



UNIVERSITÀ
DEGLI STUDI
DI PADOVA

UNIVERSITÀ DEGLI STUDI DI PADOVA — UNIVERSITÉ DE LIÈGE

DIPARTIMENTO DI INGEGNERIA INDUSTRIALE

Corso di Laurea Magistrale in Ingegneria dei Materiali

TESI DI LAUREA MAGISTRALE

**STUDIO DELLE ETEROGENEITÀ MICROSTRUTTURALI IN UN
RIVESTIMENTO COMPOSITO A MATRICE METALLICA DI
ACCIAIO INOSSIDABILE 316L E CARBURO DI TUNGSTENO,
PRODOTTO CON LASER CLADDING**

**MICROSTRUCTURAL HETEROGENEITIES IN LASER CLAD STAINLESS
STEEL + TUNGSTEN CARBIDES COMPOSITE COATINGS**

Relatrici:

Prof.ssa IRENE CALLIARI

Prof.ssa ANNE MERTENS

Controrelatrice:

Prof.ssa KATYA BRUNELLI

Laureanda: ELENA MANCINI

Anno accademico: 2016/2017

Abstract

English version

Additive manufacturing is one of the most interesting and innovative methods of production. It has the potential to revolutionize the global manufacturing and logistic landscape.

This work investigates the microstructure of a coating composed by stainless-steel metal matrix (SS316L) and tungsten carbide particulates as reinforcement. Particular attention to the reaction carbides formed between the two parts of the composite was given. The material was produced by Laser Cladding technology: an additive manufacturing technique.

A microstructural characterization revealed a particular distribution of the reinforcements along the building direction and the formation of several reaction carbides. The morphology, composition and lattice type of the carbides have been studied. The complex thermal history of laser cladding has been related to the microstructure observed. The solidification sequence has been theorized with a comparison among the data from microstructural characterization, thermal analyses and the knowledge of the process mechanism.

Microstructural investigations after thermal analyses were carried out in order to observe the microstructural changes due to different cooling rates. The compounds observed exhibit large differences, despite the cooling rates were similar.

Nano hardness tests revealed a hardness evolution between the particulates and the matrix of the composite material. Further investigations on wear properties and corrosion properties are advised.

Versione italiana:

L'Additive Manufacturing è una delle tecniche produttive più interessanti e innovative. Permette un'alta libertà di progettazione e precisione dimensionale.

Questo lavoro investiga la microstruttura di un rivestimento di materiale composito a matrice metallica. La matrice è di acciaio inossidabile AISI 316L e la fase di rinforzo è composta da particelle di carburo di tungsteno (WC). Il materiale è prodotto tramite la tecnica di produzione additiva "Laser Cladding".

Attraverso una caratterizzazione ottica è stato possibile studiare la distribuzione delle particelle e quantificare la loro superficie lungo la direzione di costruzione del deposito. Questi dati sono stati collegati alla complessa storia termica subita dal pezzo durante il processo di produzione.

Una caratterizzazione elettronica ha permesso di studiare l'interfaccia tra la matrice e la fase di rinforzo. Molti tipi di carburi sono stati osservati. La loro morfologia, composizione e tipo di reticolo sono stati studiati per identificarne la natura. Ancora una volta, la complessa storia termica è stata collegata ai carburi osservati. Una possibile sequenza di solidificazione è stata teorizzata confrontando i dati ottenuti dalla caratterizzazione microstrutturale, i dati dalle analisi termiche e la conoscenza del processo di produzione.

Dopo le analisi termiche sono state effettuate ulteriori analisi microstrutturali per osservare i cambiamenti microstrutturali dovuti a diverse velocità di raffreddamento. I composti osservati hanno esibito molte differenze, anche se le velocità di raffreddamento non erano molto diverse tra loro.

Test di nanodurezza sono stati effettuati sui composti formati tra matrice e fase di rinforzo. Ulteriori test di resistenza all'usura e resistenza a corrosione sono consigliati.

Acknowledgments

First, I would like to acknowledge Prof. Anne Mertens from AM Department for supervising my work and for patiently helping me while writing this thesis. I would also thank Prof. Jacqueline Lecomte-Beckers and Prof. Irene Calliari for giving me the opportunity to work at the ULg.

I am grateful to the Additive Manufacturing Team of the Sirris Research Centre for the production of the samples analyzed. Thanks to APTIS, Faculty of Science, ULg, for providing me the granulometry analyses on WC powders. I would also thank Thibaut L'Hoest for giving me some good basis for starting my work.

A big thanks to all the team of the MMS (Metallic Material Science) department: Jérôme T. Tchuindjang, Hakan Paydas, Rosine Pirson, Olivier Dedry, Sylvie Reginster, Henry-Michel Montrieux. In particular, I would like to acknowledge Tommaso Maurizi-Enrici for helping me with the experimental part and for showing a lot of interest in my work and Neda Hashemi for her huge moral support and advises. Thanks to S. Salieri for helping me with the sample preparation and to Jocelyn Delahaye for helping me.

A big thank to the Industrial Engineering Department of the University of Padova for helping me and advising me in the ultimate review of my thesis.

I am infinitely grateful to my family for their support and for their continuous belief in me, even when I did not believe in me anymore. Thanks to Claudio for being always there when I needed him, for his infinite moral support and help.

Thanks to all my Erasmus friends for sharing with me useful experiences.

Thanks to my friends in Italy, first of all to the Prèsidents group for sharing with me the best university years.

Table of Contents

1	Introduction	1
2	State of art	3
2.1	Additive Manufacturing	3
2.1.1	Techniques of additive Manufacturing	3
2.1.2	Parameters of Laser Cladding by powder injection	7
2.2	Coatings produced by Laser Cladding	11
2.3	Utilized materials	12
2.3.1	Stainless Steel 316L.....	12
2.3.2	Tungsten Carbide	16
2.4	Microstructure of SS316L during Laser Cladding	19
2.5	Phases formed by reaction between 316L Austenitic Stainless Steel and WC	23
3	Experimental Methods	29
3.1	Materials.....	29
3.1.1	Analysis on SS316L powder.....	29
3.1.2	Analysis on WC powder	30
3.2	Sample fabrication.....	32
3.2.1	Cladding Machine	32
3.2.2	Parameters for the realization of the samples	35
3.2.3	Samples examined in this work	37
3.3	Microstructural characterization.....	39
3.3.1	Optical microscope and Stream Analysis Software.....	39
3.3.2	Scanning Electron Microscope	40
3.4	Thermo-Calc Equilibrium Software.....	41
3.5	Thermal Analyses.....	42
3.5.1	General rules for reading DTA thermograms	43
3.6	Nanohardness Tests	44
4	Results	45
4.1	Powder Characterization	45
4.1.1	Stainless Steel 316L powder	45
4.1.2	WC powder	46
4.2	Microstructural Characterization.....	48
4.2.1	Additive Manufacturing conditions	48

4.3	Thermo-calc simulations	72
4.3.1	Pseudo-equilibrium conditions simulations	72
4.3.2	Simulations of equilibrium diagram	74
4.4	Thermal analyses results	76
4.4.1	DTA	77
4.4.2	Microstructural observations of the samples after Thermal Analyses	85
4.5	Nano-hardness tests	96
5	Discussion	97
5.1	Particles distribution.....	97
5.1.1	Distribution and particles surface quantification along y axis (building direction).....	97
5.1.2	Distribution along x axis	98
5.2	Microstructures of clad deposits: phase identification	99
5.2.1	Possible phases according to SE + EDS + EBSD	99
5.2.2	DTA heating curves	101
5.3	Solidification schemes as a function of cooling rate	104
5.3.1	Slow cooling rate	104
5.3.2	Hypothetical solidification of the laser clad deposit (high cooling rates).....	107
	Nano-hardness considerations	111
6	Conclusions and future prospects	113
7	References	115
8	Annexes	119
8.1	Annex A: Datasheet SS316L powder.....	119
8.2	Annex B: Datasheet WC powder	122
8.3	Annex C.....	123

List of Figures

Figure 2-1: Schematic illustration of an AM powder bed system [6].....	4
Figure 2-2: Schematic illustration of an AM powder feed system [7].....	5
Figure 2-3: Schematically illustration of an AM wire feed system [8].	5
Figure 2-4: The comparison of coaxial (left) and side (right) laser cladding set-up [11].....	7
Figure 2-5: Inputs, outputs and process parameters of laser cladding by powder injection [10].	8
Figure 2-6: A typical cross section of a clad bead [10].	9
Figure 2-7: Laser cladding cross sections, associated wetting angle and interfacial free energies [10]: a) high dilution, well wetting, b) ideal clad, c) no dilution, non-wetting.....	10
Figure 2-8: Schaeffler diagram displaying the microstructures of the distinct types of stainless steel [15].	15
Figure 2-9: Generalized phase diagram of the W–C system [19].....	16
Figure 2-10: Representation of the crystallographic structures of the different WC carbides. a) Hexagonal structure of the L’3-type of lower disordered β -W ₂ C carbide. The octahedral interstitials ● are randomly occupied by carbon atoms C with a probability of 1/2; b) Distribution of carbon atoms in lower carbides β -W ₂ C (1), β' -W ₂ C (2), β'' -W ₂ C (3) and ϵ -W ₂ C (4). Tungsten atoms W are not shown. The positions of nonmetal interstitial atoms ● are randomly occupied by carbon atoms with a probability of 1/2; c) The B1-type (NaCl) structure of cubic carbide γ -WC _{1-x} . d) Hexagonal structure of higher δ -WC (WC) [19].....	17
Figure 2-11: Complex thermal history related to additive manufacturing processes. a) [20]. b) [21]	19
Figure 2-12: Typical layered microstructure obtained with additive manufacturing. a) Optical macrostructure of SS316L produced using LENS [22]. b) AlSi10Mg, SLM, 10%-NaOH etched, longitudinal section, 100× [24].	20
Figure 2-13: a) Fine dendritic microstructure within layered structure [23]. b) Inverse Pole Figure (IPF) maps obtained by EBSD plotted with respect to the building direction [25].	20
Figure 2-14: a) Schematic representation of the structure of solidification of an ingot [29]. b) SEM image of a dendritic solidification morphology [30].	21
Figure 2-15: Typical morphology of M ₆ C eutectic in as cast microstructure of M2 steels [34]. a) Optical image: etching KOH+K ₃ Fe(CN) ₆ . b) SEM image.	24
Figure 2-16: Morphological types of M ₂ C eutectic [34].....	24
Figure 2-17: Morphological types of MC eutectic [34].....	25
Figure 2-18: Microstructures of a Fe-Cr-C alloys in as-cast state [36]. Dyed OM image of a Fe-Cr-C alloy [37].	25
Figure 2-19: Grain boundary sensitization [15].	26
Figure 2-20: Primary and lamellar Laves phases [39]	26
Figure 2-21: Duplex stainless-steel annealed 4 hours at 1040°C, displaying the formation of σ -phase [41].	27
Figure 3-1: Malvern Mastersizer 2000 [44].	31
Figure 3-2: Cladding Machine DUOCLAD VI LF 2000 (five axes) [1].	32
Figure 3-3: Coaxial nozzle by IREPA [1].	33
Figure 3-4: Powder Dispenser MediCoat DUO [1].	34
Figure 3-5: Turntable, displaying the scraper and the collector [1].	35

Figure 3-6: a) Schematization of the deposition of the strands [1]. b) Position of the porosity between the tracks [1].	37
Figure 3-7: Samples realized in SS316L [1]. a) Top view. b) Lateral view.	38
Figure 3-8: Samples of SS316L+WC analyzed [1].	38
Figure 3-9: a) Samples laser clad SS316L+WC. b) Samples after DTA.	39
Figure 3-10: Example of the image post processing to evaluate the particles position and surface in the composite material. a) Overview of one of the samples. b) Photo after post processing.	40
Figure 3-11: Realization of the DTA samples. a) Extraction of the carrot from the sample. b) Cutting zones.	42
Figure 3-12: DTA thermograms showing [33]: a) temperature of onset and end of transformation for a simple peak b) deconvolution to distinguish separately two superimposed peaks.	43
Figure 3-13: TI 950 Triboindenter by Hysitron [48].	44
Figure 4-1: SEM images of SS316L particles. a) Particles' surface. b) Particularity of the surface. c) Cross-section of the particle. [1]	45
Figure 4-2: SEM images of WC particles. a) Particles' surface. b) Particularity of the surface.	46
Figure 4-3: Output of the granulometry test on the WC particles.	47
Figure 4-4: Overview and particles map for sample W27.	49
Figure 4-5: Overview and particles map for sample W43.	49
Figure 4-6: Overview and particles map for sample W53.	50
Figure 4-7: Overview and particles map for sample W62.	50
Figure 4-8: Number of particles every 100µm layer, y direction. Sample W27.	51
Figure 4-9: Number of particles every 100µm layer, y direction. Sample W43.	52
Figure 4-10: Number of particles every 100µm layer, y direction. Sample W53.	52
Figure 4-11: Number of particles every 100µm layer, y direction. Sample W62.	53
Figure 4-12: Number of particles every 100 µm layer, x direction. Sample W27.	54
Figure 4-13: Number of particles every 100 µm layer, x direction. Sample W43.	54
Figure 4-14: Number of particles every 100 µm layer, x direction. Sample W53.	55
Figure 4-15: Number of particles every 100 µm layer, x direction. Sample W62.	55
Figure 4-16: Particles' surface every 100 µm layer along y axis. Sample W27.	57
Figure 4-17: Particles' surface every 100 µm layer along y axis. Sample W43.	57
Figure 4-18: Particles' surface every 100 µm layer along y axis. Sample W53.	58
Figure 4-19: Particles' surface every 100 µm layer along y axis. Sample W62.	58
Figure 4-20: Investigations on dendrites growth direction with optical microscope. a) 100x magnification.	59
Figure 4-21: Investigations on dendrites growth direction with SEM. a) 400x magnification.	59
Figure 4-22: Optical image of the carbides formed around the particles. 500x of magnification.	60
Figure 4-23: SEM images at low magnifications of the carbides around the particles. a) Overview at 200x of magnification. b) Detail at 2000x of the two near particles on the top. c) Detail at 2000x of the smaller particle in the middle.	61
Figure 4-24: SEM images at high magnifications of the carbides around the particles. a) and b) pictures are higher magnifications of the Figure 4-23b. c) and d) pictures are higher magnification of Figure 4-23c. a) and c) show a magnification of 8000x, b) and d) show a magnification of 16000x.	62
Figure 4-25: Different zones considered around the particle to study the formation of the different carbides.	62

Figure 4-26: Zone A: subdivision to study the compositions.	63
Figure 4-27: Zone B: subdivision to study the compositions.	64
Figure 4-28: Zone C: subdivision to study the compositions.	65
Figure 4-29: Zone D: subdivision to study the compositions. a) compounds further away from the particle. b) compounds near the particle.	66
Figure 4-30: First EBSD. a) BSE picture of the analysis zone. b) Pattern quality of the analysis. ...	68
Figure 4-31: First complete EBSD phase map.....	69
Figure 4-32: a) Inverse Pole Figure (IPF) map in x direction displaying the different orientations of the crystals. b) Inverse Pole Figure color key.....	70
Figure 4-33: Second EBSD. a) BSE picture of the analyzed zone. b) Pattern quality of the analysis.	70
Figure 4-34: Second complete EBSD phase map.	71
Figure 4-35: a) Inverse Pole Figure (IPF) map in x direction displaying the different orientations of the crystals. b) Inverse Pole Figure color key.....	71
Figure 4-36: Scheil simulation performed with Thermo-calc software. SS316L.	73
Figure 4-37: Scheil simulation performed with Thermo-calc software. SS316L + 0.03 wt% C and 0.5 wt% W.....	73
Figure 4-38: Scheil simulation performed with Thermo-calc software. SS316L + 0,05 wt% W.....	74
Figure 4-39: Scheil simulation performed with Thermo-calc software. SS316L + 5 wt% W.....	74
Figure 4-40: Equilibrium diagrams obtained with Thermo-calc. a) Diagram obtained with fixed a temperature of 1000 °C. b) Diagram obtained with a fixed temperature of 1250 °C.	75
Figure 4-41: Heating thermogram for SS316L produced by SLM process.....	77
Figure 4-42: Cooling thermogram for SS316L produced by SLM process.....	78
Figure 4-43: Heating thermogram for W27 (test DT1) produced by laser cladding process.	79
Figure 4-44: Cooling thermogram for W27 (test DT1) produced by laser cladding process.	80
Figure 4-45: Heating thermogram for W27 (test DT3) produced by laser cladding process.	81
Figure 4-46: Cooling thermogram for W27 (test DT3) produced by laser cladding process.	82
Figure 4-47: Heating thermogram for W27 (test DS4) produced by laser cladding process.....	83
Figure 4-48: Cooling thermogram for W27 (test DS4) produced by laser cladding process.	84
Figure 4-49: Overview of sample DS4.	86
Figure 4-50: Optical micrograph of the zone near the particles, sample DS4. a) Magnification 100x. b) Magnification 200x. c) Magnification 500x. d) different zones observed and their different thickness. Magnification 500x.	86
Figure 4-51: SEM-BSE images of the dissolution of the particles, sample DS4. a) 200x. b) 800x. c) 1600x. d) 3200x.	87
Figure 4-52: Secondary carbides formed by the dissolution of particles.....	88
Figure 4-53: Overview of sample DT1.	89
Figure 4-54: Optical images, sample DT1. a) 100x. b) 200x. c) 500x. d) 500x.	90
Figure 4-55: SEM-BSE images, sample DT1. a) 200x. b) 800x. c) 1600x. d) 3200x.....	91
Figure 4-56: Finer lamellae revealed with higher magnifications.	91
Figure 4-57: Overview of sample DT3.	93
Figure 4-58: Optical images, sample DT3. a) 100x. b) 200x. c) 500x. d) 500x.	93
Figure 4-59: SEM-BSE images, sample DT3. a) 200x. b) 800x. c) 1600x. d) 3200x.....	94
Figure 4-60: Darker areas in the vicinity of lighter carbides. Sample DT3.....	94

Figure 4-61: Scansions of the surface of the sample after nano-indentation. a) Analyzed indents. (1) Indent in the carbide around the particle (M_2C primary). (2) Indent in an eutectic carbide (M_6C or M_7C_3).	96
Figure 5-1: Complete DTA heating tests (DT1 and DT3) with the possible peaks explanation.	103
Figure 5-2: DTA cooling test (DT3) with the possible peaks explanation.	105
Figure 5-3: DTA cooling test (DT1) with the possible peaks explanation.	107
Figure 5-4: a) Optical image representing the open M_2C carbide surrounded by the finer carbide. 1000x. b) SEM image showing the presence of cavities. 600x.	107
Figure 5-5: Possible WC particles dissolution processes. a) First way of dissolution. Blue arrow indicates the diffusion direction of W and C, orange arrow indicates the reduction in size of the WC particle. b) Second way of dissolution. Yellow arrows indicate the liquid penetration, orange arrow indicates the reduction in size of the WC particle.	108
Figure 5-6: Schematization of the laser clad process with indication of the different parts.	110
Figure 5-7: Zoom of Figure 5-6 near the solidification front with a schematization of the microstructure observed in Figure 4-23.	110
Figure 5-8: Displacement of one particle in the melt pool.	111

List of Tables

Table 2-1: Main AM equipment sources and specification [5].	4
Table 2-2: Confrontation between coating techniques [10].	11
Table 2-3: Nominal composition of SS316L [17].	13
Table 2-4: Main properties of SS316L [17].	14
Table 2-5: Crystal structure of phases in the W–C system at $T > 1300$ K. Designations as in Figure 2-9 [19].	18
Table 2-6: Main characteristics of the tungsten carbide[17].	18
Table 3-1: Composition provided by Carpenter Powder Products for SS316L (Annex A).	30
Table 3-2: Composition from Höganäs AB (Annex B).	30
Table 3-3: Characteristics of the laser used and parameters utilized to build the sample [1].	33
Table 3-4: Parameters for the nozzle.	35
Table 3-5: Flow rates of the powders.	36
Table 3-6: Control Laser Power/ feed speed.	36
Table 3-7: Production parameters [1] and name of the different samples.	38
Table 3-8: Thermal tests description.	42
Table 4-1: Composition of SS316L calculated with EDS in weight percent.	46
Table 4-2: Composition of WC calculated with EDS in weight percent.	46
Table 4-3: Fraction of particles surface for each sample.	56
Table 4-4: Compositions in wt% and relative deviation standard values. Zone A.	63
Table 4-5: Compositions in at% and relative deviation standard values. Zone A.	64
Table 4-6: Compositions in wt% and relative deviation standard values. Zone B.	64
Table 4-7: Compositions in at% and relative deviation standard values. Zone B.	64
Table 4-8: Compositions in wt% and relative deviation standard values. Zone C.	65
Table 4-9: Compositions in at% and relative deviation standard values. Zone C.	66
Table 4-10: Compositions in wt% and relative deviation standard values. Zone D.	67
Table 4-11: Compositions in at% and relative deviation standard values. Zone D.	67
Table 4-12: Correlation of colors in Figure 4-31 with their lattice type. C is for cubical, T is for trigonal.	69
Table 4-13: Name given to the phases in the Thermo-calc software and actual names.	75
Table 4-14: Attribution of the different transformations to each peak. SLM SS316L heating.	77
Table 4-15: Attribution of the different transformations to each peak. SLM SS316L cooling.	78
Table 4-16: Attribution of the different transformations to each peak. DT1 test on laser clad W27, heating.	79
Table 4-17: Attribution of the different transformations to each peak. DT1 test on laser clad W27, cooling.	80
Table 4-18: Attribution of the different transformations to each peak. DT3 test on laser clad W27, heating.	82
Table 4-19: Attribution of the different transformations to each peak. DT3 test on laser clad W27, cooling.	83
Table 4-20: Attribution of the different transformations to each peak. DS4 test on laser clad W27, heating.	83
Table 4-21: Compositions in wt% and relative deviation standard values. Sample DS4.	88
Table 4-22: Compositions in at% and relative deviation standard values. Sample DS4.	88

Table 4-23: Compositions in wt% and relative deviation standard values. Sample DT1.....	92
Table 4-24: Compositions in at% and relative deviation standard values. Sample DT1.....	92
Table 4-25: Compositions in wt% and relative deviation standard values. Sample DT3.....	95
Table 4-26: Compositions in at% and relative deviation standard values. Sample DT3.....	95
Table 4-27: Values measured by the nano-indenter.....	96
Table 5-1: Composition in at% of each zone in the sample with indications of the correspondent carbide type.	101
Table 5-2: Output values of the nano-indenter, with the addition of the hardness values converted in HV.....	112

1 Introduction

Innovation and research are inherent to many industries as energetical, transports, petrochemical, etc. One of the most interesting innovative methods of production is Additive Manufacturing.

It has the potential to revolutionize the global manufacturing and logistic landscape. It enables distributed manufacturing and the production of parts-on-demand while offering the potential to reduce cost, energy consumption and carbon footprint.

The study of the realization of metal/ceramics deposits by Additive Manufacturing is complex. It involves various fields of study in metallurgy: powder metallurgy (atomization-powder production), welding (during printing powder are welded together), solidification processes (out of equilibrium, very fast solidification processes with very fine microstructures).

This thesis presents the study on the microstructure of the metal matrix composite (MMC) composed by 316L, as matrix, and WC particles. This implies the inclusion of other two fields of study. Firstly, the inclusion of coatings of metallic surfaces, because the aim of the WC particles in the matrix is to improve the hardness and the wear resistance. Secondly, the inclusion of metal matrix composite science (adhesion between the two phases).

This work is part of a vaster research project by the University of Liege: Métallurgie et Science des Matériaux (MMS). It represents the continuation of a previous work by Thibaut L'Hoest [1] with a published paper by Anne Mertens [2].

In the following chapters, the topics here shortly presented will be described. Firstly, chapter 2 will present the state of art on additive manufacturing focusing on laser cladding process and the characteristics of the materials. Secondly, chapter 3 will present the experimental methods utilized in this work. Thirdly, chapter 4 will present the results of the tests performed. Fourthly, chapter 5 will discuss the results presented in chapter 4. Finally, chapter 6 will show the conclusions and the prospects, chapter 7 contains the references and chapter 8 the annexes.

2 State of art

This chapter presents the state of art of the topics needed for the discussion of the results. The main topics treated are: (1) Additive Manufacturing (AM) technology, focusing on laser cladding process; (2) the materials utilized in this work: 316L stainless steel and WC particles; (3) microstructure presented by 316L stainless steel submitted to laser cladding process; and (4) an explanation of the compounds and constituent found.

2.1 Additive Manufacturing

Additive Manufacturing (AM), also known as 3D printing, is a “process of joining materials to make objects from 3D model data, usually layer upon layer, as opposed to subtractive manufacturing methodologies”. This definition, from ASTM 52900-15 [3], is applicable to all kind of materials including metals, ceramics, polymers, biological tissues and composites.

The field of additive manufacturing application is huge. Early use of AM in the form of Rapid Prototyping (RP) focused on preproduction visualization models. More recently, AM has been used to fabricate end-use products in aircraft, dental restorations, medical implants, automobiles, and even fashion products. The idea of using a digital file to create a three-dimensional (3-D) object is now a reality, making the transition from rapid prototyping to part production. AM has attracted much attention over the past ten years due to its immanent advantages, such as unrivalled design freedom and short lead times. With the advancement of technology, part density and quality were improved for a wide number of materials [4].

Thus, a deep knowledge is required of (1) the process itself, (2) the microstructure resulting from the process parameters and consequently of (3) the properties of the manufactured parts.

2.1.1 Techniques of additive Manufacturing

AM system may be classified in terms of the material feedstock, energy source, build volume, etc. Table 2-1 is a selected list of equipment manufacturers and their equipment. In this table, manufacturing systems are divided into three broad categories (while there are many more): powder bed systems, powder feed systems and wire feed systems [5].

Table 2-1: Main AM equipment sources and specification [5].

System	Process	Build volume (mm)	Energy source
Powder bed			
ARCAM (A2)(a)	EBM	200 × 200 × 350	7 kW electron beam
EOS (M280)(b)	DMLS	250 × 250 × 325	200-400 W Yb-fiber laser
Concept laser cusing (M3)(b)	SLM	300 × 350 × 300	200 W fiber laser
MTT (SLM 250)(b)	SLM	250 × 250 × 300	100-400 W Yb-fiber laser
Phenix system group (PXL)(c)	SLM	250 × 250 × 300	500 W fiber laser
Renishaw (AM 250)(d)	SLM	245 × 245 × 360	200 or 400 W laser
Realizer (SLM 250)(b)	SLM	250 × 250 × 220	100, 200, or 400 W laser
Matsuura (Lumex Advanced 25)(e)	SLM	250 × 250 diameter	400 W Yb fiber laser; hybrid additive/subtractive system
Powder feed			
Optomec (LENS 850-R)(f)	LENS	900 × 1500 × 900	1 or 2 kW IPG fiber laser
POM DMD (66R)(f)	DMD	3,200° × 3°, 670° × 360°	1-5 kW fiber diode or disk laser
Accufusion laser consolidation(g)	LC	1,000 × 1,000 × 1,000	Nd:YAG laser
Irepa laser (LF 6000)(c)	LD		Laser cladding
Trumpf(b)	LD	600 × 1,000 long	
Huffman (HC-205)(f)	LD		CO ₂ laser cladding
Wire feed			
Sciaky (NG1) EBFFF(f)	EBDM	762 × 483 × 508	> 40 kW @ 60 kV welder
MER plasma transferred arc selected FFF(f)	PTAS FFF	610 × 610 × 5,182	Plasma transferred arc using two 350A DC power supplies
Honeywell ion fusion formation(f)	IFF		Plasma arc-based welding

Country of Manufacturer: (a) Sweden, (b) Germany, (c) France, (d) United Kingdom, (e) Japan, (f) United States, and (g) Canada

- Regarding the powder bed system, a powder bed is created by raking powder across the work area [Figure 2-1]. The energy source (electron beam or laser beam) is programmed to deliver energy to the surface of the bed melting or sintering the powder into the desired shape. Then, additional powder is raked across the work area, and the process is repeated to create the solid three-dimensional component. The advantages include its ability to produce high resolution features, internal passages, and maintain dimensional control.

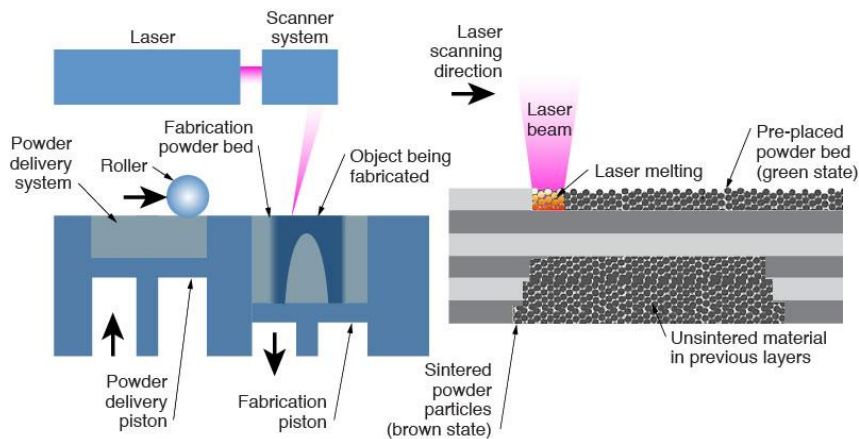


Figure 2-1: Schematic illustration of an AM powder bed system [6]

- A schematic illustration of an AM powder feed system is shown in Figure 2-2. Powder are conveyed through a nozzle on the build surface. A laser is used to melt a monolayer or more

into the desired shape. The advantages of this type of system include its larger build volume and its ability to refurbish worn or damaged components.

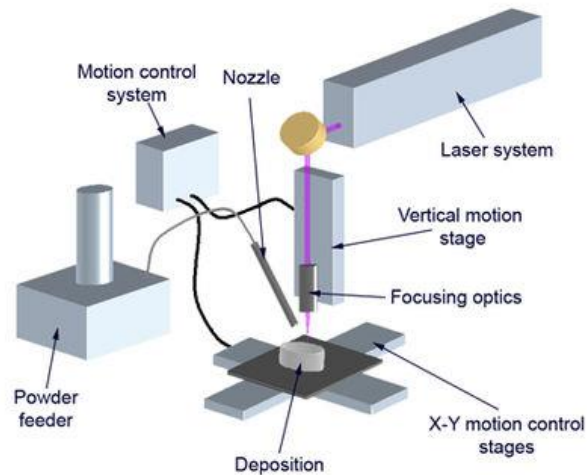


Figure 2-2: Schematic illustration of an AM powder feed system [7].

- With regard to the wire feed systems, the feed stock is a wire and the energy source can include electron beam, laser and plasma arc. Firstly, a single bead of material is deposited and upon subsequent passes is built upon to develop a three-dimensional structure. The wire feed system is well suited for high deposition rate and for large build volumes. However, the final product usually requires extensive machining [Figure 2-3].

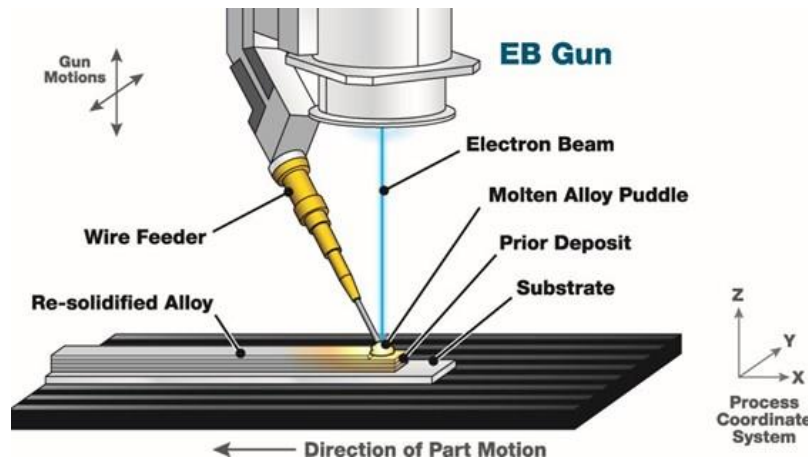


Figure 2-3: Schematically illustration of an AM wire feed system [8].

The most popular processes for AM of metals are Laser Beam Melting (LBM), Electron Beam Melting (EBM), and Laser Metal Deposition (LMD). LBM process is also known as Selective Laser Melting (SLM), Direct Metal Laser Sintering (DMLS), Laser CUSING, Laser Metal Fusion (LMF) or industrial 3D printing. LMD process is also called Direct Metal Deposition (DMD), Laser

Engineered Net Shaping (LENS), Laser Cladding (LC) or laser deposition welding. Most of these names are trademarks of different machine manufacturers.

2.1.1.1 Laser Cladding

Laser cladding is a process that combines various scientific fields: laser technology, computer-aided design and manufacturing (CAD/CAM), robotics, sensors and control and powder metallurgy. This process utilizes a laser heat source to deposit a thin layer of metal on a substrate. The deposited material can be transferred to the substrate by several methods: powder injection (powder feed), pre-placed powder on the substrate, or by wire feed. Among these methods, laser cladding by powder injection has been demonstrated to be most effective. In the case of powder injection, a carrier gas is used to form a cladding powder stream, which is blown under the laser beam while it scans the surface of the substrate. This way, a melt pool with a depth corresponding to the thickness of a single clad is generated. To cover large surfaces, overlapping tracks are made: the laser beam melts the powder particles and a thin layer of the substrate. Argon gas is commonly used as a shielding and carrier gas [9].

A wide variety of materials can be processed by laser cladding with powder feed technology.

The integration of the laser cladding technology with a three-dimensional CAD solid model, provides the ability to fabricate complex components without intermediate steps. The development of the laser cladding technology depends on enhancement of the technologies involved. Understanding the interconnections between the involved technologies and the process quality is a major step for the development of laser cladding. However, numerous interactions between the technologies involved in laser cladding not only increase the complexity of the process but also increase the number of process parameters [10].

The laser cladding by powder injection is the one of interest. Two ways of feeding powder are available: from a side or coaxially to the laser beam [Figure 2-4]. When the powder stream is delivered coaxially to the laser beam, all the directions of the substrate movement (x-y) perpendicular to the laser beam are equivalent, being independent of the cladding direction. Therefore, it is possible to build equivalent tracks independently on the moving direction of the specimen.

A complete description and modelling of the laser cladding technique with injection powder into a laser melt pool is very complex, because of the numerous interactions: laser beam-powder, laser beam-substrate, powder stream-melt pool, powder stream-solid substrate. Furthermore, physical phenomena like mass and heat transfer, fluid flow, and phase transformation are involved [11].

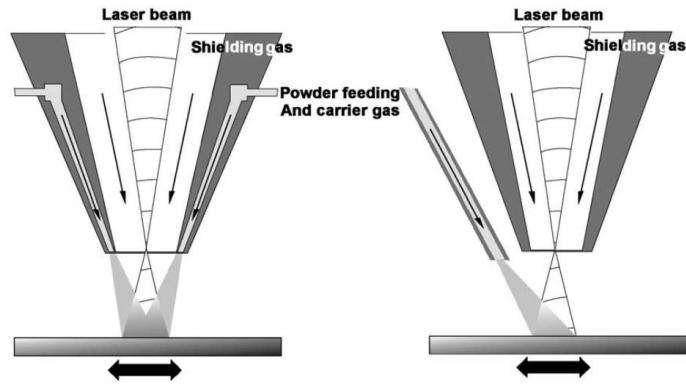


Figure 2-4: The comparison of coaxial (left) and side (right) laser cladding set-up [11].

The thickness of the track deposited is typically 50 μm up to 2 mm in one step.

Laser cladding requires high average laser power. Shared power densities are in the range: 10^2 - 10^4 W/cm^2 , with an interaction time around 10^{-3} - 0.5 s [12].

The lasers that have sufficient power for laser cladding are CO_2 lasers, Nd:YAG lasers and High Power Diode Lasers (HPDLs). The CO_2 laser is the most commonly used laser for cladding, particularly for cladding of small areas. The pulsed Nd:YAG is the best choice because of the good control of the energy input. CO_2 lasers and Nd:YAG lasers are already implemented in industry for repairing and regenerating structures and engine part. HPDLs are less common but their efficiency is higher. One of the reason is that the shape of the intensity distribution is non-Gaussian [9].

2.1.2 Parameters of Laser Cladding by powder injection

A large variety of operating parameters and physical phenomena determine the quality of laser cladding. Figure 2-5 presents an overview of these parameters gathered as inputs, processes, and outputs. Usually, the inputs or operating parameters are the laser, motion device, powder feeder set points, material and ambient properties. The outputs of the process, which represent the clad quality, are the geometry, microstructure, cracks, porosity, surface roughness, residual stresses and dilution [13,14]. In the following, some of the main parameters of this process are explained.

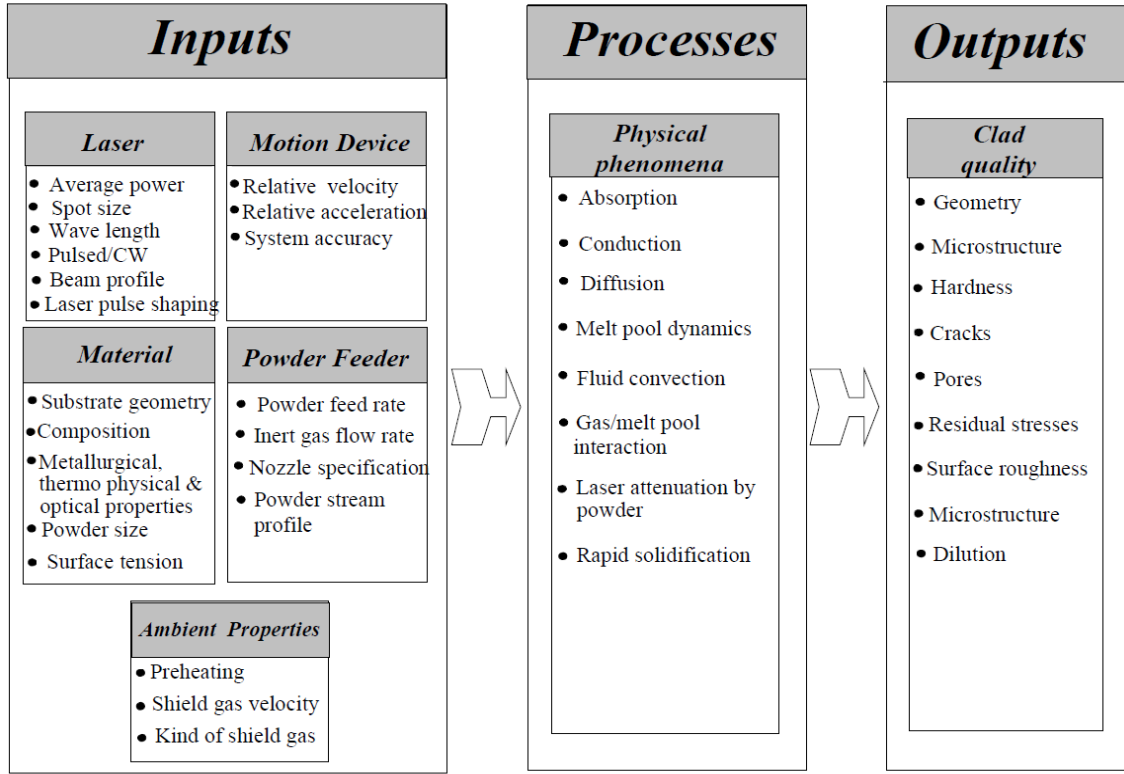


Figure 2-5: Inputs, outputs and process parameters of laser cladding by powder injection [10].

2.1.2.1 Dilution

One of the characteristics of the clad layer is the dilution. This is defined as the amount of intermixing of the clad and substrate materials. Dilution has two definitions: geometrical and metallurgical [13]. According to the specified parameters in Figure 2-6, the geometrical definition of dilution is:

$$Dilution = \frac{b}{h + b} \quad (1)$$

where b is the thickness of substrate that was melted during the cladding process [mm], and h is the height of the clad bead [mm]. Other geometrical characteristics are defined in this figure: w is the clad width, θ is the angle of wetting (see also section 2.1.2.2).

The metallurgical definition of dilution is:

$$Dilution = \frac{\rho_c(X_{c+s} - X_c)}{\rho_s(X_s - X_{c+s}) + \rho_c(X_{c+s} - X_c)} \quad (2)$$

Where dilution is defined as the percentage of the total volume of the surface layer contributed by melting of the substrate. With ρ_c the density of melted powder alloy [kg/m³], ρ_s density of substrate material [kg/m³], X_{c+s} weight percent of the element X in the total surface of the clad region [%], X_c

the weight percent of element X in the powder alloy [%], and X_s the weight percent of element X in the substrate [%]. Dilution increases with increasing laser power, but decreases with increasing scanning speed.

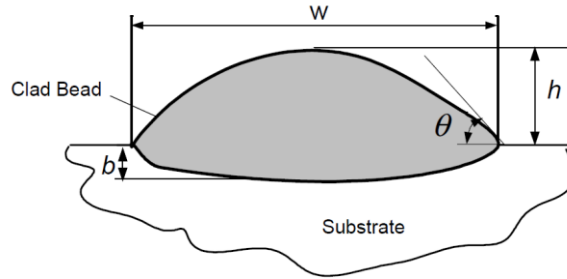


Figure 2-6: A typical cross section of a clad bead [10].

2.1.2.2 Wettability

In laser cladding wetting angle and interfacial free energies are important parameters that indicate the quality of the clad. Three types of clad cross section may be produced by laser cladding as shown in Figure 2-7. The wetting angle θ , and the interfacial free energies γ_{ij} [J/m^2], affect the amount of dilution. Three interfacial energies can be considered for laser cladding: solid-liquid interfacial free energy γ_{SL} , solid-vapor interfacial energy γ_{SV} , and liquid-vapor interfacial energy γ_{LV} [10].

A balance between the mentioned energies governs the shape of the clad bead. This balance is expressed by:

$$\gamma_{SV} - \gamma_{SL} = \gamma_{LV} \cos \theta \quad (3)$$

The liquid will wet the substrate as $\cos \theta \rightarrow 1$, or equivalently, if $\gamma_{SV} - \gamma_{SL} > \gamma_{LV}$ [Figure 2-7b].

A high positive spreading factor: $S = \gamma_{SV} - \gamma_{SL} - \gamma_{LV}$ causes the spreading of the track, while a low spreading factor results in a non-wetting system as shown in Figure 2-7c. Furthermore, when the laser energy is high, dilution increases and wetting angle decreases as shown in Figure 2-7a.

Due to the elevated temperatures necessary to melt the metals, oxidation can easily occur in laser cladding. The oxidation causes a low quality clad, as shown in Figure 2-7c. This is owed to the low wetting of an oxide substrate by a liquid metal and the lower surface energies of metal oxides.

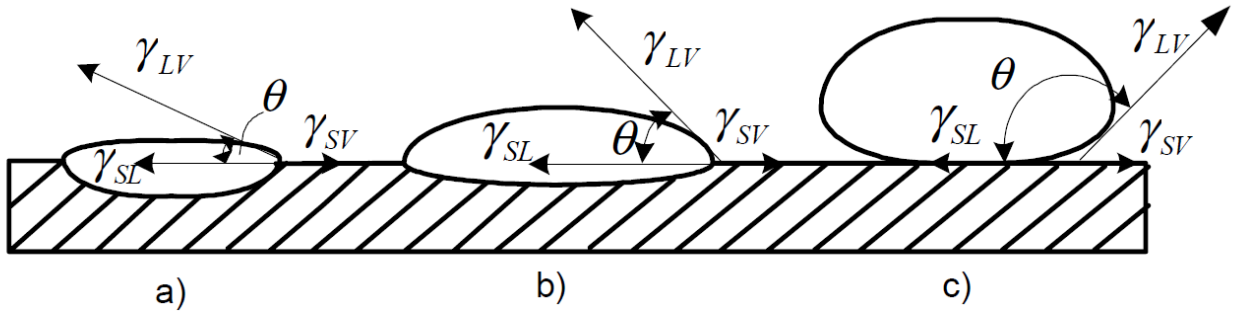


Figure 2-7: Laser cladding cross sections, associated wetting angle and interfacial free energies [10]: a) high dilution, well wetting, b) ideal clad, c) no dilution, non-wetting.

2.2 Coatings produced by Laser Cladding

The application of laser cladding should compete with several coating techniques such as thermal spray, welding, chemical vapor deposition (CVD), and physical vapor deposition (PVD).

The thermal spray can be categorized into three methods, which are combustion torch (e.g., flame-spray, high-velocity oxy fuel, and detonation gun), electric (wire) arc, and plasma arc. In addition, PVD can be categorized into ion plating and ion implantation. CVD is also categorized into: sputtering, ion plating, plasma-enhanced CVD, low-pressure CVD, laser-enhanced CVD, active reactive evaporation, ion beam and laser evaporation [10].

Table 2-2 compares several major features of these coating techniques to provide the advantages and disadvantages of these processes for metallic and non-metallic coating applications. Laser cladding creates a very strong bond with low dilution, hence a very small heat-affected zone (HAZ) is produced in the substrate. Nevertheless, the investment cost and maintenance cost of the laser cladding machine are high. Upcoming developments of the laser cladding technology are focused in utilizing high-power diode and fiber lasers, which offer higher efficiency and lower maintenance cost. Therefore, laser cladding technology will play an important role in the metallic coating market in the near future.

Table 2-2: Confrontation between coating techniques [10].

<i>Feature</i>	<i>Laser Cladding</i>	<i>Welding</i>	<i>Thermal spray</i>	<i>CVD</i>	<i>PVD</i>
Bonding strength	High	High	Moderate	Low	Low
Dilution	High	High	Nil	Nil	Nil
Coating materials	Metals, ceramics	Metals	Metals, ceramics	Metals, ceramics	Metals, ceramics
Coating thickness	50 μm to 2 mm	1 to several mm	50 μm to several mm	0.05 μm to 20 μm	0.05 μm to 10 μm
Repeatability	Moderate to high	Moderate	Moderate	High	High
Heat-affected zone (HAZ)	Low	High	High	Very low	Very low
Controllability	Moderate to high	Low	Moderate	Moderate to high	Moderate to high
Cost	High	Moderate	Moderate	High	High

2.3 Utilized materials

Materials utilized to build the composite are: Stainless Steel AISI 316L as matrix and Tungsten Carbide as reinforcement phase.

2.3.1 Stainless Steel 316L

Stainless Steels, also known as inox (from French), are iron based alloys with a minimum of 10.5 wt% of chromium content. They are notable for their corrosion resistance given by a thin and compact layer of inert chromium oxide, which is formed by contact with oxidizing environment. The layer prevents further corrosion by blocking oxygen diffusion to the steel surface and stops corrosion from spreading into the bulk of the metal. This phenomenon is called passivation and it occurs only if the quantity of chromium is high enough and with presence of oxygen [15].

There are distinct types of stainless steels classified by their crystalline structure [16]:

- Austenitic stainless steel (200 and 300 series). Their crystalline structure is face-centered cubic. The maximum amount of carbon is 0,15 wt%, the minimum amount of chromium is 16 wt%. They must contain a sufficient amount of nickel to retain an austenitic structure at all temperatures: from cryogenic region to the melting point. The most widely used are 304 (also known as 18/8 for its composition of 18 wt% chromium and 8 wt% of nickel), 316 grades (also known as 18/10 for its typical composition of 18 wt% chromium and 10 wt% nickel). The austenitic stainless steels offer better corrosion resistance than all the other classes.
- Ferritic stainless steels (some of 400 series) have better engineering properties than austenitic grades, but have reduced corrosion resistance, because of the lower chromium and nickel content. Ferritic stainless steels have a body-centered cubic crystal structure. Their amount of chromium is between 10,5 and 27 wt%. Nickel amount is very little. Most composition contains molybdenum, some types can contain lead, aluminum or titanium. These alloys can be degraded by the presence of sigma phase, rich with chromium, an intermetallic phase which can precipitate upon welding.
- Martensitic stainless steels (some of 400 series) are less corrosion resistant than the other two classes, however, their toughness, strength and machinability are higher. They can even undergo hardening by heat treatment. Martensitic stainless steel contains chromium (12–14 wt%), molybdenum (0.2–1 wt%), nickel (less than 2 wt%), and carbon (about 0.1–1 wt%). It is, then, very hard but brittle.

- Duplex stainless steels have mixed microstructure of austenite and ferrite. Duplex stainless steels have roughly twice the strength compared to austenitic stainless steels and also improved resistance to localized corrosion, particularly pitting and stress corrosion cracking. They are characterized by high chromium (19–32 wt%) and molybdenum (up to 5 wt%) and lower nickel contents than austenitic stainless steels.
- The precipitation hardening (PH) stainless steels are a family of corrosion resistant alloys that can be heat treated to provide tensile strengths of 850 MPa to 1700 MPa and yield strengths of 520 MPa to over 1500 MPa. The family of precipitation hardening stainless steels can be divided into three main types: low carbon martensitic, semi-austenitic and austenitic. The most common is the 17/4-PH. It is a martensitic type. It transforms into martensite at low temperatures; typically, around 250°C. Furthermore, it is strengthened by ageing at between 480 and 620°C.

SS316L is an austenitic stainless steel. L stands for Low Carbon, that leads to an enhanced corrosion resistance in welded structures. This reduction in carbon content prevents the precipitation of chromium carbides at grain boundaries. These carbides liberate the zones in the vicinity from chromium, carrying the amount of chromium necessary for the passivation below the minimum needed (sensibilization). The 316L alloy has good weldability, which is an essential property based on the laser cladding procedure. Moreover, it is a non-magnetic alloy.

Table 2-3 reports the nominal composition of the SS316L.

Table 2-3: Nominal composition of SS316L [17].

AISI	EN	%C	%Cr	%Ni	%Mo	%Mn	%Si	%Fe
AISI 316L	X2CrNiMo18-10	≤ 0.03	16.5-18.5	10-13	2-2.5	<1	<1	Bal.

In Table 2-4 are reported some characteristics of the SS316L in fully annealed conditions [17].

Table 2-4: Main properties of SS316L [17].

Density	7870 – 8070 kg/m ³
Young's modulus	190 – 205 GPa
Yield strength (elastic limit)	170 – 310 MPa
Tensile strength	480 – 620 MPa
Elongation	30 – 50 % strain
Flexural strength (modulus of rupture)	170 – 310 MPa
Fracture toughness	53 – 72 MPa*m ^{1/2}
Hardness Vickers	170 – 220 HV
Fatigue strength at 10 ⁷	256 – 307 MPa
Melting Point	1380 – 1400 °C
Maximum service temperature	750 – 925 °C
Thermal conductivity	13 – 17 W/m*°C
Specific heat capacity	490 – 530 J/kg*°C
Thermal expansion coefficient	15 – 18 µstrain/°C
Latent heat of fusion	260 – 285 kJ/kg
Price	4,19 – 4,83 €/kg

The principle behind the functioning of Laser Cladding is very close to welding. In addition, ferrite content is important for avoiding hot cracking during welding of austenitic stainless steels. In order to understand the presence of ferrite in the steel when cooling from high temperatures and prevent hot cracking, we should refer to the Schaeffler diagram. This diagram gives a method to predict the phase balance in austenitic stainless-steel welds. For this purpose, a “nickel equivalent” is calculated for the austenite stabilizing elements and a “chromium equivalent” for the ferrite stabilizing elements. These are used as the axes for the diagrams, which show the compositional equivalent areas where the phases austenite, ferrite, martensite (and mixtures of these) should be present.

The nickel and chromium equivalents are calculated with the following formulae. The designed values correspond to the nominal composition of SS316L. As observed in Schaeffler diagram, ferrite in this type of steel can show at maximum of 15 wt%.

$$Ni(eq) = Ni(wt\%) + Co(wt\%) + 0,5 * Mn(wt\%) + 0,3 * Cu(wt\%) + 25 * N(wt\%) + 30 * C(wt\%) = 11.9 - 15.9$$

$$Cr(eq) = Cr(wt\%) + 2 * Si(wt\%) + 1,5 * Mo(wt\%) + 5 * V(wt\%) + 5,5 * Al(wt\%) + 1,75 * Nb(wt\%) + 1,5 * Ti(wt\%) + 0,75 * W(wt\%) = 21 - 24.5$$

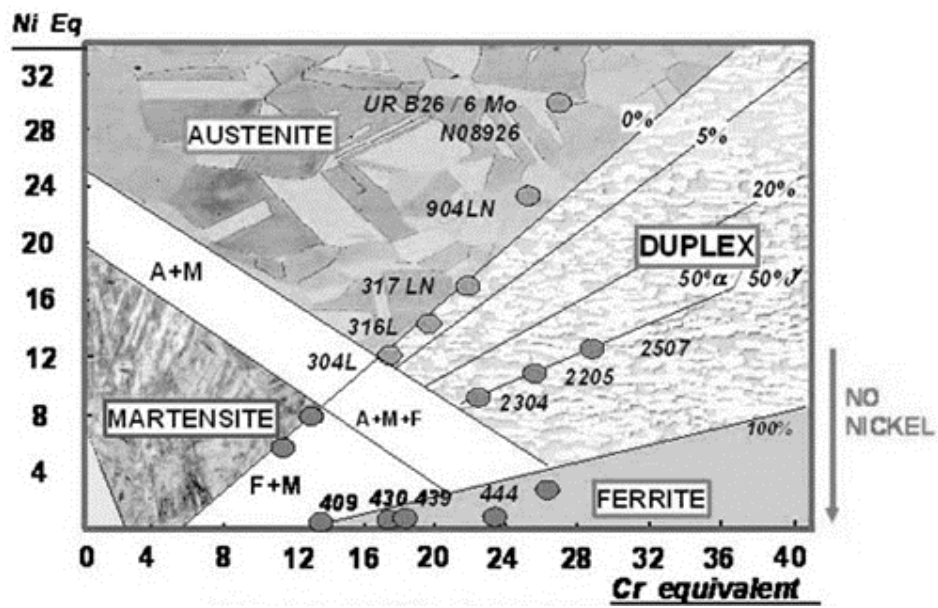


Figure 2-8: Schaeffler diagram displaying the microstructures of the distinct types of stainless steel [15].

2.3.2 Tungsten Carbide

Tungsten carbide is composed by Tungsten and Carbon. A natural form of tungsten carbide is Qusongite. Qusongite is an extremely rare mineral with the simple formula WC and presents some impurities of chromium, nickel and titanium [18]. It crystallizes in hexagonal system. Table 2-5 reports the lattice constants and the space group.

The W–C system includes two phases, namely, W_2C and WC, each having several structural modifications, which are stable in certain temperature and concentration ranges in accordance with Figure 2-9 [19].

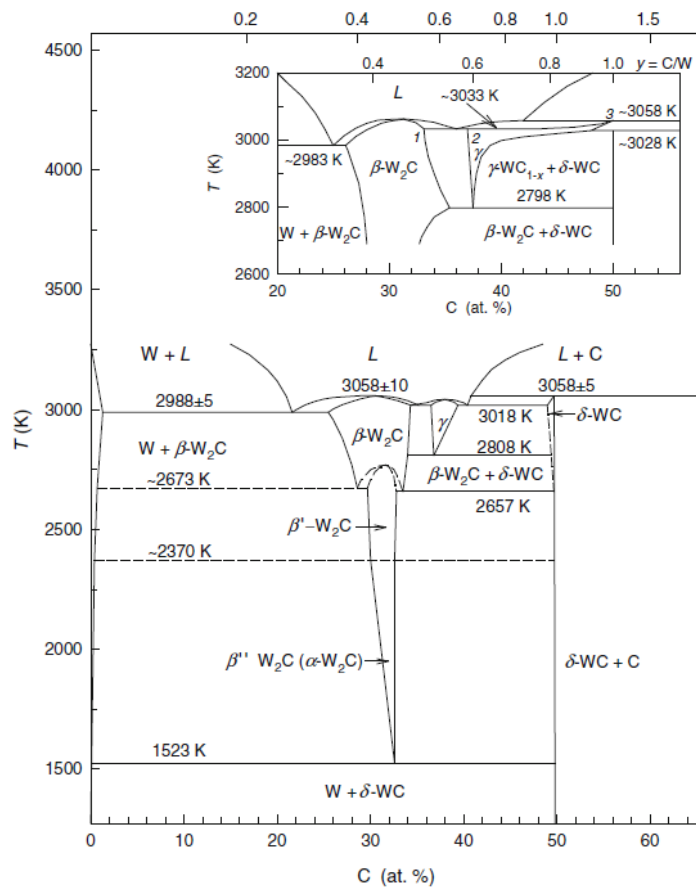


Figure 2-9: Generalized phase diagram of the W–C system [19].

There are multiple compounds that can form in the system W-C.

Four modifications are described for lower (with lower C content) tungsten carbide W_2C . Three of them are low-temperature β'' - W_2C [Figure 2-10b (3)], intermediate β' - W_2C [Figure 2-10b (2)] and high-temperature β - W_2C [Figure 2-10b (1)]. In all W_2C modifications, tungsten atoms form a hcp metallic sublattice, in which one-half of octahedral interstitials are occupied by carbon atoms as depicted in Figure 2-10a. Depending on the distribution of carbon atoms C, the lower carbide W_2C

can be disordered at elevated temperature or ordered at a low temperature. The presence of several types of carbon atoms distribution causes the possibility of the formation of several structural modifications of W_2C . Another modification of W_2C has been detected and designated as ε - W_2C [Figure 2-10b (4)]

Higher (with higher C content) carbide WC with hexagonal structure is designated as δ -WC [Figure 2-10d]. Furthermore, the compositions between lower and higher tungsten carbides include the cubic phase γ - WC_{1-x} (designated also as simply WC_{1-x}) [Figure 2-10c]. At present, cubic carbide γ - WC_{1-x} is considered as a structural modification of higher WC carbide.

Table 2-5 reports the existence regions relative to the phase diagram depicted in Figure 2-9, all the lattices constants, the space group, the Pearson symbol and the lattice type and symmetry.

In crystallography, space groups are also called the crystallographic or Fedorov groups, and represent a description of the symmetry of the crystal. Pearson symbol is a method of describing the crystal structure: the two letters specify the Bravais lattice (lower-case letter specifies the crystal family and upper-case letter the centering type), the number represent the number of atoms in the unit cells.

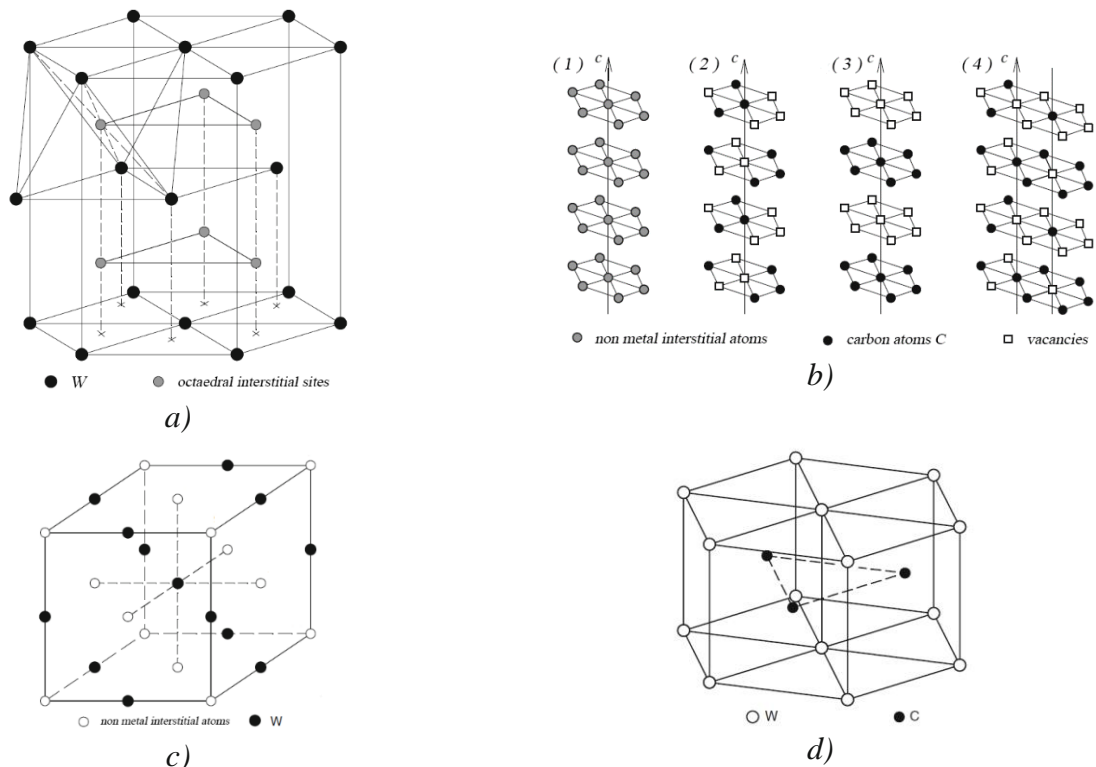


Figure 2-10: Representation of the crystallographic structures of the different WC carbides. a) Hexagonal structure of the $L'3$ -type of lower disordered β - W_2C carbide. The octahedral interstitials \bullet are randomly occupied by carbon atoms C with a probability of 1/2; b) Distribution of carbon atoms in lower carbides β - W_2C (1), β' - W_2C (2), β'' - W_2C (3) and ε - W_2C (4). Tungsten atoms W are not shown. The positions of nonmetal interstitial atoms \bullet are randomly occupied by carbon atoms with a probability of 1/2; c) The B1-type (NaCl) structure of cubic carbide γ - WC_{1-x} . d) Hexagonal structure of higher δ -WC (WC) [19].

Table 2-5: Crystal structure of phases in the W–C system at $T > 1300$ K. Designations as in Figure 2-9 [19].

Phase	Existence region (at%)	Lattice constants (nm)	Space group	Pearson symbol	Lattice type and symmetry
Qusongite (not in diagram)	—	$a=0.902, c=2.831$	$P\bar{6}m2$		
W	0–1.0	$a=0.3165$	$Im\bar{3}m(O_h^9)$	$cI2$	A2 (W type), bcc
β -W ₂ C	~25.5–34.0	$a=0.3002, c=0.475-0.476$	$P6_3/mmc (D_{6h}^4)$	$hP3$	L'_3 (W ₂ C type), hexagonal
β' -W ₂ C	~29.5–33.0	$a=0.4728, b=0.6009, c=0.5193$	$Pbcn (D_{2h}^{14})$	—	PbO ₂ or Mo ₂ C (ζ -Fe ₂ N) type, orthorhombic
β'' -W ₂ C	~29.5–32.5	$a=0.2985, c=0.4717$ (WC _{0.41}), $a=0.3001, c=0.4728$ (WC _{0.50})	$P\bar{3}m1 (D_{3d}^3)$	$hP3$	C6 (anti-CdI ₂ type), trigonal
γ -WC _{1-x}	~37.0–39.5, ~37.1–50.0	$a=0.4266$ (WC _{1.0}), $a=0.4252$ (WC _{0.85})	$Fm\bar{3}m(O_h^5)$	$cF8$	B1 (NaCl type), cubic
δ -WC	~50	$a=0.2906, c=0.2837$	$P\bar{6}m2 (D_{3h}^1)$	$hP2$	B_h (WC type), hexagonal
C	100	$a=0.142, c=0.339$	$P6_3/mmc(D_{6h}^4)$	$hP4$	A9 (C, graphite), hexagonal

In Table 2-6 are collected all the main characteristics of the tungsten carbide from Cambridge Engineering Selector (CES) Software.

Table 2-6: Main characteristics of the tungsten carbide[17].

Density	15300 – 15900 kg/m ³
Young's modulus	600 – 670 GPa
Yield strength (elastic limit)	373 – 530 MPa
Tensile strength	373 – 530 MPa
Elongation	0,06 – 0,09 %strain
Flexural strength (modulus of rupture)	510 – 820 MPa
Fracture toughness	7,4 – 9 MPa*m ^{1/2}
Hardness Vickers	3100 – 3600 HV
Fatigue strength at 10 ⁷	360 – 420 MPa
Melting Point	2820 – 2920 °C
Maximum service temperature	727 – 777 °C
Thermal conductivity	28 – 88 W/m*°C
Specific heat capacity	184 – 190 J/kg*°C
Thermal expansion coefficient	4,5 – 7,1 μ strain/°C
Latent heat of fusion	330 – 370 kJ/kg
Price	17,1 – 26,6 €/kg

2.4 Microstructure of SS316L during Laser Cladding

The thermal cycle of additive manufacturing processes is not comparable to any other types of techniques. This implies that the microstructure is very different from the other manufacturing techniques.

During Laser Cladding process, the material is submitted to a complex thermal history. M.L. Griffith et al. [20] measured the thermal cycle presented in Figure 2-11a. This was obtained by placing a thermocouple in direct contact with a H13 tool steel while printing. Each peak represents the thermocouple response. Figure 2-11b represents computed thermal cycles in first (L1), third (L3), fifth (L5), seventh (L7) and ninth (L9) layers in a nine-layer deposition of 316 stainless steel. Both graphs present that the average temperature of the part increases.

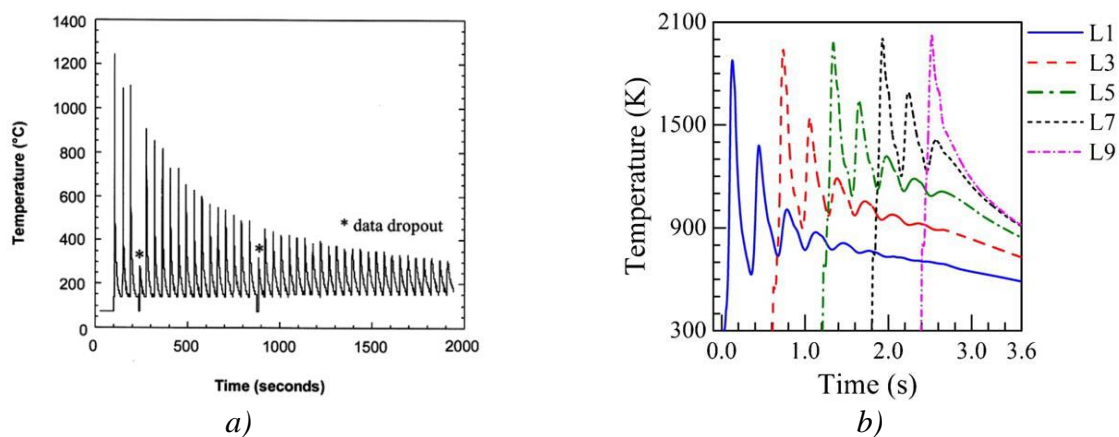


Figure 2-11: Complex thermal history related to additive manufacturing processes. a) [20]. b) [21]

T. Durejko et al. [22] studied the microstructure of laser cladded SS316L. They built a sample of cubical shape: a cross-section [Figure 2-12a] perpendicular to the layers revealed a structure that is characteristic of welded joints. Each scanning by the laser produces an “arc-shaped” configuration [23]. The sequentially overlapping paths form a coherent connection between each layer. This layered structure is typical of additive manufacturing processes. Figure 2-12b show the same layer overlapping, but in AlSi10Mg [24].

In many cases the solidification structure observed in LC presents epitaxial growth in the parallel direction to the of maximum heat conduction direction. The newly solidified layer crystallize in continuity with the previously solidified layers [25]. As the laser is always exposed on the top surface of the solid part, the columnar grains may grow through the melt pool boundary [Figure 2-13b].

Within the laser track, fine cellular and dendritic structures are observed, as shown in Figure 2-13a. Moreover, an increase in distance from the substrate leads to a coarsening of the microstructure. In

fact, heat is retained for longer time in the piece, due to higher thickness [23]. Dislocations and associated residual stresses are concentrated at the cellular boundaries due to the segregation of the heavy alloying elements Mo [26] or Cr [27]. Therefore, the 3D morphology of the cellular structure is well aligned in each columnar grain [26]. Hierarchical macro-, micro- and nano-scale structures are formed in SS316L.

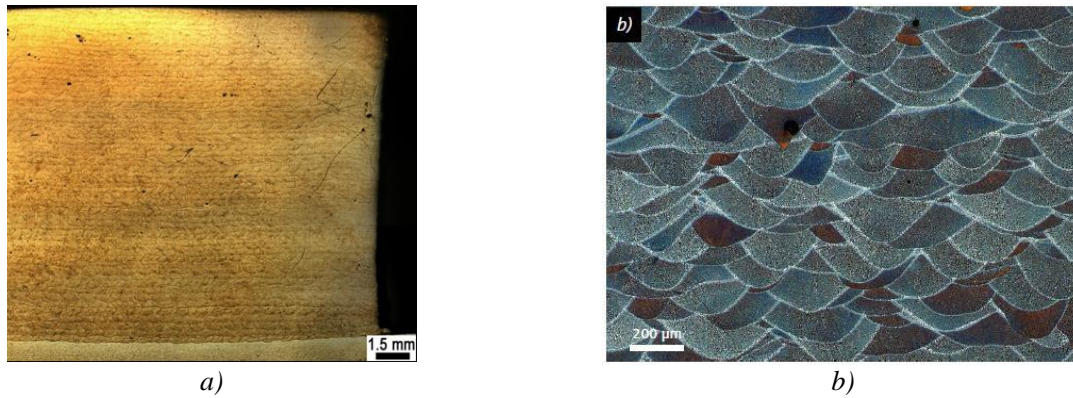


Figure 2-12: Typical layered microstructure obtained with additive manufacturing. a) Optical macrostructure of SS316L produced using LENS [22]. b) AlSi10Mg, SLM, 10%-NaOH etched, longitudinal section, 100× [24].

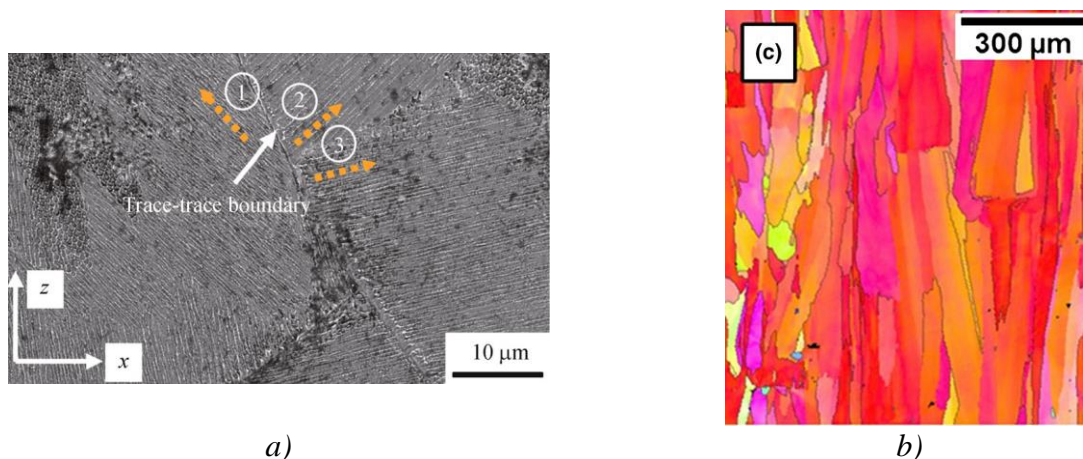


Figure 2-13: a) Fine dendritic microstructure within layered structure [23]. b) Inverse Pole Figure (IPF) maps obtained by EBSD plotted with respect to the building direction [25].

The cooling of a liquid metal implies its solidification. Solidification process occurs in two stages: nucleation and growth. Once nucleation has occurred, solidification proceeds by the movement of an interface (growth). The process may generate heat if the enthalpy of the solid is less than that of the liquid [28]. The microstructure of stainless steels after solidification is influenced by its composition and by the cooling rate imposed. Usually the cooling conditions are very far from the thermal history of the additive manufacturing. The most common solidifications structures observed in metals can be explained considering, as example, the solidification of an ingot of a general alloy.

Ingots are manufactured by the freezing of a molten liquid in a mold. At first contact of the liquid with the cold walls of the ingot, a strong heat dissipation of the liquid occurs, leading to a strong undercooling. The strong undercooling implies an elevated nucleation rate, that incites many randomly oriented crystals to nucleate in the melt. Since the growth of the crystals is very fast, the contact of the solidification fronts readily occurs. The morphology formed in this zone is fine equiaxed (chill zone). Latent crystallization heat, liberating from the crystallizing metal, decreases the undercooling of the melt and decreases the growth rate. At this stage some small grains, having favorable growth axis, start to grow in the direction opposite to the direction of heat flow. This implies a directional growth (dendritic growth) with formation of the primary branches of the dendrites (from the Greek word for “tree”: dendron). A negative temperature gradient is present in the perpendicular direction in respect to the axis of growth of the primary branches: there is the formation of secondary branches. The length of the dendritic zone is determined by the constitutional undercooling. When the temperature of the melt, adjacent to the solidification front, increases due to the liberation of the latent heat, constitutional undercooling will end and the columnar grains growth will stop. Further cooling of the molten alloy in the central zone of the ingot will cause formation of large equiaxed grains [15].

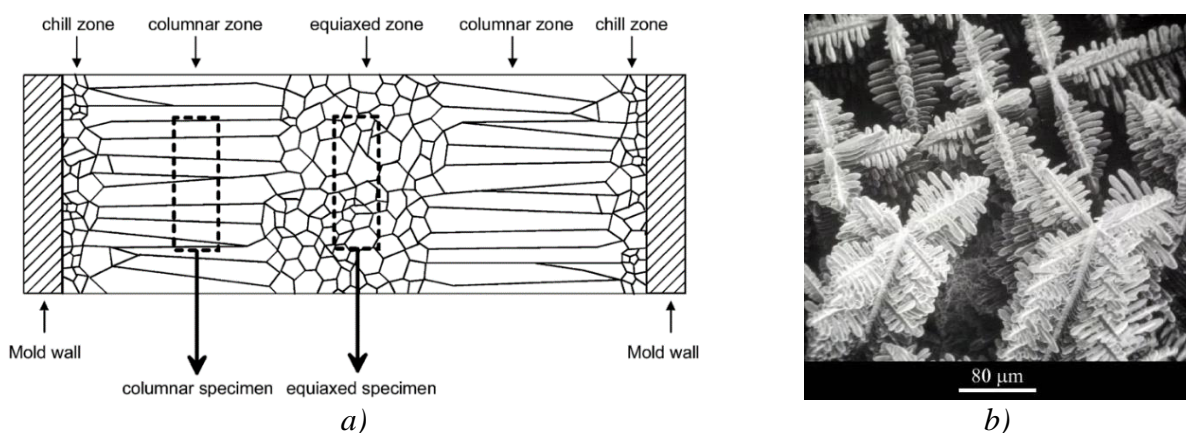


Figure 2-14: a) Schematic representation of the structure of solidification of an ingot [29]. b) SEM image of a dendritic solidification morphology [30].

The meaning of the Greek word for dendrite gives an appropriate description of their shape. In fact, the form and the structure of a metallic dendrite is often described as that of a tree [Figure 2-14b], with a main branch or trunk, from which grow side branches, from which grow smaller side branches, and so on, until all the main branches and the side branches grow into each other and there is no space for any more branches to grow. The shape and the size of these dendrites are all factors that influence the final properties (mechanical, chemical and electrical) of cast and welded materials.

In the following, the main reactions that occur during cooling of a typical SS316L are described.

Precipitation of primary delta ferrite from liquid ($L \rightarrow L + \delta$)

The solidification process can, for certain compositions and cooling rates, begin with the formation of delta ferrite (δ). δ -ferrite forms from the liquid in the form of primary dendrites. The amount and distribution of δ -ferrite is strongly affected by the steel chemical composition, but less affected by the cooling rate [31-34].

Formation of austenite through peritectic reaction ($L + \delta \rightarrow \gamma$)

With decreasing temperature, C segregates to the liquid, leading to the stabilization of the austenite (γ). γ precipitates at the δ/L interface as the product of the peritectic reaction. The chemical composition and the cooling rate during solidification strongly affect the starting temperature of the peritectic reaction. This temperature increases with an increase in C content and decreases with increase of the V, Mo and W contents. These effects come from the fact that C enlarges the γ stability field, while V, Mo and W enlarge the ferrite stability field [33, 34].

2.5 Phases formed by reaction between 316L Austenitic Stainless Steel and WC

Metal matrix composites (MMC) are very common abrasion resistant materials. The basic structure contains a relatively soft matrix and a harder phase that provides high abrasion resistance. There are two basic metallurgical ways to achieve such a structure: the hard phase can be generated through segregation from molten metal or the hard phase can be introduced into the matrix [35]. Various reaction could occur between the introduced hard particles and the steel with the formation of several types of carbides. A carbide is a compound composed of carbon and a less electronegative element. Carbides often forms in high alloyed steels while exposed to high temperature for a certain amount of time.

Mainly three types of carbides can be distinguished. (1) Primary carbides, that forms directly from the liquid phase during solidification; (2) eutectic carbides, that forms from the liquid but together with another phase (example: cooperative solidification); (3) secondary carbides, that precipitates after the solidification has ended, usually after a thermal treatment [15].

In the following, the reactions that occur during cooling are described.

Formation of eutectic carbides through eutectic reaction ($L \rightarrow \gamma + M_xC_y$)

After the γ formation, the residual interdendritic liquid enriched with C and carbide former elements, leads to the formation of three types of carbides (M_2C and/or M_6C and MC) by the eutectic reaction of $L \rightarrow \gamma + \text{Carbides}$. MC carbides normally nucleate and grow by the eutectic decomposition of the last remaining liquid, while M_2C and/or M_6C may form at higher temperatures. However, Boccalini et al. [34] have also shown that in non-equilibrium conditions, as solidification obtained by Differential Thermal Analysis (DTA), the reaction forming $\gamma +$ eutectic MC can also occur at higher temperature, before the formation of $\gamma + M_2C$ and/or $\gamma + M_6C$.

In the following, the most common morphologies of the carbides are briefly defined.

M_6C : The morphology of the eutectic M_6C carbide is characterized by the presence of central and secondary platelets of M_6C carbide, as observed in as cast microstructure of M2 steels [Figure 2-15]. The platelets are separated from each other by the γ phase. The letter M in the M_6C corresponds to the elements W, Mo, V, Cr. The crystalline structure of M_6C is fcc and its hardness is around 1500 HV [33].

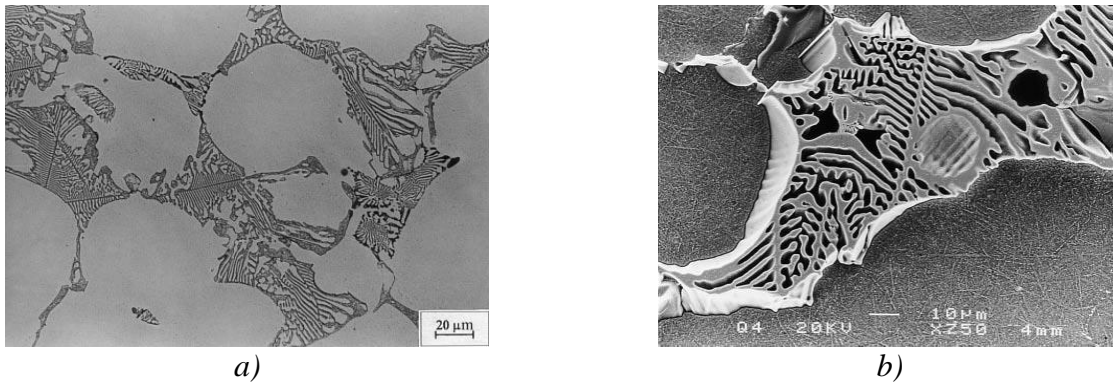


Figure 2-15: Typical morphology of M_6C eutectic in as cast microstructure of M2 steels [34]. a) Optical image: etching $KOH+K_3Fe(CN)_6$. b) SEM image.

M_2C : The morphology of eutectic M_2C carbide may vary depending on the chemical composition and on the cooling rate. Figure 2-16 shows the two main morphological types of the eutectic M_2C : irregular and complex regular. The irregular eutectic M_2C shows a ragged boundary that does not outline the interface between the matrix and the eutectic pool. The complex-regular eutectic M_2C shows a smooth boundary that outlines the interface between the matrix and the eutectic pool. The irregular eutectic M_2C is mainly promoted by a low cooling rate or a high V content and the complex-regular eutectic M_2C is favored by a high cooling rate or a low V content. The crystalline structure of M_2C carbide is hexagonal and its hardness is between 1581-2498 HV [33].

Optical	SEM	
		Irregular
		Complex regular

Figure 2-16: Morphological types of M_2C eutectic [34].

MC: Figure 2-17 shows three morphological types of eutectic MC carbide: divorced MC carbide that forms as isolated massive crystals, irregular MC that is a poorly coupled eutectic with a petallike morphology and complex-regular MC that is a coupled eutectic with a branched petallike morphology. The structure of MC carbide is fcc and its hardness is around 3000 HV.

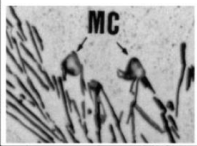
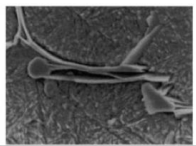
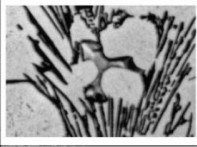
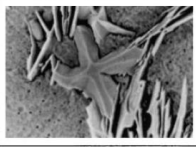

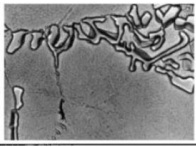
Optical	SEM	Carbide morphology	Eutectic classification
		Idiomorphic	Divorced
		Petallike	Irregular
		Branched petallike	Complex regular

Figure 2-17: Morphological types of MC eutectic [34].

M₇C₃: The morphology of the eutectic carbide M₇C₃ is a very fine rod-like morphology, as shown in Figure 2-18. Rapid solidification and a high amount of Cr are the main causes of the formation of the M₇C₃ carbide [33]. Otherwise, the usual form of M₇C₃ carbide is the primary Cr-rich M₇C₃ carbide, mostly found in hypereutectoid alloys with an orthorhombic crystalline structure.

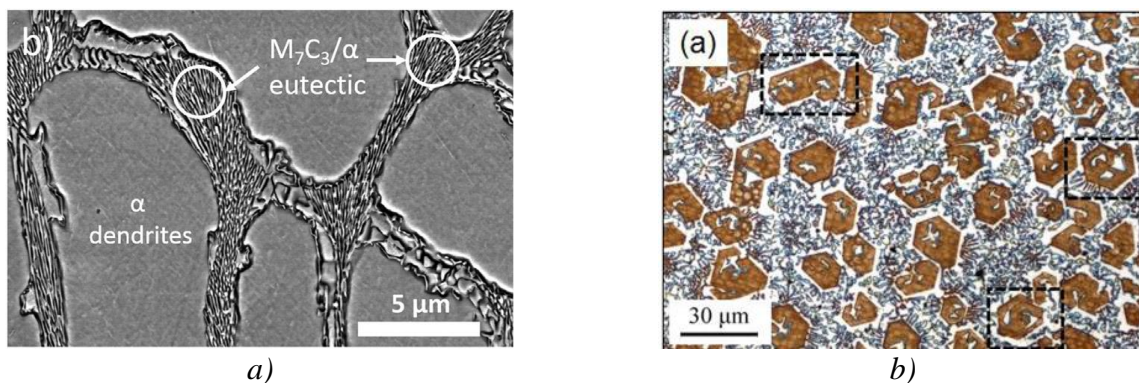


Figure 2-18: Microstructures of a Fe-Cr-C alloys in as-cast state [36]. Dyed OM image of a Fe-Cr-C alloy [37].

M₂₃C₆: This carbide is mainly a secondary carbide in stainless steel and gives sensitization. This process consists in the formation of Cr-rich M₂₃C₆ carbides in stainless steel. While precipitating at the grain boundaries, the carbides subtract chromium from the matrix of the stainless steel. This process causes a loss in corrosion resistance and can occur when welding austenitic steel at T ≤ 900°C [15].

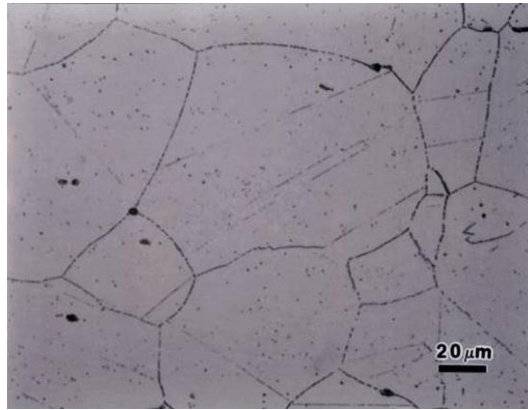


Figure 2-19: Grain boundary sensitization [15].

In the following, other possible phases included are briefly described.

Laves phase: This type of phase is classified on the basis of geometry alone and their composition is of AB_2 type, where A and B are metallic elements. In general, the A atoms are ordered as in diamond, hexagonal diamond, or a related structure, and the B atoms form tetrahedra around the A atoms for the AB_2 structure. A characteristic feature is the almost perfect electrical conductivity, but they are not plastically deformable at room temperature [38].

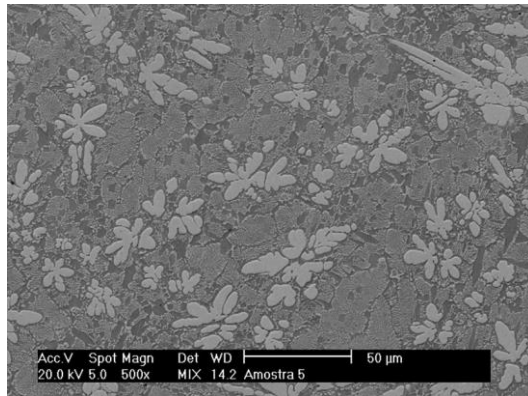


Figure 2-20: Primary and lamellar Laves phases [39]

Sigma phase: In welding of austenitic stainless steel the formation of δ -ferrite occurs. If δ -ferrite remains for long time between 600 and 1000°C, then σ -phase is formed [15]. The formation of σ is mainly favored by Cr and Mo, but also by W and Si, which enlarge its stability field and enhance both the precipitation rate and its volume fraction. The σ -phase is a hard and brittle phase [40].

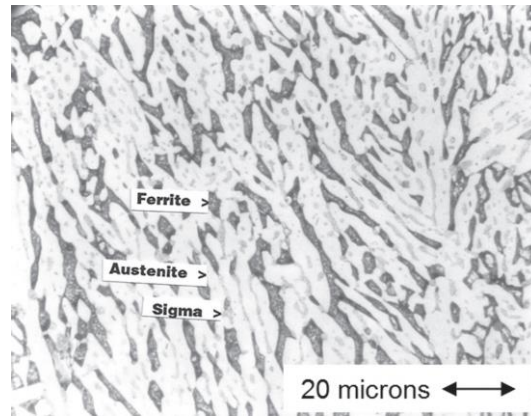


Figure 2-21: Duplex stainless-steel annealed 4 hours at 1040°C, displaying the formation of σ -phase [41].

3 Experimental Methods

3.1 Materials

The starting material to build the deposit is in form of powder. This powder must be as spherical as possible to not damage the dispenser and the nozzle of the machine. If the powder presents an irregular shape, it can cause abrasion in the pipes that carry the powders in the melting zone. The size of the particles is also very important for the good functioning of the machine. Particles smaller than 40 μm could create wear problems because of their small surface creating greater local pressure on the pipes. Moreover, small particles have a high tendency to form cluster and agglomerates. Particles larger than 200 μm , on the other hand, may obstruct the nozzle and plug the pipes.

3.1.1 Analysis on SS316L powder

The SS316L powder is produced by Carpenter Powder Products [42], a company established in Sweden. The specified particle size is between 44 and 105 μm (Annex A). The powder was analyzed using a Scanning Electron Microscope (SEM), in Secondary Electrons (SE) mode to understand the quality of the outer and inner surface and with Energy Dispersive X-ray Spectrometry (EDS) to gain information about its composition. The microscope used is a Philips XL30 ESEM-FEG. Two different sets of samples were prepared: (1) a small quantity of free powder was poured on adhesive tape to characterize the morphology of the particles; (2) a small amount of powder was mixed with conductive embedding resin and polished following standard practices to reveal the inner structure (porosity) of powder particles and allow for investigating its chemical composition.

The composition of the particles has been provided by the industry (Annex A), and matches the nominal composition for SS316L [Table 3-1]. The composition of the powder was measured, with EDS detector, as the average of the composition following a line in the cross section of one single particle. The detector collects x-rays emitted by atoms that had been excited under the action of the electron beam. More precisely, these x-rays are emitted due to the reassessment of the electrons going back to their standard energy level. The detector analyzes the photons x coming from the surface based on their energy in accordance with the Moseley's law.

When a heavy atom is excited, it has a strong tendency to excite the electronic layers of the neighboring lighter atoms, resulting in a possible overestimation of the lighter elements.

Table 3-1: Composition provided by Carpenter Powder Products for SS316L (Annex A).

<i>%wt.</i>	<i>C</i>	<i>Fe</i>	<i>Mo</i>	<i>Ni</i>	<i>Cr</i>	<i>Mn</i>	<i>Si</i>
	<0,03	Bal.	2,00-3,00	10,00-14,00	16,00-18,00	<2	<1

3.1.2 Analysis on WC powder

The WC powder utilized in this research has been provided by Höganäs AB [43], a Swedish company established in Höganäs. The name of the particular type of WC powder is “4590”. It is characterized by spherical particles between 50 and 200 μm (Annex B). This spherical shape is obtained by plasma torch atomization. The production involves the eutectic melting of tungsten and carbon to form the tungsten carbide in the molten state. There are three eutectic reactions in the system between W and C, this implies that Tungsten Carbide can be in three different forms: W_2C , WC_{1-x} and WC (see also section 2.3.2).

The composition as given by the provider is shown in Table 3-2. As for the SS316L powder, the composition of the powders has been measured with the EDS technique. The average composition was determined along a line through a cross section of a particle.

Table 3-2: Composition from Höganäs AB (Annex B).

<i>%wt</i>	<i>C</i>	<i>W</i>	<i>Fe</i>
	4,0	Bal.	0,1

The SEM images shows only a few particles, so we have little information concerning the actual granulometry. Hence, measurements using the laser diffraction technique have been made in order to obtain more accurate information about the size distribution of the whole powder. This test was conducted by APTIS, Faculty of Science, University of Liege.

The cleaned WC powder was suspended in 40 ml of water-Daxad 11 (additive) solution. A Malvern Mastersizer 2000 [Figure 3-1] has been used to measure the granulometry of the powder. This machine is based on the Fraunhofer Diffraction theory, stating that the intensity of light scattered by a particle is directly proportional to the particle size. The angle of the laser beam and particle size have an inversely proportional relationship, where the laser beam angle increases as particle size decreases and vice versa.



Figure 3-1: Malvern Mastersizer 2000 [44].

3.2 Sample fabrication

3.2.1 Cladding Machine

The additive manufacturing technique utilized to build the samples is Laser Cladding. The samples have been produced by Sirris [45] and the machine utilized is the DUOCLAD VI LF 2000 [Figure 3-2]. This machine has been developed by BeAM [46] and uses the CLAD (Direct Laser Additive Construction) process, developed by IREPA LASER [47]. The raw powder is projected through a nozzle placed coaxially to the laser beam. In this machine, the nozzle-laser assembly is placed on five axes that are controlled digitally. Sirris has two kinds of laser sources: the MesoCLAD allowing the creation of cords between 0.8 and 1 mm ($15 \text{ cm}^3/\text{h}$) and the MacroCLAD for cords of 2 mm ($250 \text{ cm}^3/\text{h}$). The machine has two fiber lasers with different maximum power: 300 W and 2000 W [4].



Figure 3-2: Cladding Machine DUOCLAD VI LF 2000 (five axes) [1].

The fiber lasers belong to the group of solid-state lasers (together with the crystals lasers). The fiber lasers, with a wavelength of 1 μm , produce a very small spot. So, they achieve an intensity up to 100 times more than a CO₂ laser with the same average power. Fiber lasers do not require any maintenance and they distinguish themselves by their very long working life of at least 25.000 hours.

Table 3-3 presents the laser parameters utilized to build the samples analyzed in this work.

Table 3-3: Characteristics of the laser used and parameters utilized to build the sample [1].

<i>Model and Label of the Laser</i>	YLS-2000-CL, IGP
<i>Nominal Power</i>	2000 W
<i>Efficiency</i>	28%
<i>Wavelength</i>	1070 \pm 10 nm
<i>Input fiber diameter</i>	100 μm
<i>Input fiber length</i>	5 m
<i>Process fiber diameter</i>	600 μm
<i>Process fiber length</i>	10 m
<i>Glass fiber activator (dopant)</i>	Ytterbium
<i>Excitation source</i>	Pumping diodes
<i>Cooling Capacity</i>	9.3 kW at 33 °C

The inert gas utilized as carrier gas is Argon. It has the additional functions of protecting the deposit from oxidation and shaping the powder flux.

Practically, there are three different circuits [Figure 3-3] for Argon:

- The *central gas* protecting the laser from the rising fumes, which could cause the laser to fail.
- The *carrier gas* whose function is to transport the powder.
- The *shape gas* that is responsible for shaping the cone of powder.

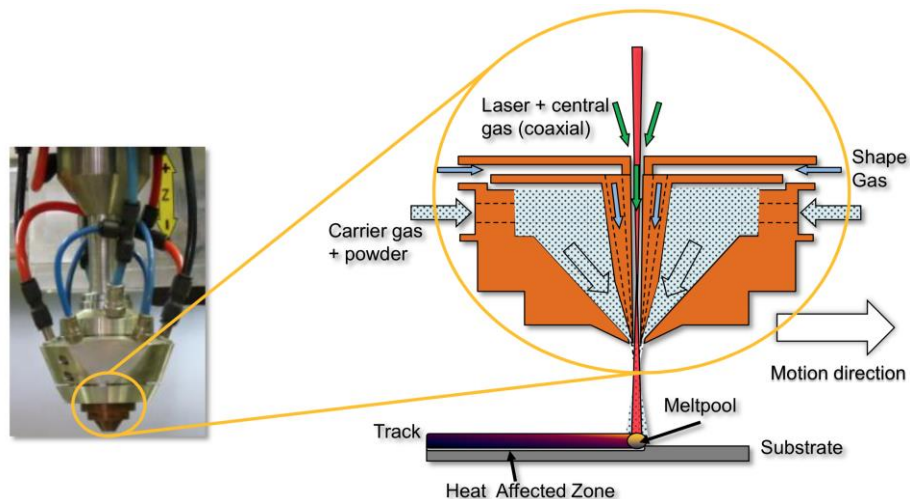


Figure 3-3: Coaxial nozzle by IREPA [1].

In order to obtain a composite coating, there must be two different materials. For this aim the cladding machine is equipped with a double powder feed: MediCoat DUO [Figure 3-4]. The powder is continuously fed through a turntable [Figure 3-5]. The speed of the turntable defines the volumetric quantity of powder (cm^3/min) or, using the bulk density of the powder, the weight feed rate of powder (g/min). The powder intake is very difficult to control and requires a lot of attention. In fact, with the working of the dispenser, the powder rate can change. It is therefore necessary to check regularly the exact powder flow. A good functioning of the dispenser is owed to the quantity of gas, the distribution of the gas through the inner circuits, the type of powder utilized and the speed of the turntable.

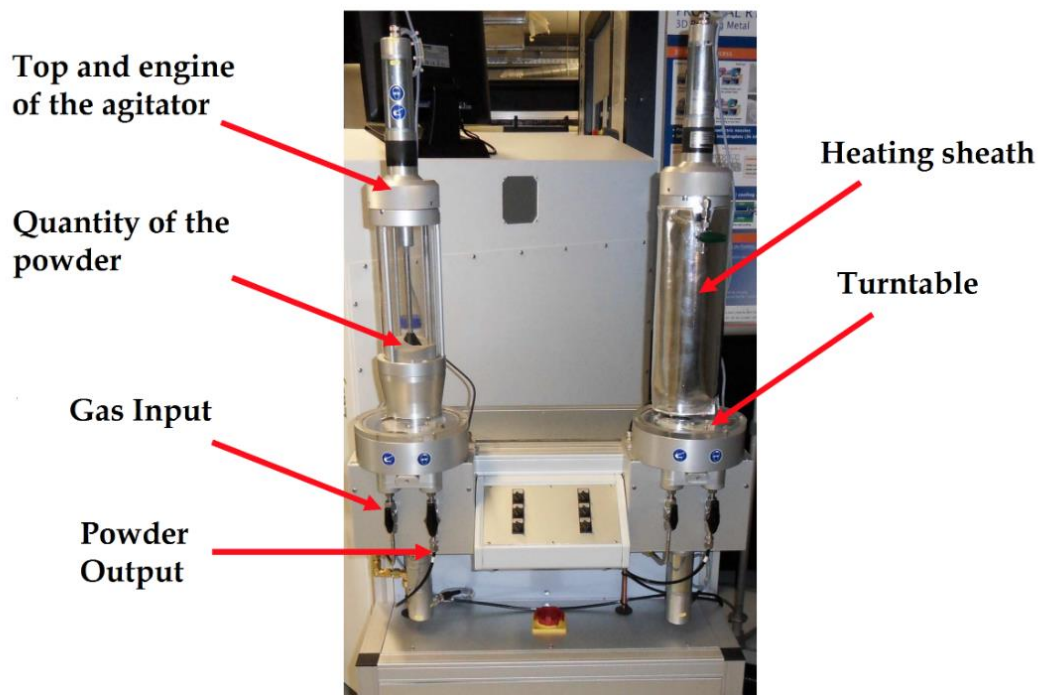


Figure 3-4: Powder Dispenser MediCoat DUO [1].

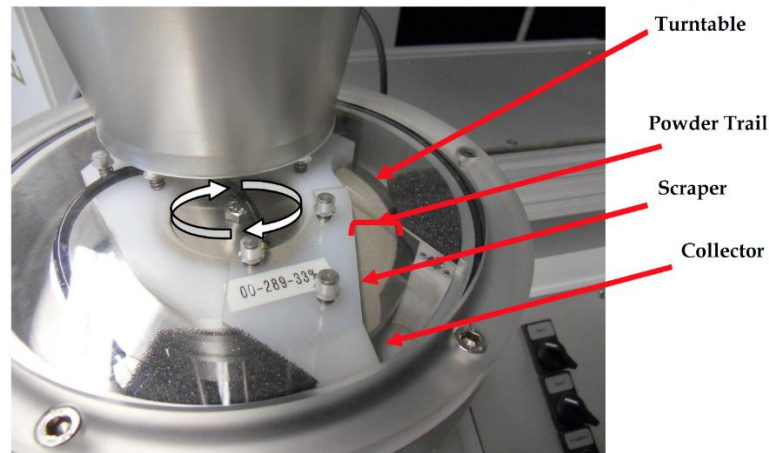


Figure 3-5: Turntable, displaying the scraper and the collector [1].

3.2.2 Parameters for the realization of the samples

- *Nozzle Parameters:* In order to produce high quality bead to obtain a suitable coating, the geometry of the flux of powder projected on the substrate must be controlled. This is called “cone”. It should neither be too long nor too short, ensuring that the powder arrives as concentrated as possible into the melt pool. For the present samples, the length of the cone is 10 mm. As described, the cone is characterized by three gas flows (shape, central and carrier) and by the characteristics of the powders. Moreover, there is a minimum amount of carrier gas, to avoid the locking of the powders in the pipes. Table 3-4 reports the amounts of the three kinds of gas flows used to build the samples.

Table 3-4: Parameters for the nozzle.

<i>Sample Type</i>	<i>Central gas (l/min)</i>	<i>Shape gas (l/min)</i>	<i>Carrier gas – SS316L (l/min)</i>	<i>Carrier gas – WC (l/min)</i>
<i>SS316L without addition of ceramic particles</i>	1	6	2.5	—
<i>SS316L with WC particles</i>	4	7	1.2	2.5

- *Powder Flow Rates Parameters:* The quantity of powder supplied to the melt pool [Table 3-5] must be checked regularly, due to drifts observed in the dispenser. If the powder flow rate is insufficient, less powder is deposited which implies that some of the energy of the laser beam is absorbed by the layer underneath. The excess energy will be stored in the piece, rising its average temperature. On the contrary, an excessive amount of powder will result in a too thick

layer, reducing the length of the cone. In addition, energy could be insufficient to melt all this powder creating porosity.

Table 3-5: Flow rates of the powders.

<i>Sample Type</i>	<i>Flow rate of SS316L powder (g/min)</i>	<i>Flow rate of WC powder (g/min)</i>
<i>SS316L without addition of ceramic particles</i>	2,7 (20% of the maximum speed of the turntable)	—
<i>SS316L with WC particles</i>	2,7 (20% of the maximum speed of the turntable)	Variable for the different samples

- *Control of Laser Power and Feed Speed:* The control of the laser power and of the feed speed affects the energy supplied to the powder. This affects the deposit shape and influences the microstructure. Insufficient energy leads to delamination of the adjacent tracks because of the lack of overlapping with the previous layer. Too much energy may lead to material oxidation. Moreover, when the laser power is below a certain value the cords tend to be discontinuous. These parameters [Table 3-6] have been used as a basis to produce the samples containing tungsten carbide, with some adaptation.

Table 3-6: Control Laser Power/feed speed

	<i>Range</i>
<i>Laser Power (W)</i>	500 – 680
<i>Feed speed (mm/min)</i>	270 – 290

- *Layer Thickness:* The target distance between the nozzle and the piece is 10 mm. Consequently, for each new layer the nozzle must ascend by a certain height away from the piece. This shift along the Z-axis must be equal to the height of the previous layer. Unfortunately, the amount of material deposited and the height of the beads is not constant. Actually, when the first layer is deposited, the heat is rapidly drawn away from the substrate and the support. However, when the number of layers increases, the heat accumulates in the material. This phenomenon changes the thickness of the deposited layers. The increment for each new layer was fixed at 700 µm.
- *Tracks Offset:* In making each layer, the distance of deposition between the tracks, in X and Y directions, must also be considered. Tracks are placed without spacing in between. This allows to produce less porous and more resistant pieces, because of the better overlapping of

the strands along the same layer. Hence, when making a sample it is necessary to know the width of the strands to calculate the spacing. This width depends on the type of material, the powder flow rate, the feed speed and the laser power. Still, it is possible to have small cavities between the tracks [Figure 3-6]. Typically, the spacing between the tracks is 30% less than the width. For the SS316L and the parameters described above, the cord width is of 2 mm, so the nozzle offset for each new strand is 1.4 mm.

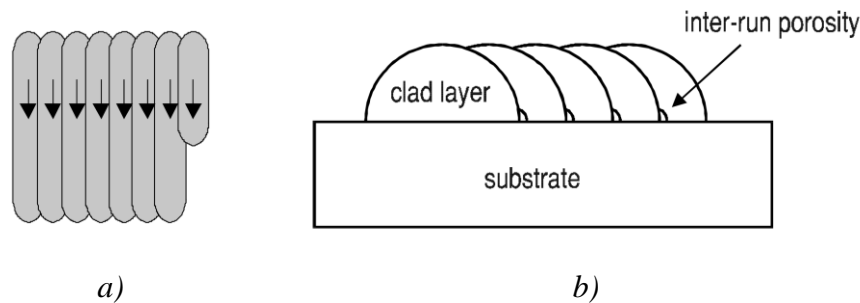


Figure 3-6: a) Schematization of the deposition of the strands [1]. b) Position of the porosity between the tracks [1].

The samples analyzed in this work have been made using ISO codes on a conventional CNC (Computer Numerical Control) machine.

3.2.3 Samples examined in this work

Two types of samples have been produced: (1) containing only 316L Stainless Steel, of cubical shape, with dimensions $25 \times 20 \times 10 \text{ mm}^3$, (2) with addition of WC powder, of cubical shape, with dimensions $20 \times 20 \times 10 \text{ mm}^3$.

- *SS316L samples*

These samples [Figure 3-7], composed only of SS316L, were made in order to obtain the basic parameters for future additions of ceramics. These samples were manufactured by “crossed” strategy: each layer was made with a rotation of 90 degrees. The contouring speed is 270 mm/min, the internal tracks were made at a speed of 290 mm/min. The heat accumulation does not affect the distance with the nozzle, that remains constant during fabrication. Hence, each new layer has a height of 700 μm .

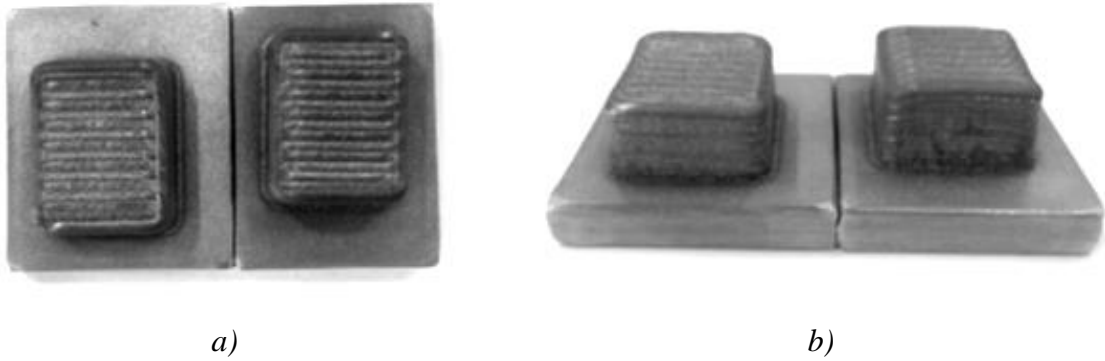


Figure 3-7: Samples realized in SS316L [1]. a) Top view. b) Lateral view.

- *SS316L with WC samples*

The fabrication parameters are the same as for the SS316L. Only the quantity of tungsten carbide varies [Figure 3-8].

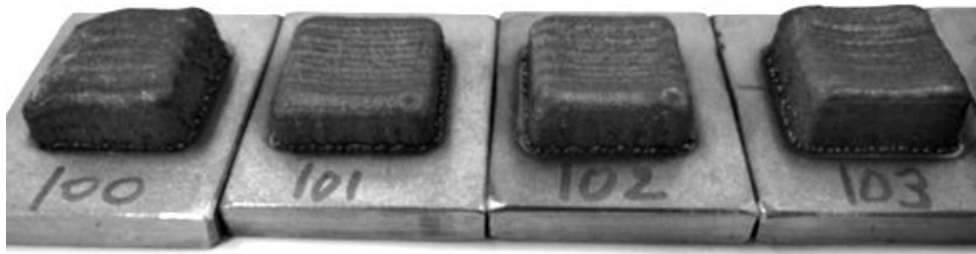


Figure 3-8: Samples of SS316L+WC analyzed [1].

Table 3-7 summarizes the denomination of the samples and all the data for their production. The names have been chosen referring to the weight percentage of the WC powder in the deposit.

Table 3-7: Production parameters [1] and name of the different samples.

316L (%)	WC (%)	316L (g/min)	WC (g/min)	Volumetric percentage of WC in SS316L	Weight percentage of WC in SS316L	Old name (as in Figure 3-8)	New name
20	0	2,7	—	0	0	P8	W0
20	15	2,7	1,02	16	27	P101	W27
20	30	2,7	2,04	28	43	P102	W43
20	45	2,7	3,06	36	53	P103	W53
20	65	2,7	4,42	47	62	P100	W62

3.3 Microstructural characterization

3.3.1 Optical microscope and Stream Analysis Software

The first step is the samples preparation. First, the samples were cut then embedded in phenolic resin using a Struers CitoPress 1 machine. The temperature used for curing the resin was 180°C. After embedding, the samples were polished using a Struers Tegramin-30 polisher, first with SiC papers with 80 to 1200 grits, then with a diamond suspension (particle diameter from 9 to 1µm), in order to obtain a mirror polished surface. Finally, the samples have been treated with an Oxide Polishing Suspension (OPS), that is composed of colloidal silica. The samples were observed with an Olympus BX60M microscope. The embedded samples are displayed in Figure 3-9.

First, overviews of the whole surface of the cross-section of the samples SS316L with WC were taken at 25x of magnification. The overviews were then processed with image post processing open source software GIMP 2 [Figure 3-10] to underline the particles. The Stream Analysis software was used to analyze the processed pictures to understand the position of the particles in the deposit, both along y and x direction (see section 4.2.1.1). Y represents the direction parallel to the building direction of the “as built” sample, while x represents direction parallel to the width of the sample. The particles’ surfaces were also measured in the cross-section of the sample. The surface of the samples was then observed with polarized light using the prism Olympus U-DICR at different magnification, up to 100x, to observe the zone between the particles and the matrix.

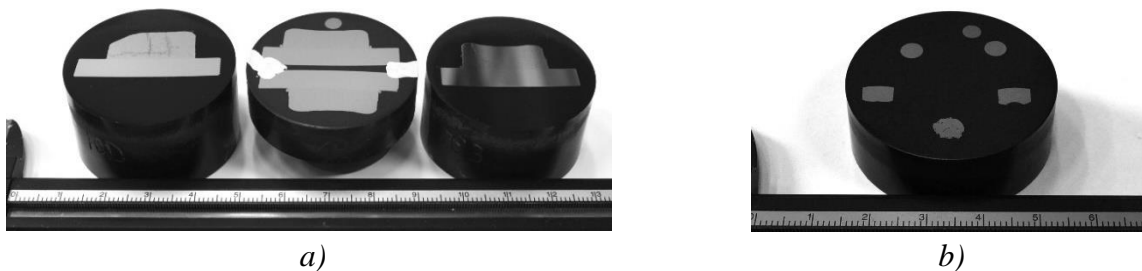


Figure 3-9: a) Samples laser cladded SS316L+WC. b) Samples after DTA.

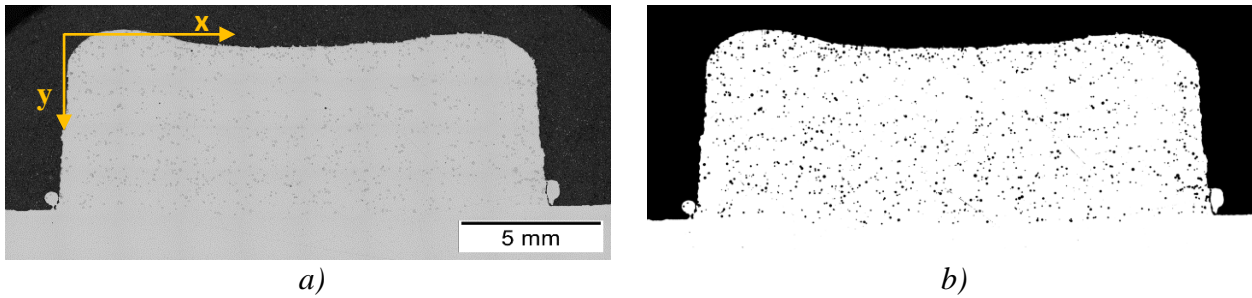


Figure 3-10: Example of the image post processing to evaluate the particles position and surface in the composite material. a) Overview of one of the samples. b) Photo after post processing.

3.3.2 Scanning Electron Microscope

Observations were carried out with a Phillips XL30 FEG-ESEM in order to understand the reaction between the ceramic particles and the metallic matrix.

Images were taken in Secondary Electrons mode for direct observation. Profiles composition were obtained with EDS (Energy Dispersive Spectrometry) to better understand the composition of the various zones of the microstructure. EBSD (Electron Backscattered Diffraction) analysis were carried out to determine the crystallographic lattices of the different zones.

Sample preparation was similar to the one used for optical analysis. Only the resin was different: it was a phenolic resin made conductive by adding a carbon filler. The conductivity of the resin is required to avoid the accumulation of electrical charges on the sample during the observation. Moreover, two tracks were painted with a silver painting to enhance the evacuation of electrical charges during EBSD analysis. For this observation, the samples were placed on a special support, to ensure that the sample does not move when it is tilted to an angle of 70° .

3.4 Thermo-Calc Equilibrium Software

Thermo-Calc is a software package for the calculation of thermodynamic and phase equilibria. In conjunction with suitable thermodynamic databases, assessed using the CALPHAD approach, Thermo-Calc can be used for a wide variety of applications. Thermo-Calc simulations can be divided in two types: equilibrium and pseudo-equilibrium conditions. Pseudo-equilibrium conditions refer to simulations of non-equilibrium conditions, but its accuracy is limited.

In this study, Thermo-Calc has been used for two simulations: (1) to simulate the solidification steps for the SS316L and for compositions between the SS316L and WC, through the Advanced SCHEIL Module; (2) to calculate a phase diagram of the SS316L varying the quantity of Tungsten and Carbon. These simulations have been useful to understand the solidification structures in the samples and helpful to set the maximum temperature of DTA tests. Moreover, to understand the solidification range.

3.5 Thermal Analyses

Differential Thermal Analysis (DTA) and Differential Scanning Calorimetry (DSC) were performed with the NETZSCH STA 449C, following standard DIN 51 007, and with the NETZSCH DSC 404C, respectively. The difference of temperature between the sample and the standard is measured by means of thermocouples and first expressed in μV (thermal voltage). In the DSC the difference of temperature is then converted into a heat flux, expressed in mW, but not in the DTA.

In this study DTA was applied to determine the decompositions and precipitations of the various phases in the material considered. DSC was used to obtain confirmation of the information from the DTA. In fact, DSC has more precision and higher sensitivity. DTA was firstly chosen to carry out the tests because it is easier to perform tests on molten metals: DSC crucible is very small and there is the risk of the molten metal to overflow. Table 3-8 summarizes the conditions of the thermal tests performed on sample W27.

Table 3-8: Thermal tests description.

Analysis	Temperature Range [$^{\circ}\text{C}$]	Heating/Cooling rate [$^{\circ}\text{C}/\text{min}$]	Name of sample after DTA and of the DTA/DSC test
DTA	TR — 1500	5	DT1
	TR — 1500	1	DT3
	TR — 1200	5	DT4
DSC	TR — 1200	5	DS4

Precise dimensions are required for the samples: these must be of 5 mm diameter to appropriately fill the crucible. Figure 3-11 shows the dimensions and the positions in which the sample were cut to obtain the samples for thermal analyses. A cylindrical sample of 20 mm length was extracted via electro erosion. This cylinder was then cut to obtain 5 mm long samples for the DTA tests and 2 mm long samples for the DSC test. The most external part of the sample has been cut off to avoid variation of precipitated/dissolved phases due to some edge effect.

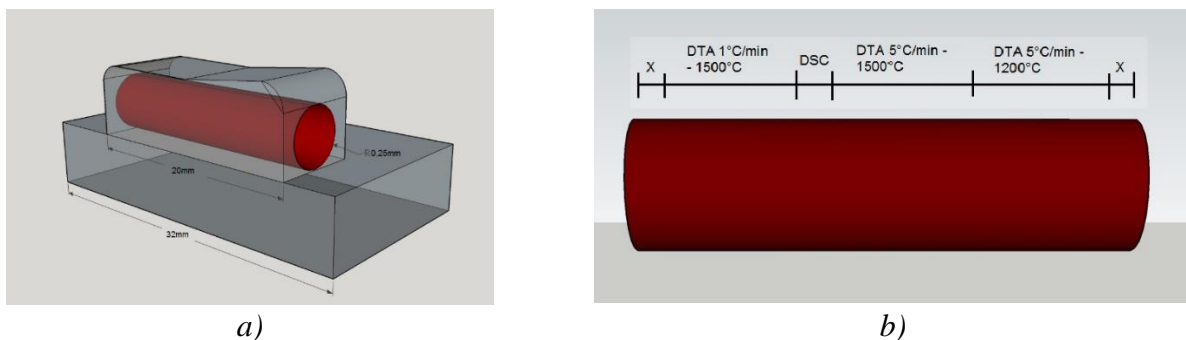


Figure 3-11: Realization of the DTA samples. a) Extraction of the carrot from the sample. b) Cutting zones.

A DTA analysis of a SS316L sample fabricated by the additive technology known as SLM (Selective Laser Melting) has been performed as a reference, at a rate of 5 °C/min up to 1500 °C. The thermal cycle imposed in SLM is close to the thermal history during laser cladding, and both processes result in comparable microstructures.

After thermal analyses, the microstructures of the samples have been observed, following same procedure as for the “as built” samples. Firstly, the samples were cut and embedded in conductive resin. Secondly, the surface was mirror and OPS polished. Thirdly, using the optical microscope the overall surface was observed. Finally, direct observations with SEM through Secondary Electrons (SE) and EDS analyses were carried out.

3.5.1 General rules for reading DTA thermograms

- The peak of a phase transformation may be endothermic or exothermic, depending on whether the phase transformation absorbs or releases heat.
- For a given peak, only the first slope is considered to determine the characteristic temperatures of the beginning and the end of the transformation. The second slope corresponds to a relaxation phenomenon that has no physical significance for the phase transformation [Figure 3-12a].
- The point where the peak starts deviating from the baseline indicates the onset of a phase transformation. The transformation ends when the considered peak reaches the maximum of its amplitude [Figure 3-12a].
- When several peaks are superposed in the same temperature range, a deconvolution allows to distinguish these peaks, even if this operation remains delicate [Figure 3-12b] [33].

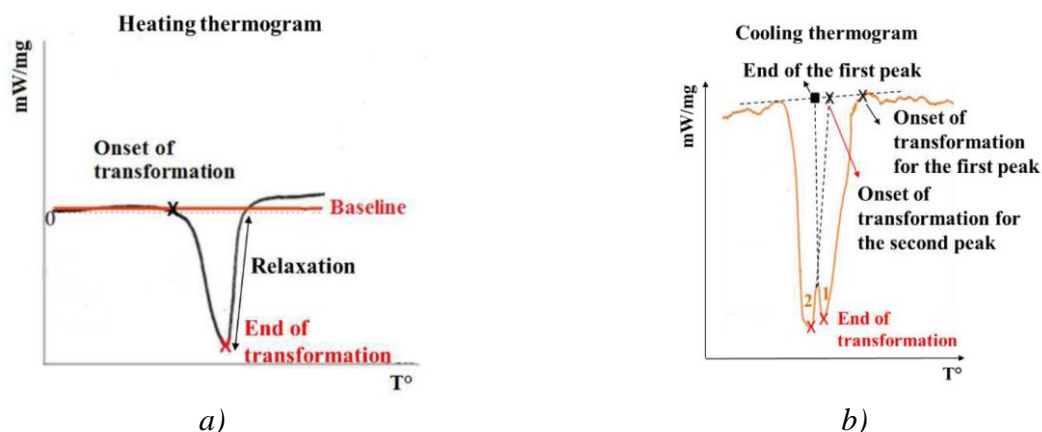


Figure 3-12: DTA thermograms showing [33]: a) temperature of onset and end of transformation for a simple peak b) deconvolution to distinguish separately two superimposed peaks.

3.6 Nanohardness Tests

The machine used is the TI 950 Triboindenter nanoindenter by Hysitron [Figure 3-13]. The machine works in two modalities: load control modality and displacement control modality.

Nanohardness tests have been performed in order to understand the hardness evolution between the SS316L matrix and the WC particles, in the dissolution zone of WC in SS316L. For this purpose, nanoindentations have been made at a controlled depth of 300 nm, following a grid 3x5 from the inside to the outside of the WC particle. In order to check the position of each indentation a scan by SPM imaging has also been performed.



Figure 3-13: TI 950 Triboindenter by Hysitron [48].

4 Results

4.1 Powder Characterization

This first section of this chapter presents the analyses made on the powders. SEM observations and EDS analyses have been conducted to detect the shape and the composition of both SS316L and WC powders. Furthermore, the granulometry of the tungsten powder was analyzed.

4.1.1 Stainless Steel 316L powder

Direct SEM observations have been performed on the SS316L powder. The particle size has been observed to be generally between 40 μm and 100 μm , as specified by Carpenter Powder Product. The surface of the particles is generally spherical and presents some roughness [Figure 4-1a]. Some particles are stuck together, especially the finer ones are stuck to the larger ones. The finer ones are called “satellites” [Figure 4-1b]. The particles are found to be fully dense. However, when finer particles stick to larger ones some porosities can be present [Figure 4-1c].

In Table 4-1 the composition of the SS316L powders is presented. Carbon, as a light element, is overestimated by the EDS probe. All the other elements are in agreement with the nominal composition.

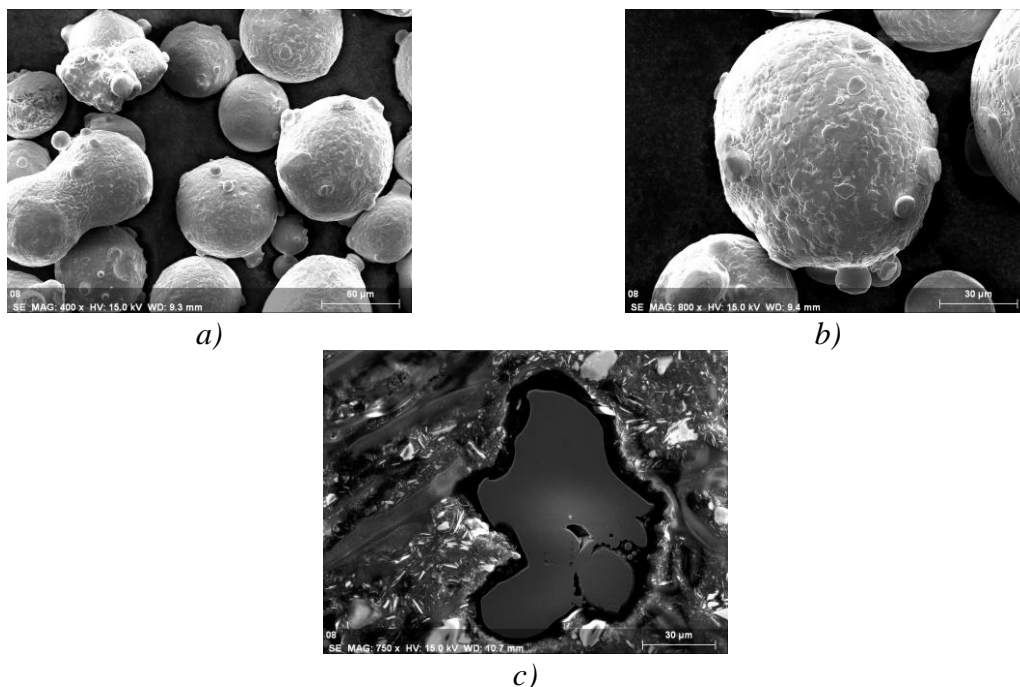


Figure 4-1: SEM images of SS316L particles. a) Particles surface. b) Particularity of the surface. c) Cross-section of the particle. [1]

Table 4-1: Composition of SS316L calculated with EDS in weight percent.

wt%	C	Fe	Mo	W	Ni	Cr	Mn	Si
Average	2,52	67,96	1,77	0,17	9,46	16,26	1,51	0,36
Standard Deviation	1,42	1,88	0,51	0,42	0,80	0,93	0,40	0,17

4.1.2 WC powder

The WC powder has been observed with the SEM microscope, in order to study the shape and the surface of the particles. The Figure 4-2a reveals the powder to be spherical and smooth in appearance. In Figure 4-2b an image of the surface of a single particle is shown, reveals that the surface is not perfectly smooth.

The composition of the WC powder is measured by EDS, as reported in Table 4-2.

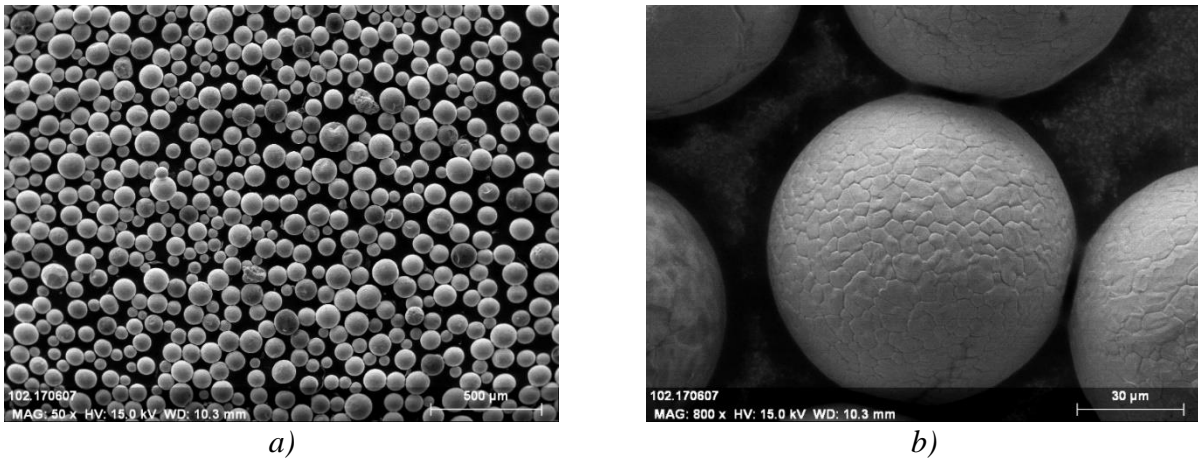


Figure 4-2: SEM images of WC particles. a) Particles surface. b) Particularity of the surface.

Table 4-2: Composition of WC calculated with EDS in weight percent.

wt%	C	W	Fe	Mo
Average	13,84	85,91	0,24	0,01
Standard Deviation	4,94	5,04	0,29	0,06

A granulometry test was carried out by APTIS. The output of the Malvern Mastersizer 2000 is shown in Figure 4-3. The size dispersion is from 60 μm to 200 μm, in accordance with the data provided by Höganäs AB. The range of particles size measured by the machine is narrow. Therefore, the dispersion of the particles size is satisfactory for the use in this case study.

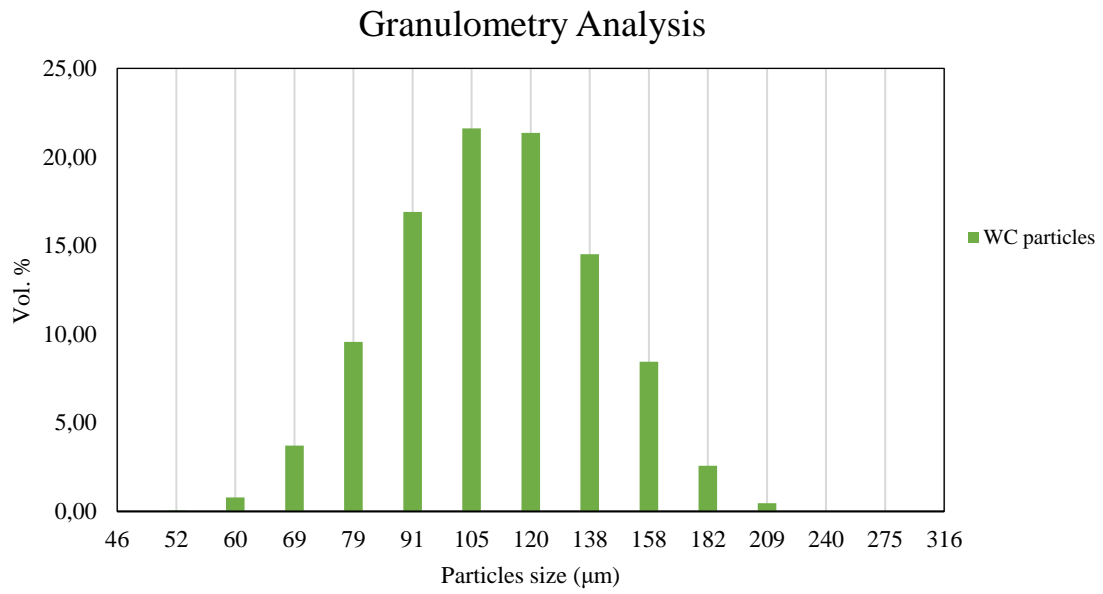


Figure 4-3: Output of the granulometry test on the WC particles.

4.2 Microstructural Characterization

4.2.1 Additive Manufacturing conditions

4.2.1.1 Optical observation of the particles distribution in the clad deposit

The aim of this part of the analysis was to study the distribution of the reinforcement inside the composite material. The main information investigated was the position of the particles in respect to the substrate (*y axis*). Other characteristics such as the distribution of the particles along the *x axis*, the particles surface variation along *y* direction and the fraction of the reinforcement in the cross-section were also obtained. Image processing could have brought some measurement imprecision. The samples analyzed were: W27, W43, W53 and W62 [Table 3-7]. For each sample, in the following data are presented: the general overview, the original WC particles map, the quantification of the particles in 100 μm thick layer, both in *y* and in *x* direction and the surfaces quantification of the particles, in *y* direction, in 100 μm layer.

- The general overviews were the starting point for all the analyses. The overviews of the samples with the reference axes are shown in the following pictures [Figure 4-4 to 4-7].
- The maps were obtained with Stream Motion Software by Olympus. It is a method to understand the position of the center of each particle combining the *x* value with the *y* value. The map of the original WC particles is compared with the original picture to check that the particles are correctly identified and delineated [Figure 4-4 to 4-7].

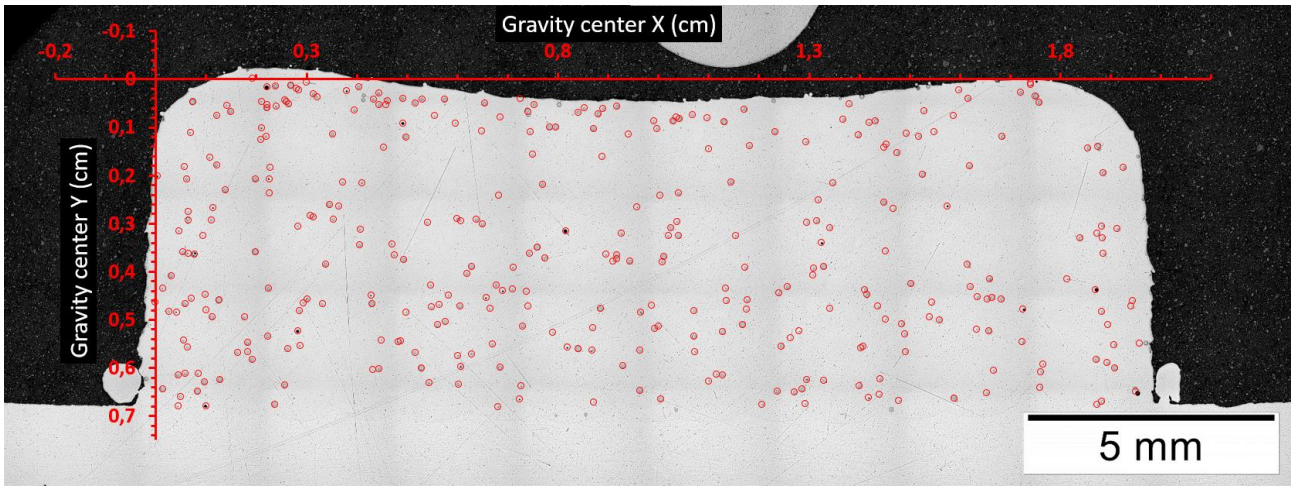


Figure 4-4: Overview and particles map for sample W27.

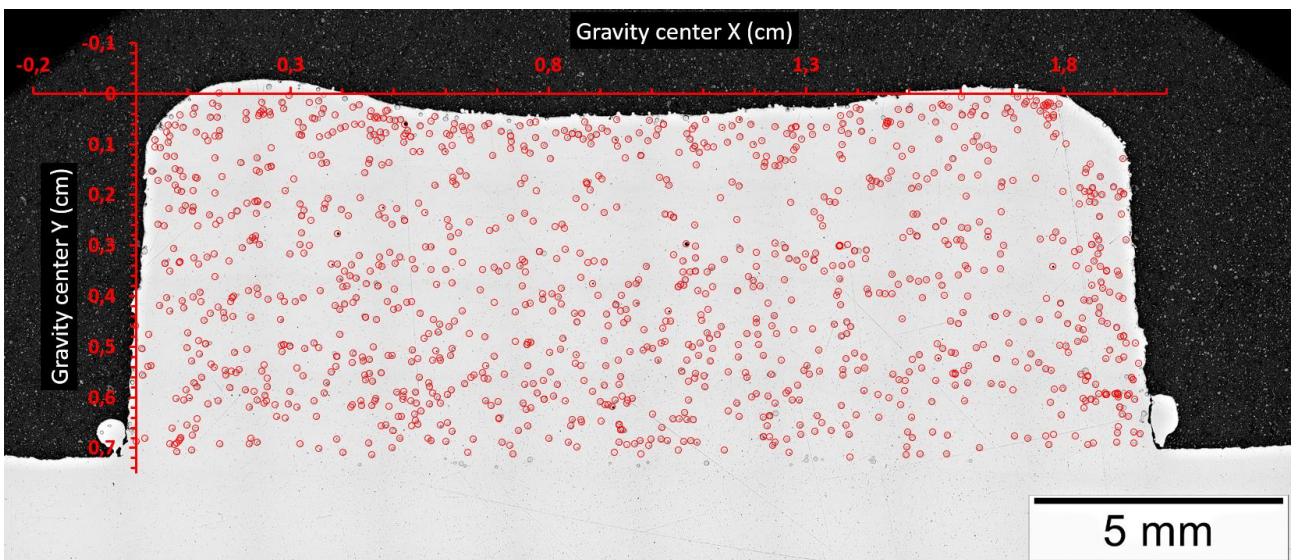


Figure 4-5: Overview and particles map for sample W43.

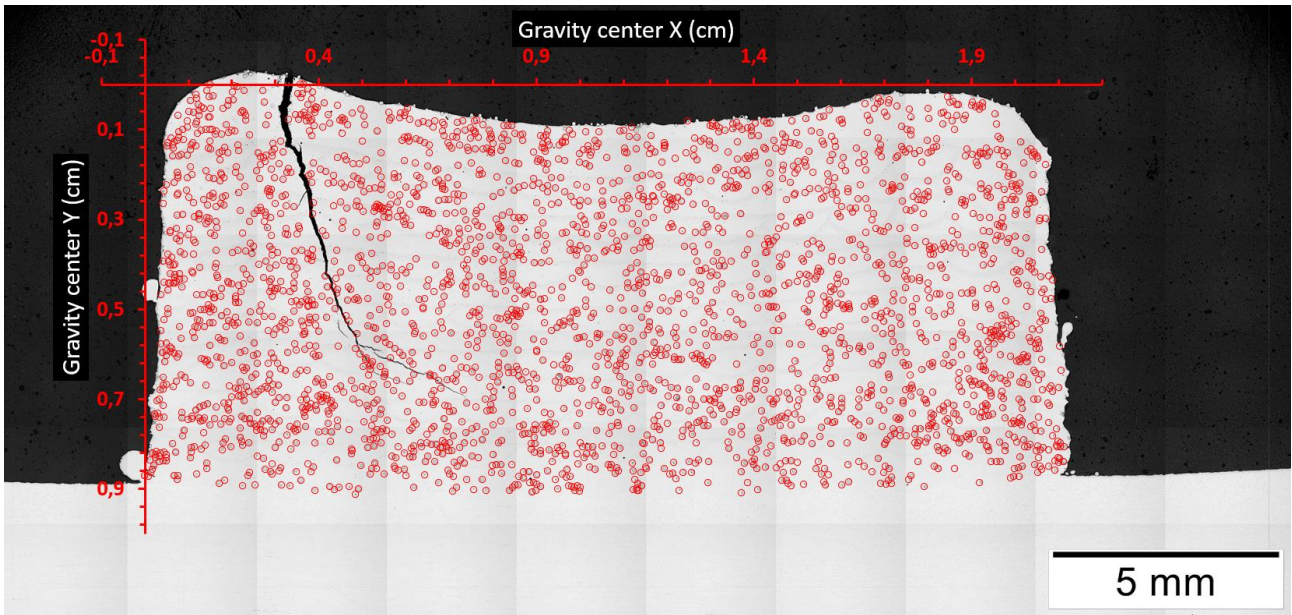


Figure 4-6: Overview and particles map for sample W53.

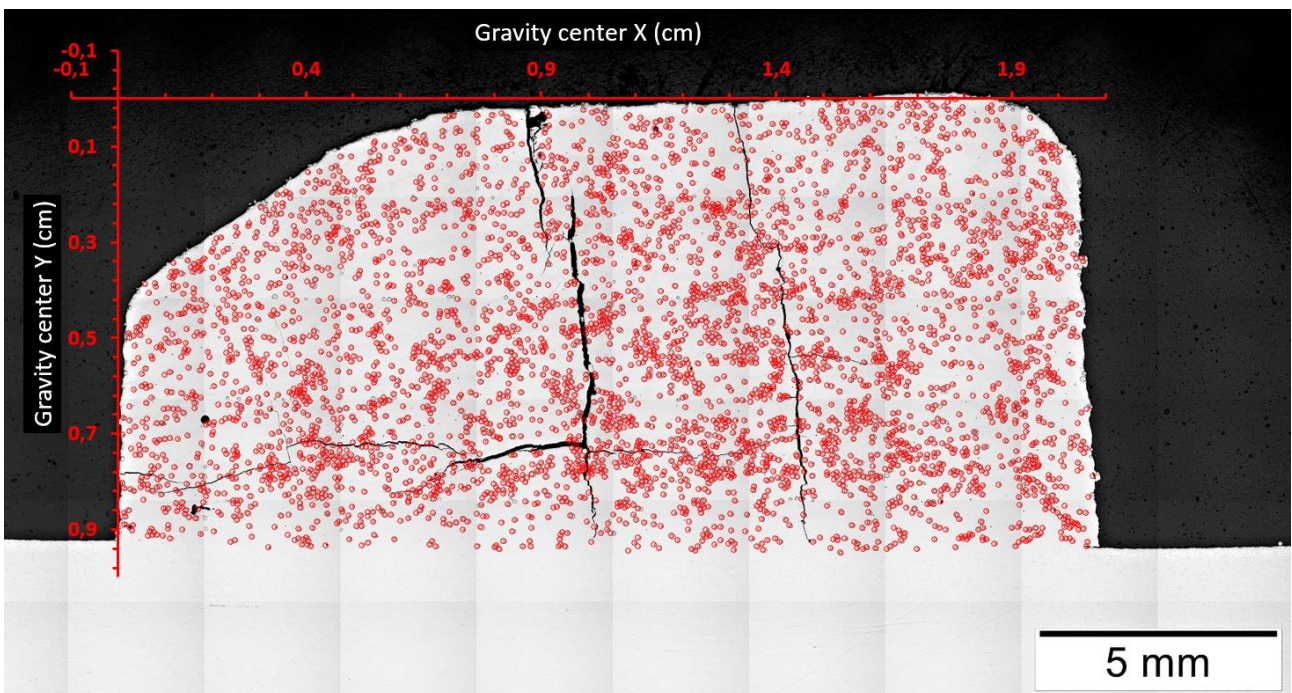


Figure 4-7: Overview and particles map for sample W62.

- The quantification of the particles for 100 μm thick box, along y direction, was the most useful analysis. The purpose was to understand (1) whether there is a pattern of distribution between all four samples, and (2) whether the particles sediment at the bottom of the melt pool which

is 700 μm height. Figures 4-8 to 4-11 shows the information that have been obtained from the analysis of the overviews.

In each sample (1), the particles show the same distribution as a function of the distance from the substrate. At the base of the sample (y maximum) there are little particles. In the mid-lower part there are more particles, as if there would be an accumulation of particles. Then, in the mid-higher part there is a lack of particles. In the top of the sample the number of particles increase again (y minimum). This effect is more visible in the W27 and W43 samples [Figure 4-8, 4-9]. In samples W53 and W62 [Figure 4-10, 4-11], the variation is still present, but less prominent. In the top zone of sample W62 [Figure 4-11] there is not the increase of the number of the particles described for the other samples because of its irregular shape. Particles (2) tend to accumulate between each cladded layer (700 μm). Sample W27 [Figure 4-8] shows a pattern. The accumulation of particles is present every three to five layers considered in this analysis (100 μm). Hence, every 300 μm to 500 μm more particles are measured. By contrast, samples W43, W53 and W62 [Figure 4-9 to 4-11] show an accumulation of particles every 5 to 9 layers. This agrees with the height of the cladded layer (700 μm).

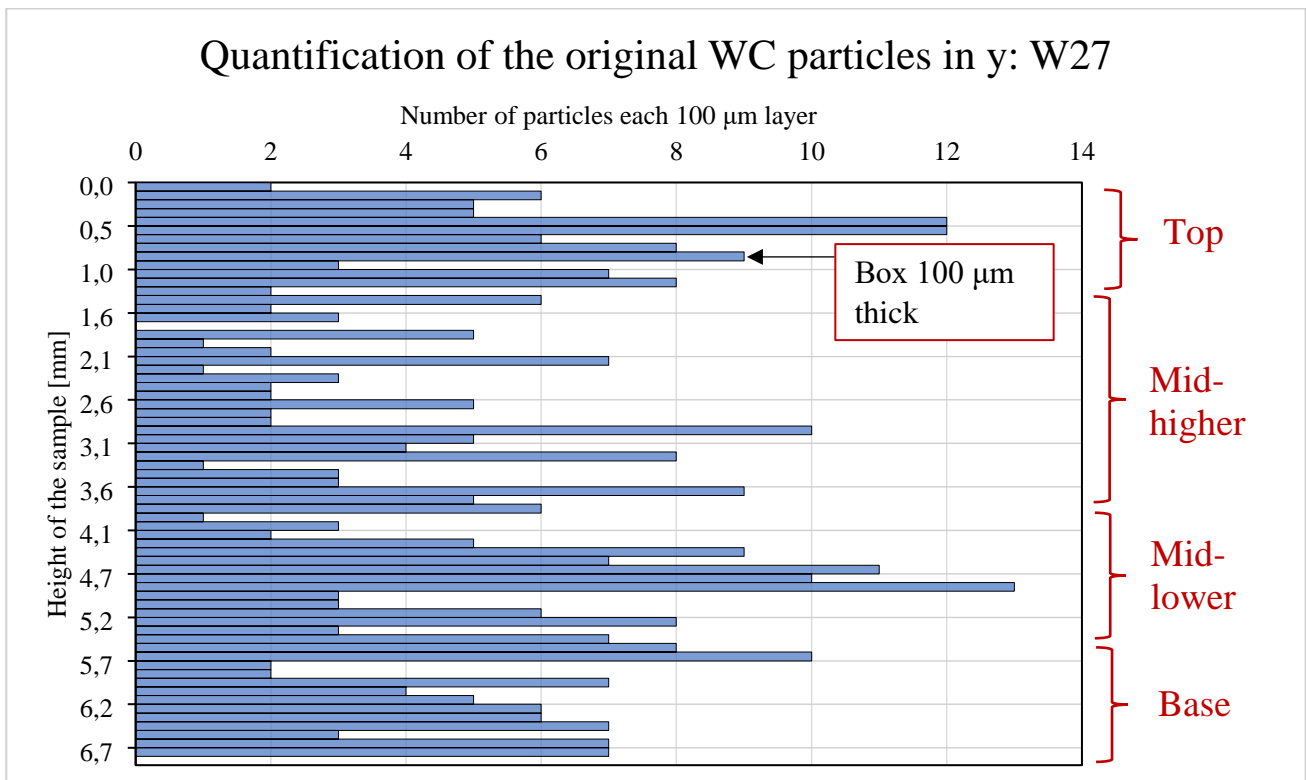


Figure 4-8: Number of particles every 100 μm layer, y direction. Sample W27.

Quantification of the original WC particles in y: W43

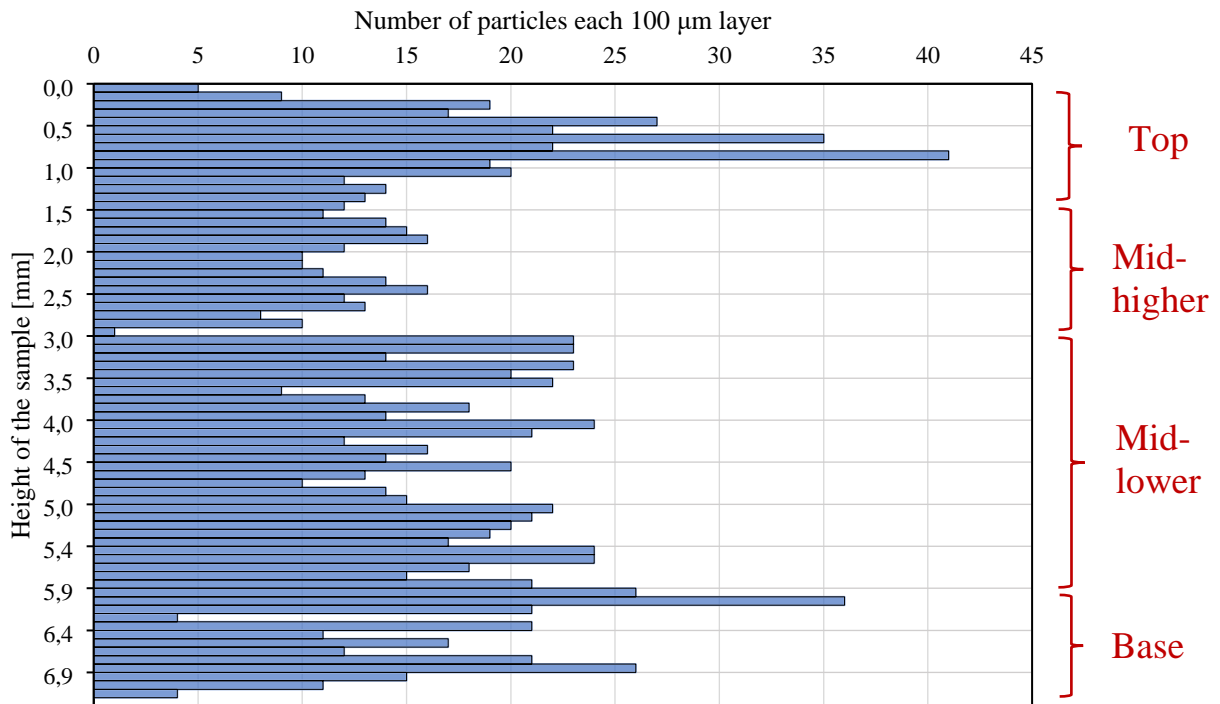


Figure 4-9: Number of particles every 100 μm layer, y direction. Sample W43.

Quantification of the original WC particles in y: W53

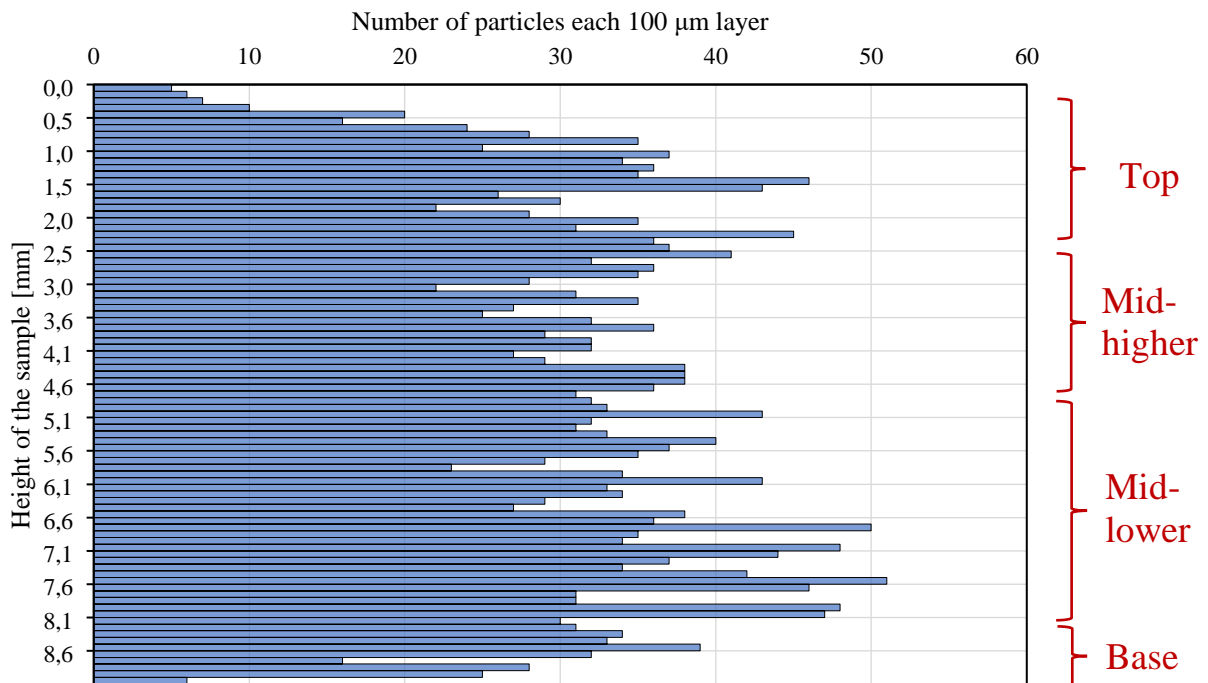


Figure 4-10: Number of particles every 100 μm layer, y direction. Sample W53.

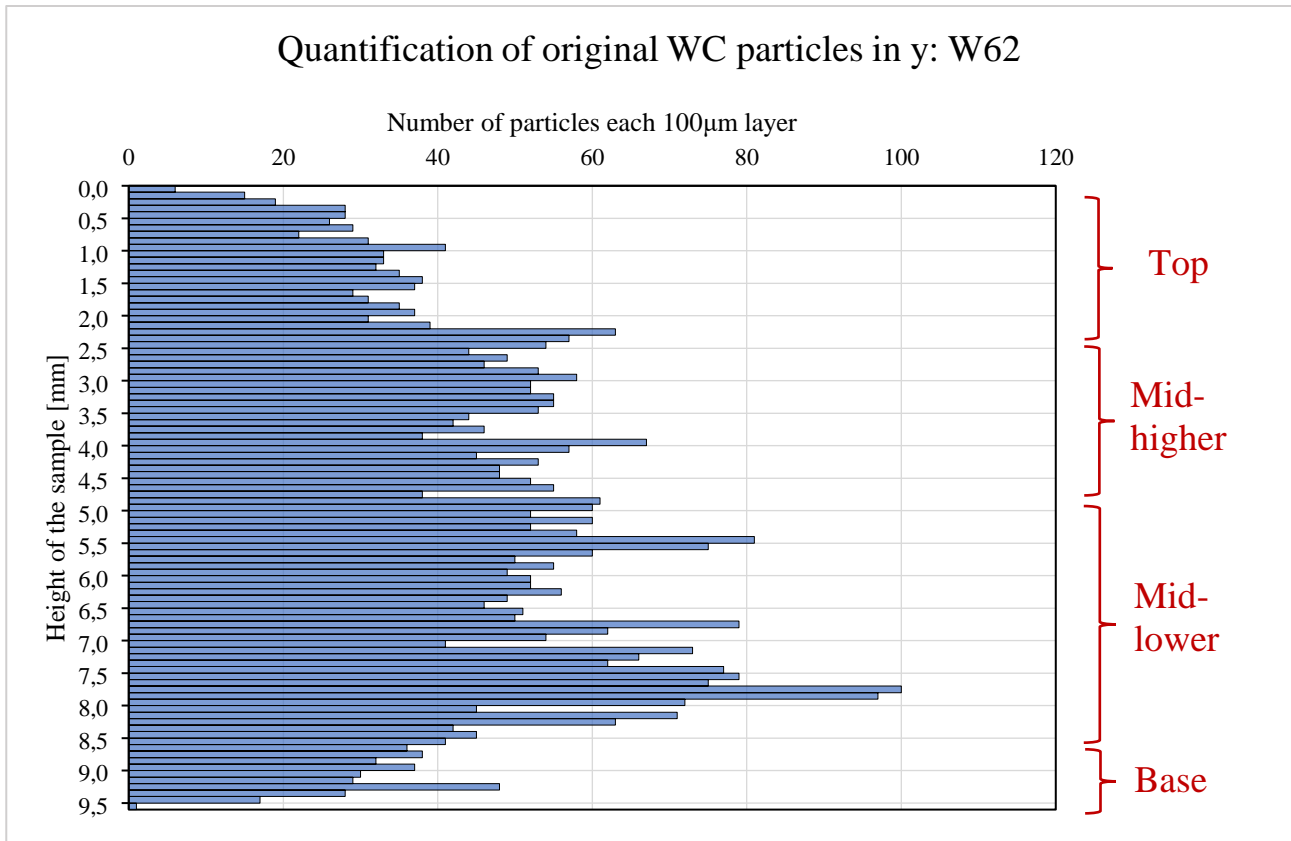


Figure 4-11: Number of particles every 100 µm layer, y direction. Sample W62.

- The same type of measurement has also been carried out in x direction. So, the quantity of particles has been measured, again, for steps of 100 µm thick. For all four samples [Figure 4-12 to 4-15] particles have a tendency to accumulate on the edge of the sample. In sample W27 [Figure 4-12] the trend is very marked. In sample W43 [Figure 4-13], at 1,4 cm width from the left edge, there is a point with more particles due to a random accumulation. Sample W53 [Figure 4-14] follows slightly the trend described as common for all the four sample. Finally, sample W62 [Figure 4-15] only the right part (for high values of x) is to be considered, because its width and its height are not constant. The trend is the same with high values of x .

Quantification of the original WC particles in x: W27

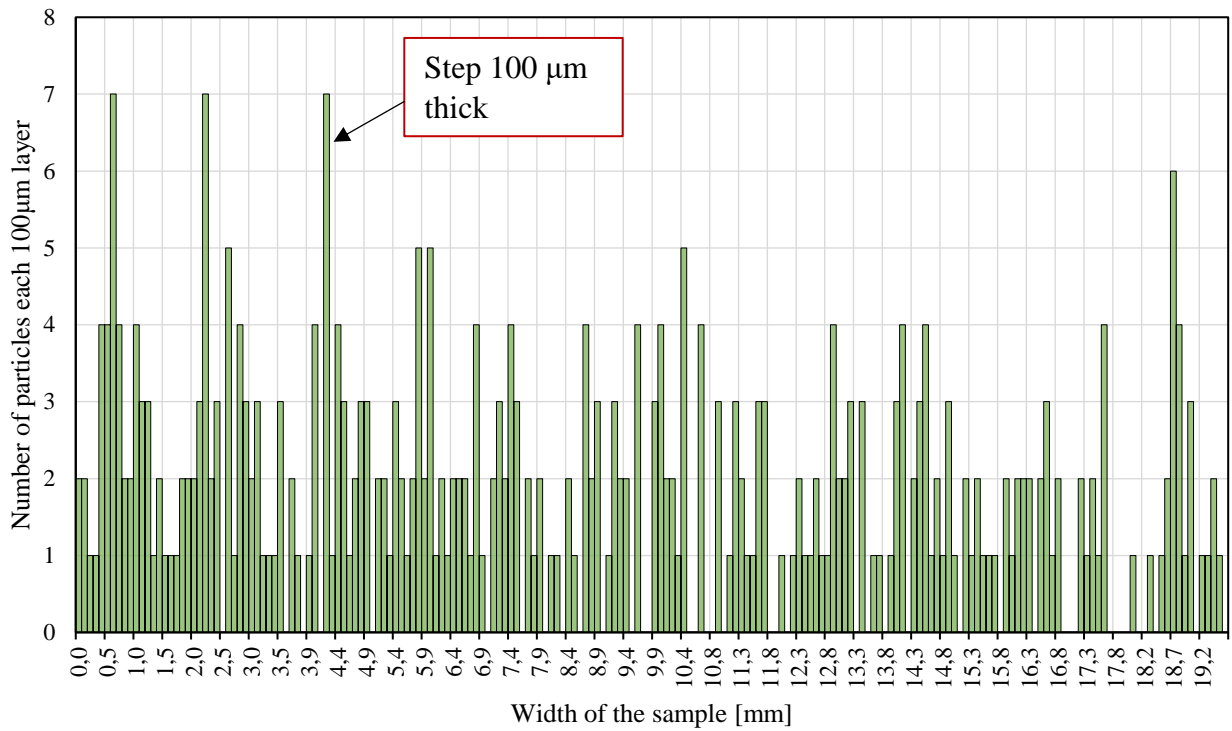


Figure 4-12: Number of particles every 100 μm layer, x direction. Sample W27.

Quantification of original WC particles in x: W43

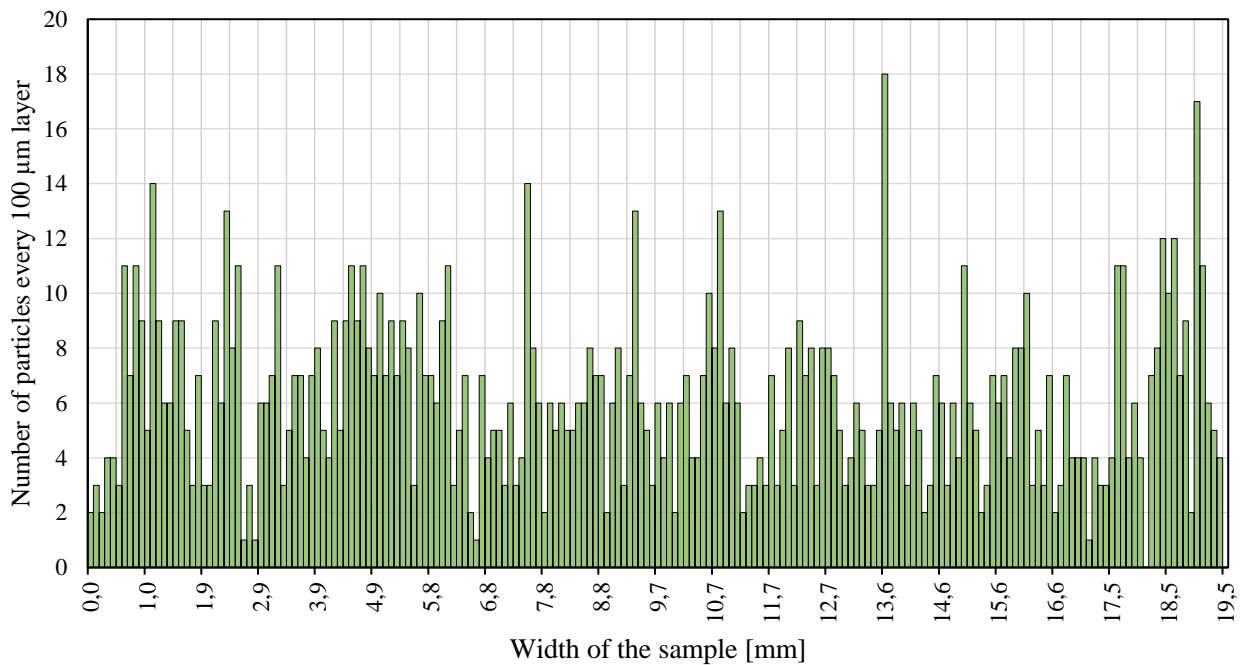


Figure 4-13: Number of particles every 100 μm layer, x direction. Sample W43.

Quantification of original WC particles in x: W53

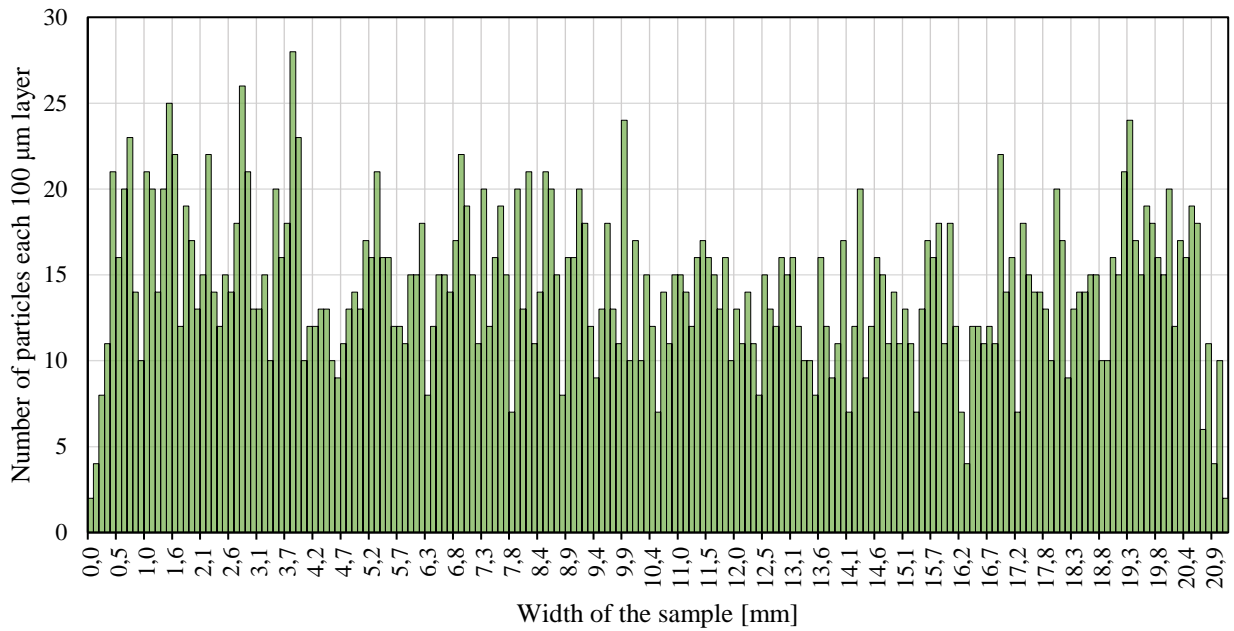


Figure 4-14: Number of particles every 100 μm layer, x direction. Sample W53.

Quantification of original WC particles in x: W62

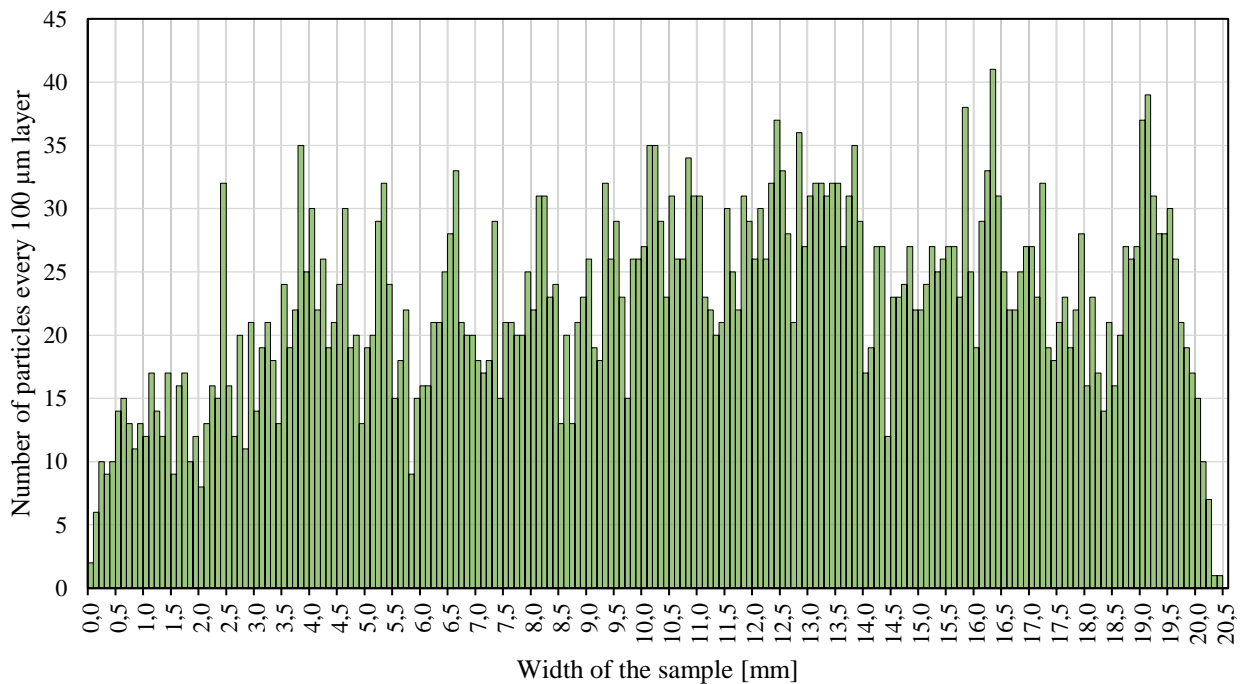


Figure 4-15: Number of particles every 100 μm layer, x direction. Sample W62.

- The total surface of the particles has been analyzed in every single box 100 μm thick along y direction. The surfaces of all individual particles have been summed in every 100 μm thick box in y. From Figure 4-16 to 4-19 are presented the data for each sample. The pattern shows a decreasing of particles surface fraction in the center of the sample.

Finally, has been quantified the fraction of the particles surface for each sample:

$$f_s = \frac{\sum_1^i S_i}{S_{TOT}} \quad (4)$$

with s_i surface of every single particle and S_{TOT} surface of the overall sample. These data [Table 4-3] have been gained with Stream Motion Software.

Table 4-3: Fraction of particles surface for each sample.

Sample	W27	W43	W53	W62
f_s	0,00925	0,02813	0,05654	0,26241

The ratio is in accordance with the percentage of the reinforcing phase.

Particles surface every 100 μm layer along y axis: W27

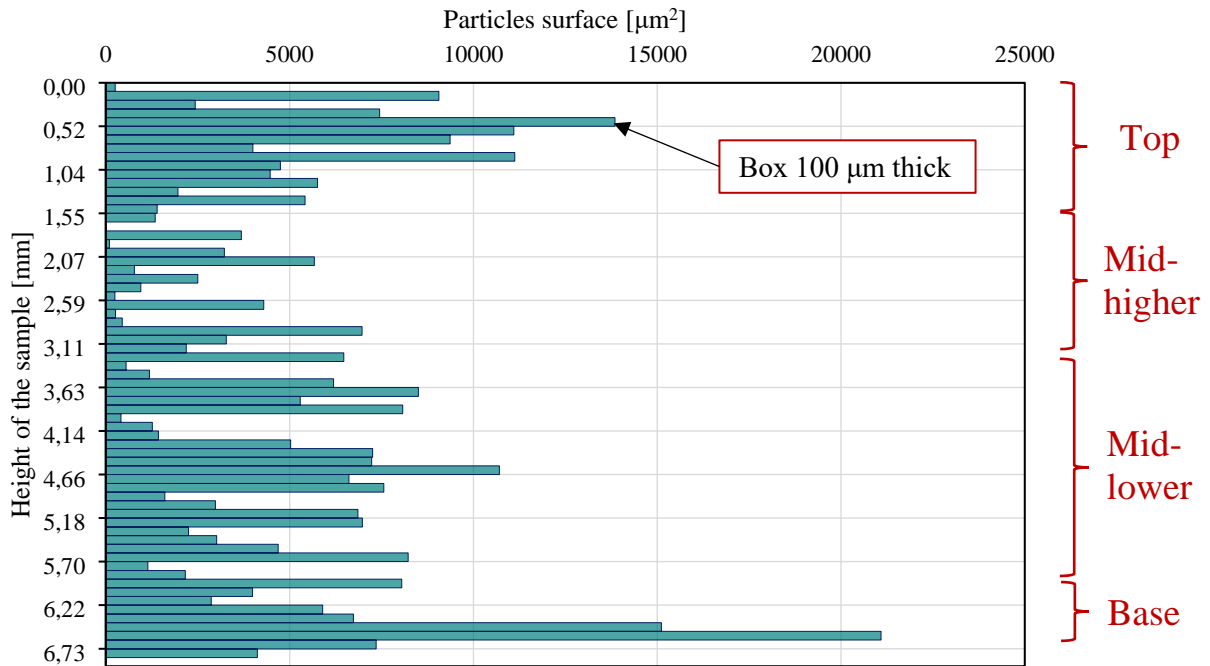


Figure 4-16: Particles surface every 100 μm layer along y axis. Sample W27.

Particles surface for every 100 μm layer along y axis: W43

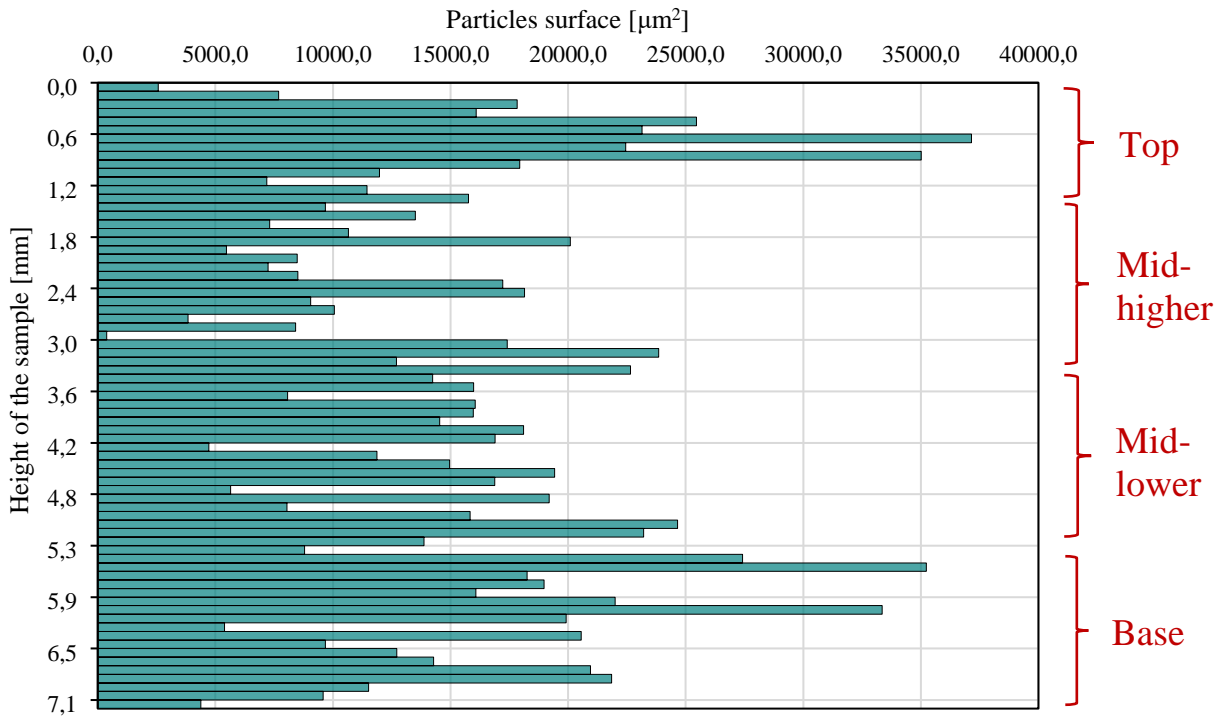


Figure 4-17: Particles surface every 100 μm layer along y axis. Sample W43.

Particles surface for every 100 μm layer along y axis: W53

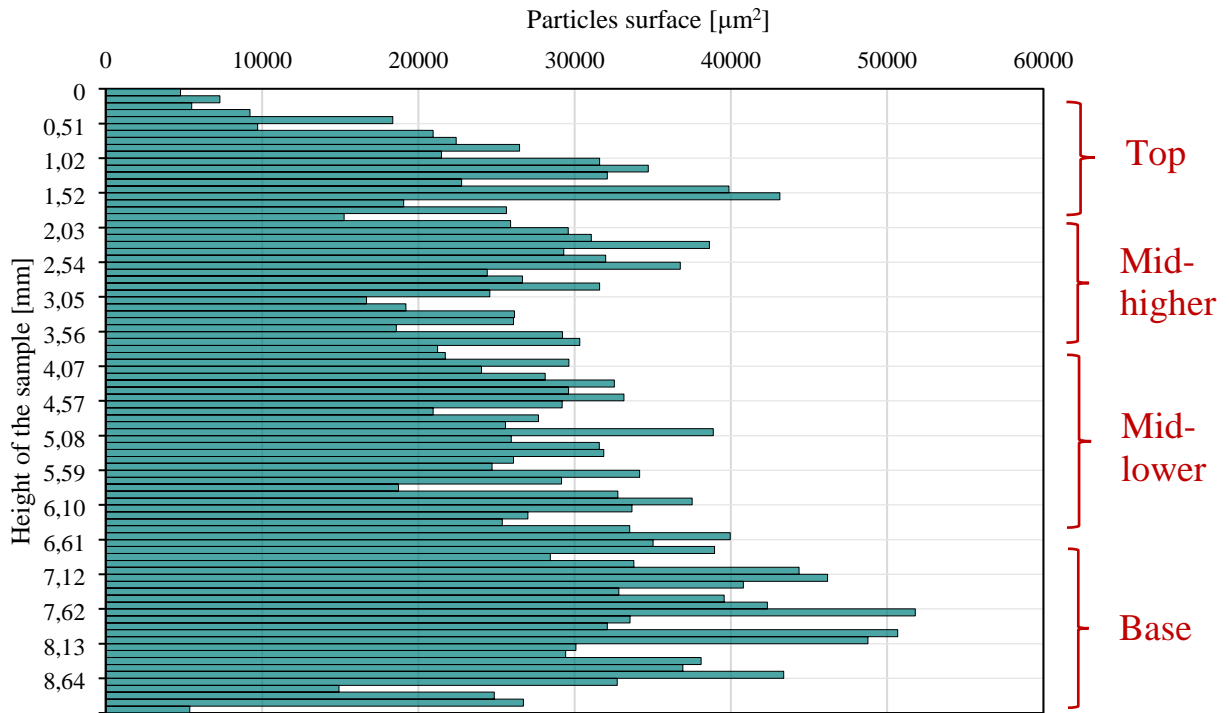


Figure 4-18: Particles surface every 100 μm layer along y axis. Sample W53.

Particles surface for every 100 μm layer along y axis: W62

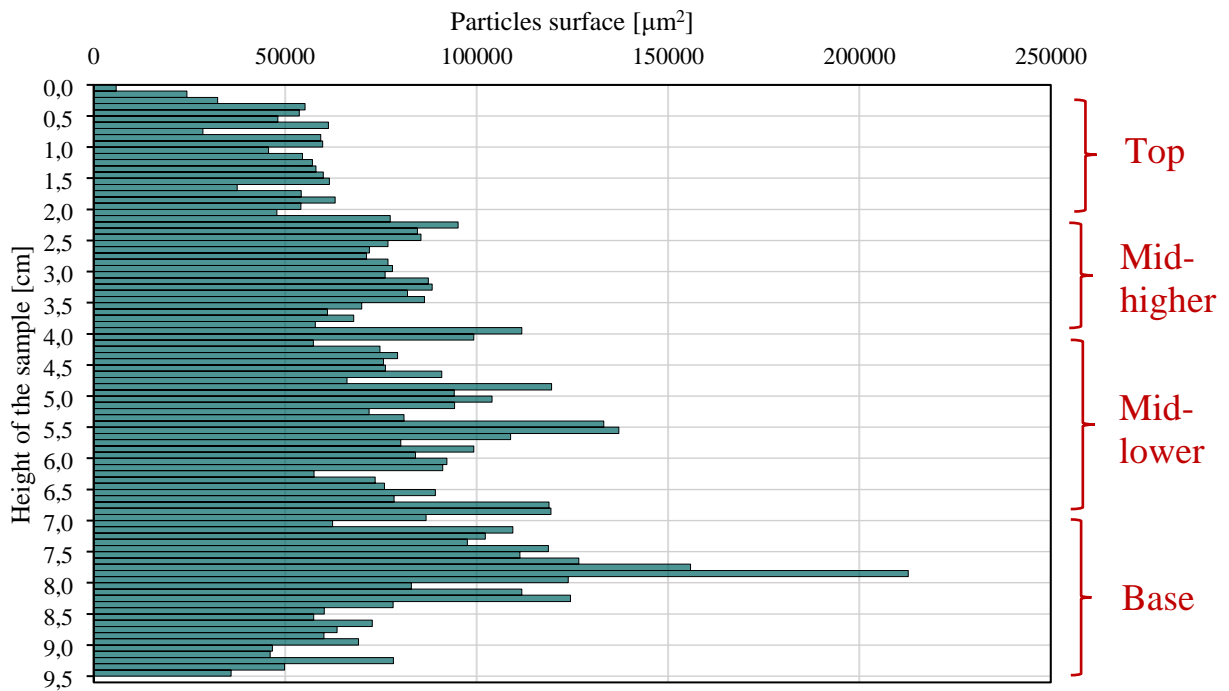


Figure 4-19: Particles surface every 100 μm layer along y axis. Sample W62.

4.2.1.2 Dendrites growth direction

Sample W43 has been observed by optical microscopy to get information about the orientation of the dendrites in the matrix. Figure 4-20 shows the orientation of the dendrites. Through the cross-section of the sample different zones of the matrix correspond to different orientations of the dendrites. This is important, because it gives indications on the direction of solidification in a precise zone of the matrix.

Moreover, investigations have been performed with the SEM on the same sample. Thanks to the higher magnification and the greater contrast between the matrix and the carbide, the directions of the dendrites has been determined more clearly. Figure 4-21 shows that dendrites near each other grow in the same direction, thus forming a bundle of dendrites with similar orientation. Furthermore, the growth direction of dendrites is perpendicular to the surface of the particles, always forming bundles.

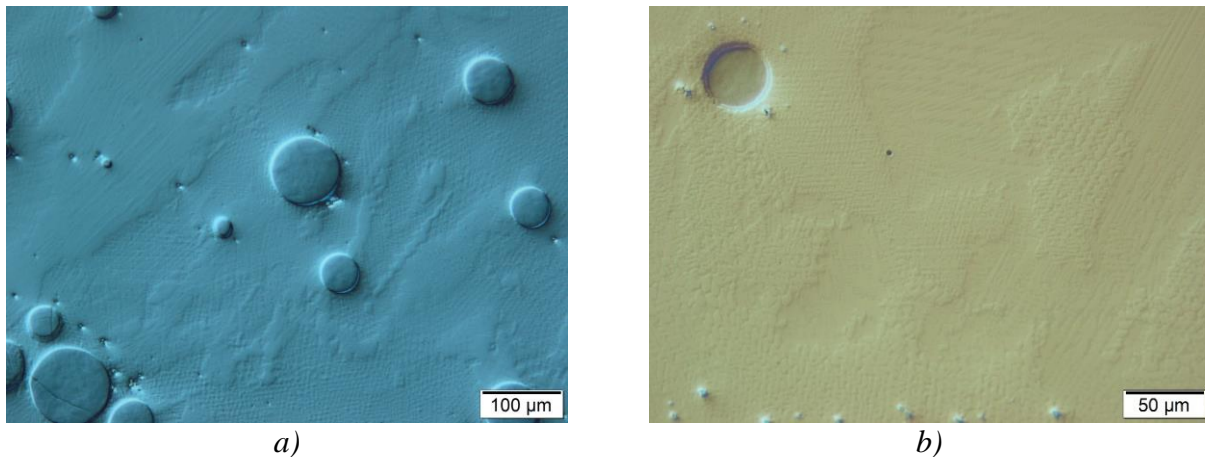


Figure 4-20: Investigations on dendrites growth direction with optical microscope. a) 100x magnification. b) 200x magnification.

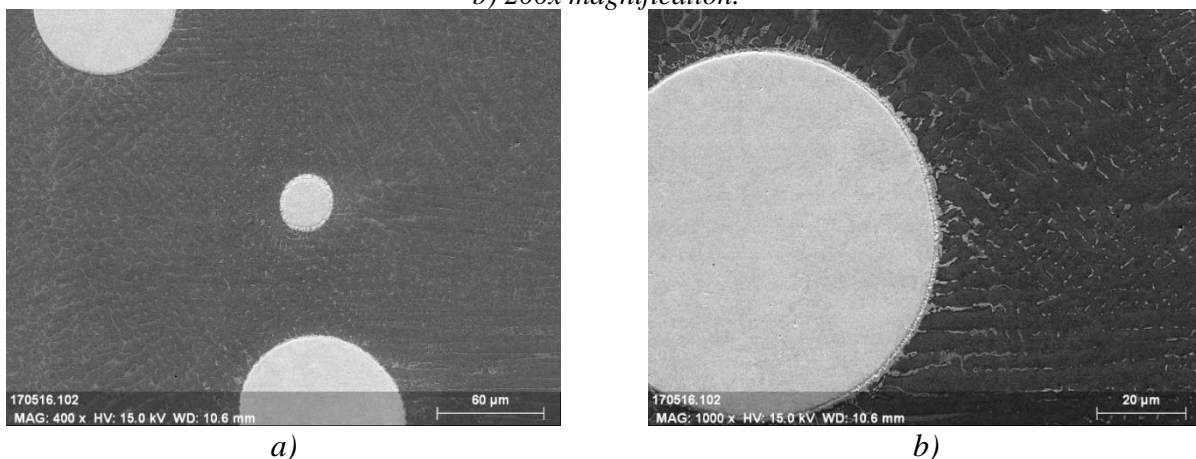


Figure 4-21: Investigations on dendrites growth direction with SEM. a) 400x magnification. b) 1000x magnification.

4.2.1.3 Carbides characterization

Sample W43 has been observed with optical microscope to gain information on the shape of the carbides. This sample was chosen because it is the one with the higher percentage of particles but without cracks. Nevertheless, all the samples show the same compounds around the particles. The reaction carbides formed around the particles and the carbides between the dendrites were investigated [Figure 4-22]. The size of the carbides is very small, due to the very fast cooling of the cladding process. So, an investigation with the SEM was necessary. Figure 4-23 show SEM images at low magnification of the surface of the sample, meanwhile Figure 4-24 shows higher magnifications. Figure 4-25 shows the formation of various regions: particle and carbides circular crown (A), equiaxial zone (B), eutectic carbides zone (C), dendritic zone (D). The order of these zone has been chosen in function of the distance from the particles.

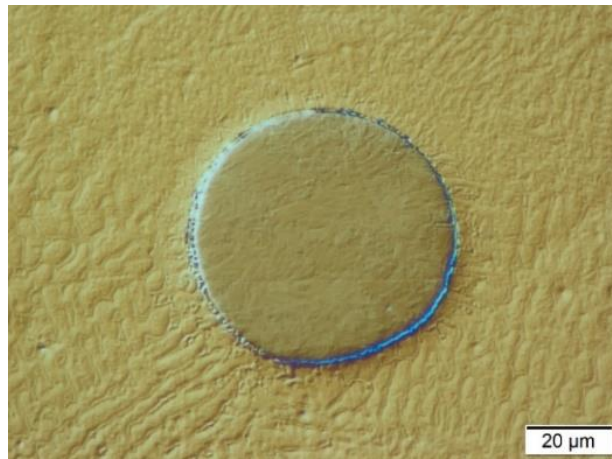


Figure 4-22: Optical image of the carbides formed around the particles. 500x of magnification.

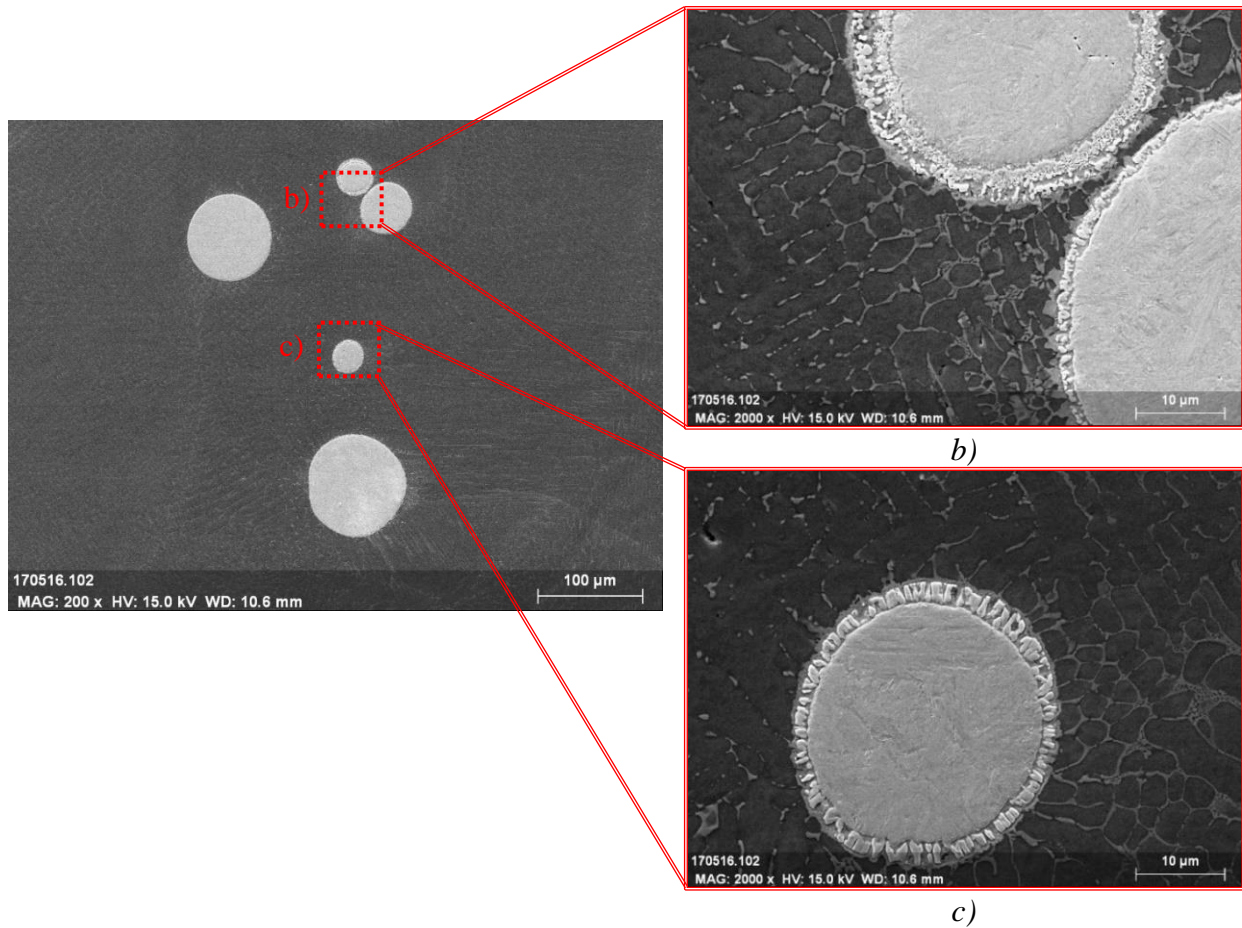


Figure 4-23: SEM images at low magnifications of the carbides around the particles. a) Overview at 200x of magnification. b) Detail at 2000x of the two near particles on the top. c) Detail at 2000x of the smaller particle in the middle.

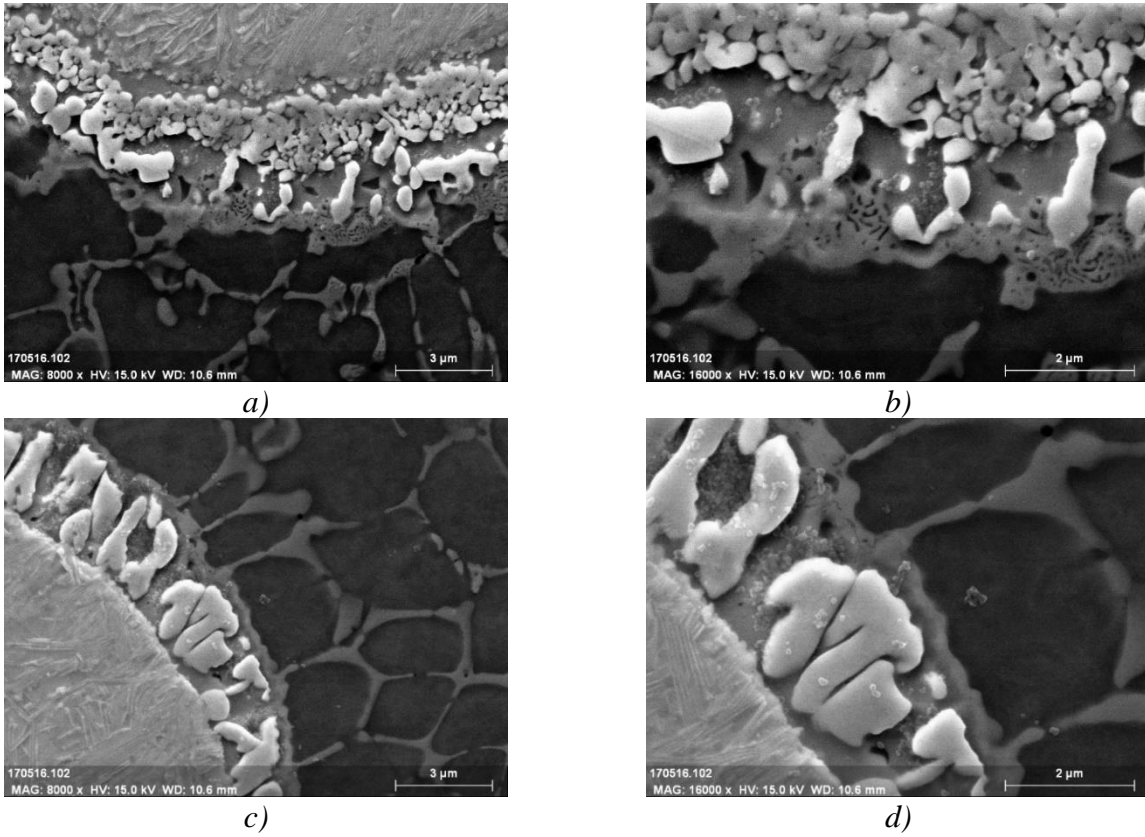


Figure 4-24: SEM images at high magnifications of the carbides around the particles. a) and b) pictures are higher magnifications of the Figure 4-23b. c) and d) pictures are higher magnification of Figure 4-23c. a) and c) show a magnification of 8000x, b) and d) show a magnification of 16000x.

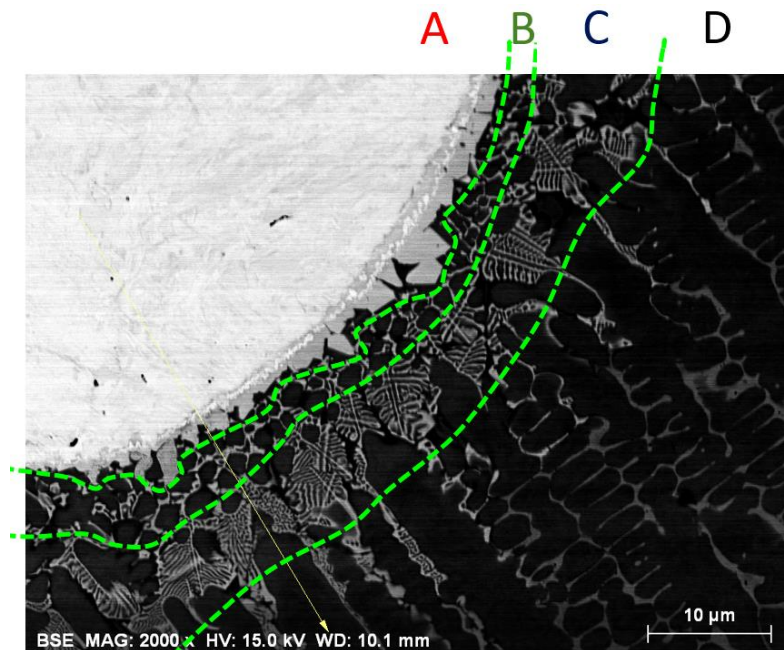


Figure 4-25: Different zones considered around the particle to study the formation of the different carbides.

Zone A . Particle and carbides circular crown

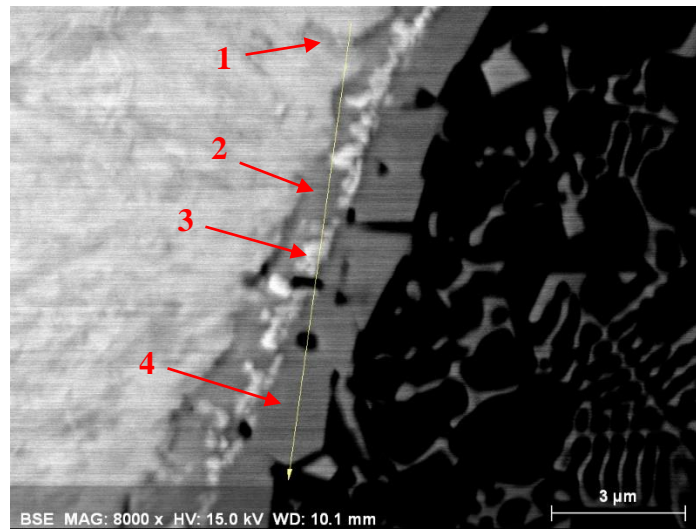


Figure 4-26: Zone A: subdivision to study the compositions.

Zone A presents the compounds closest to the particle. It can be divided into four sub-zones to achieve a better understanding of the elements diffusion through close compounds [Figure 4-26]. Different zones have been investigated. Firstly, inside the particle (1), to verify the composition data provided by Carpenter and the composition from the EDS analysis on particles. Secondly, the zone between the particle and the white carbides (2). Thirdly, the white carbides (3). Finally, the compounds formed between the white carbides and the matrix (4). The numbers in brackets correspond both to the numbers in Table 4-4, 4-5 and to the numbers in Figure 4-26.

With the SEM in EDS mode, many profile analyses have been performed. The compositions in weight percent of the various zones are presented in Table 4-4. The compositions in atomic percent are presented in Table 4-5, thus allowing to understand the type of carbide present in each compound. The carbide inside the particle (1) has 50 at% of C and almost 50 at% of W. Hence, it is a type W-rich MC carbide. All three carbides investigated are a Cr and W-rich M_2C carbide. The white carbides (3) present less Cr and more W, in comparison with the others. In fact, the Back-Scattered Electron (BSE) image shows a lighter color.

Table 4-4: Compositions in wt% and relative deviation standard values. Zone A.

A	wt%	C	Cr	Fe	W	Ni	Mo	Si	Mn
1	Inside the original WC particle	6,7±1,0	0,2±0,3	0,5±0,5	92,2±1,1	0,2±0,3	0	0	0,2±0,2
2	between original WC particle and white carbides	4,9±0,6	5,3±0,5	18,3±1,2	69,7±1,2	1,5±0,6	0	0	0,3±0,4
3	white carbides	4,7±0,5	2,4±0,6	7,0±1,0	85,3±1,8	0,3±0,4	0±0,1	0	0,1±0,1
4	compounds between white carbides and matrix	5,3±0,9	7,1±1	20,6±1,6	63,8±2,6	2,1±0,7	0,7±0,6	0	0,4±0,4

Table 4-5: Compositions in at% and relative deviation standard values. Zone A.

A	at%	C	Cr	Fe	W	Ni	Mo	Si	Mn
1	Inside the original WC particle	51,4±4,3	0,4±0,5	0,9±0,8	46,7±3,8	0,3±0,6	0	0	0,3±0,4
2	between original WC particle and white carbides	32,6±2,8	8,1±0,8	26,3±1,6	30,5±1,8	2,0±0,8	0,0±0,1	0	0,4±0,6
3	white carbides	36,9±3,4	5,4±1,7	14,5±4,0	42,0±5,1	1±1	0,0±0,1	0	0,2±0,3
4	compounds between white carbides and matrix	32,5±3,7	10,2±1,2	27,5±2,1	26,0±2,3	2,7±0,9	0,6±0,5	0	0,5±0,5

Zone B . Equiaxial zone

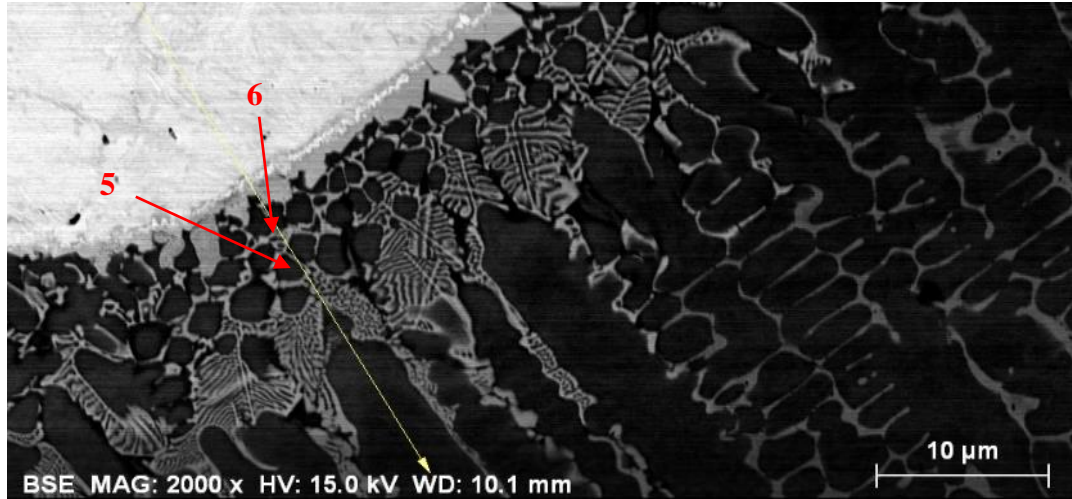


Figure 4-27: Zone B: subdivision to study the compositions.

Moving away from the particle, the microstructure becomes equiaxial. Zone B has been divided in two sub-zones [Figure 4-27]. The first zone (5) is the austenite phase. The second zone (6) is grain boundary, that limits regular zones of austenite phase.

In Table 4-6 and Table 4-7 are reported the compositions of the two subzones indicated in Figure 4-27. The grain boundary, being in the vicinity of the austenite, contains a lot of Iron. It can be considered a type M_2C carbide of mainly Cr and Fe with a little percentage of W.

Table 4-6: Compositions in wt% and relative deviation standard values. Zone B.

B	%wt	C	Cr	Fe	W	Ni	Mo	Si	Mn
5	austenite phase	2,9±0,5	13,3±0,3	56,6±1,1	17,5±3,2	7,9±1,6	1,1±0,4	0	0,8±0,4
6	grain boundary	5,3±0,3	13,8±0,3	33,8±0,1	40,3±0,4	4,0±0,1	2,4±0,8	0	0,4±0,3

Table 4-7: Compositions in at% and relative deviation standard values. Zone B.

B	%at	C	Cr	Fe	W	Ni	Mo	Si	Mn
5	austenite phase	13,6±1,8	14,5±0,6	57,4±1,3	5,4±1,2	7,6±1,4	0,6±0,2	0	0,8±0,4
6	grain boundary	26,9±1,3	16,3±0,1	37,2±0,4	13,5±0,1	4,2±0	1,5±0,5	0	0,5±0,4

Zone C . Reaction eutectic carbides zone

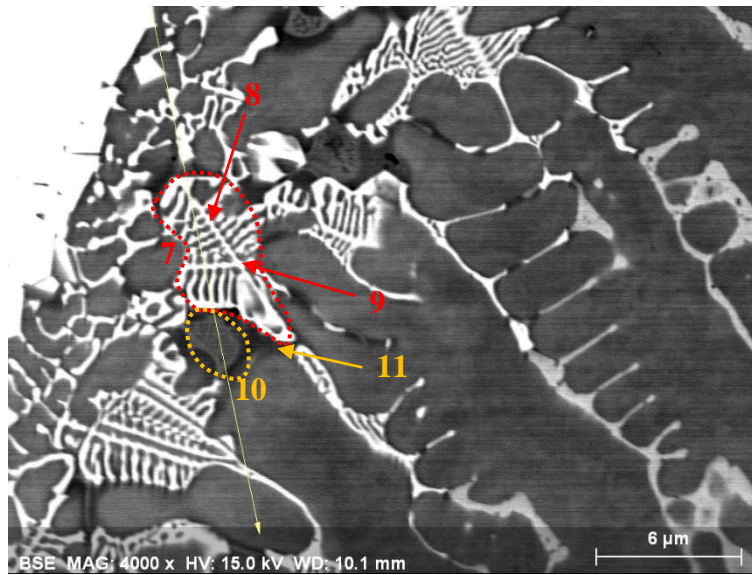


Figure 4-28: Zone C: subdivision to study the compositions.

This part of the microstructure has not been observed around all the particles, and can be present only in one side of the particle. Two carbides have been observed. The first, lighter one, is a lamellar carbide enriched with tungsten. This carbide presents a main lamella to which other lamellae are anchored, in this work called support. The composition of this carbide has been measured as an average between lamellae (7). Then the composition has been investigated in the central part of support (8), and, finally, at the junction of the two supports (9). The second carbide, the darker one that forms around the tungsten lamellar carbide, is a chromium lamellar carbide (10). The dark zone around this last carbide has also been analyzed (11).

Table 4-8 and 4-9 show the compositions of these compounds. The morphology of the tungsten lamellar carbide show that it is an M_6C eutectic type [34]. The average composition (7) confirms it. The chromium carbide is also eutectic. The fine lamellar structure corresponds to an M_7C_3 of Fe and Cr (10) [36].

Table 4-8: Compositions in wt% and relative deviation standard values. Zone C.

C	%wt	C	Cr	Fe	W	Ni	Mo	Si	Mn
7	tungsten lamellar carbide	4,0±0,8	12,3±1,1	45,6±4,5	30,1±5	5,8±1,1	1,4±0,6	0	0,8±0,4
8	part of the W-C carbide of support	4,5±1,0	11,6±1,2	39,4±3,1	37,6±4,1	4,5±0,8	1,7±0,5	0	0,6±0,3
9	X center of the two supports	5,5±0,2	11,6±0,8	34,9±3,1	41,3±2,9	4,0±0,6	2,4±0,2	0	0,3±0
10	chromium carbide	5,5±0,5	30,7±2,0	44,5±2,0	12,4±2,5	3,4±0,6	2,0±0,4	0	1,4±0,6
11	darker zone near Cr carbide	4,4±1,6	17,7±2,9	62,0±2,0	8,3±1,9	6,3±1,3	0,7±0,3	0	0,5±0,3

Table 4-9: Compositions in at% and relative deviation standard values. Zone C.

C	%at	C	Cr	Fe	W	Ni	Mo	Si	Mn
7	tungsten lamellar carbide	20,0±4,0	14,0±1,1	48,6±4,4	9,8±1,8	5,9±1,1	0,9±0,4	0	0,8±0,5
8	part of the W-C carbide of support	23,2±3,8	13,8±1,3	43,6±2,9	12,7±1,9	4,8±0,9	1,1±0,3	0	0,7±0,4
9	X center of the two supports	28,1±1,6	13,7±0,7	38,4±2,8	13,8±1,1	4,2±0,7	1,5±0,1	0	0,4±0,0
10	chromium carbide	22,5±1,8	29,3±1,5	39,5±1,9	3,4±0,8	2,9±0,5	1,0±0,2	0	1,3±0,6
11	darker zone near Cr carbide	14,8±5,1	16,8±1,6	59,6±5,2	2,3±0,6	5,6±1,3	0,4±0,1	0	0,5±0,2

Zone D . Dendritic Zone

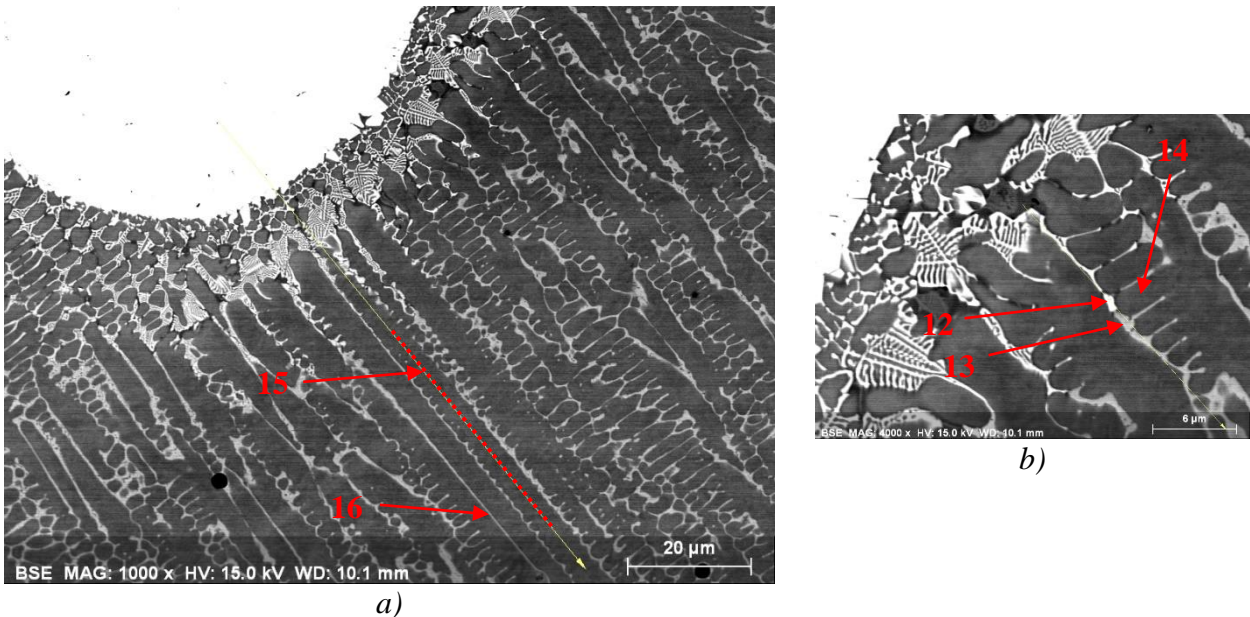


Figure 4-29: Zone D: subdivision to study the compositions. a) compounds further away from the particle. b) compounds near the particle.

The dendritic zone has been studied only near the particles, to focus on the diffusion zone. The microstructure of this zone can be explained considering two sub-zones: the austenite phase inside the dendrites and the carbides around the dendrites. The austenite phase was studied at two distinct locations: first near the particle, between the carbides (14) and far from the particle, along the dendrite (15). Secondly, the carbides in between the dendrites have been studied: (12), (13) and (16).

Table 4-10 and Table 4-11 show the compositions of the different zones and their positions in Figure 4-29. Mainly two types of carbides form between the dendrites: one richer in W and the other richer in Cr. These two types can be represented by the M_4C type of carbide rich with W, Cr and Fe or by the $M_{23}C_6$ type of carbide rich with W, Cr and Fe.

Table 4-10: Compositions in wt% and relative deviation standard values. Zone D.

D	%wt	C	Cr	Fe	W	Ni	Mo	Si	Mn
12	carbide between the dendrites (light)	4,9±0,9	14,1±0,9	30,9±2,0	41,7±2,4	3,1±0,8	4,8±1,5	0	0,5±0,5
13	carbide between the dendrites (dark)	5,2±0,7	18,5±0,8	44,6±2,7	23,9±4,0	4,5±1,3	2,6±0,3	0	0,7±0,5
14	austenite phase between the carbides	2,5±0,7	12,8±1,0	63,8±2,6	9,9±3,5	9,1±1,0	0,9±0,4	0,1±0,2	0,9±0,5
15	austenite phase far from the original WC particle (in the dendrite)	3,5±0,6	13,1±1,0	63,9±2,3	8,2±2,8	9,0±1,0	1,0±0,5	0,1±0,1	1,2±0,5
16	carbides between dendrites 50 µm away from the particle	3,9±0,5	19,0±0,9	46,9±1,8	21,1±2,3	5,1±0,9	3,0±0,42	0	1,0±0,2

Table 4-11: Compositions in at% and relative deviation standard values. Zone D.

D	%at	C	Cr	Fe	W	Ni	Mo	Si	Mn
12	carbide between the dendrites (light)	25,8±3,7	17,2±1,2	35,3±2,5	14,5±1,1	3,4±0,9	3,2±1,1	0	0,6±0,6
13	carbide between the dendrites (dark)	23,5±2,6	19,4±1,1	43,5±2,0	7,1±1,4	4,2±1,1	1,5±0,2	0	0,7±0,5
14	austenite phase between the carbides	11,2±3,0	13,4±1,0	62,3±2,3	3,0±1,1	8,5±1,0	0,5±0,2	0,2±0,4	0,9±0,5
15	austenite phase far from the original WC particle (in the dendrite)	15,0±2,4	13,1±1,0	59,6±2,0	2,4±0,8	8,0±0,9	0,6±0,2	0,2±0,3	1,1±0,4
16	carbides between dendrites 50 µm away from the particle	18,1±2,1	20,6±0,7	47,2±2,0	6,5±0,7	4,9±0,9	1,8±0,2	0	1,0±0,2

EBSD Analyses

EBSD Analyses were performed on the W43 sample. The first analysis was done in a zone between two particles that are close to each other. Figure 4-30a shows the chosen zone for the analysis, meanwhile Figure 4-30b shows the pattern quality of the zone considered. The pattern quality specifies the indexed zone of the analysis: the white zones are indexed. Comparison of Figure 4-30a and b shows a slight shift of the observed area during the measurement, but this does not affect the validity of the observation.

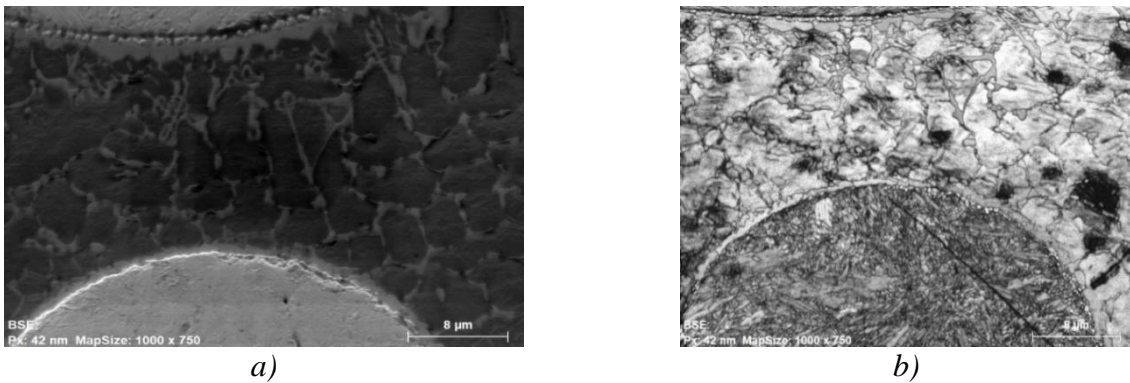


Figure 4-30: First EBSD. a) BSE picture of the analysis zone. b) Pattern quality of the analysis.

Figure 4-31 reports the complete result of the EBSD analysis. Each color corresponds to a lattice type, not necessarily to the phase indicated. However, the indicated phases are the most likely. Table 4-12 helps to correlate the colors with the phases examined. The detected forms of tungsten carbide are: W_2C_T1 (trigonal) + Qusongite (see section 2.3.2).

Figure 4-32 shows the different crystallographic orientations corresponding to the different directions of solidification, using different colors.

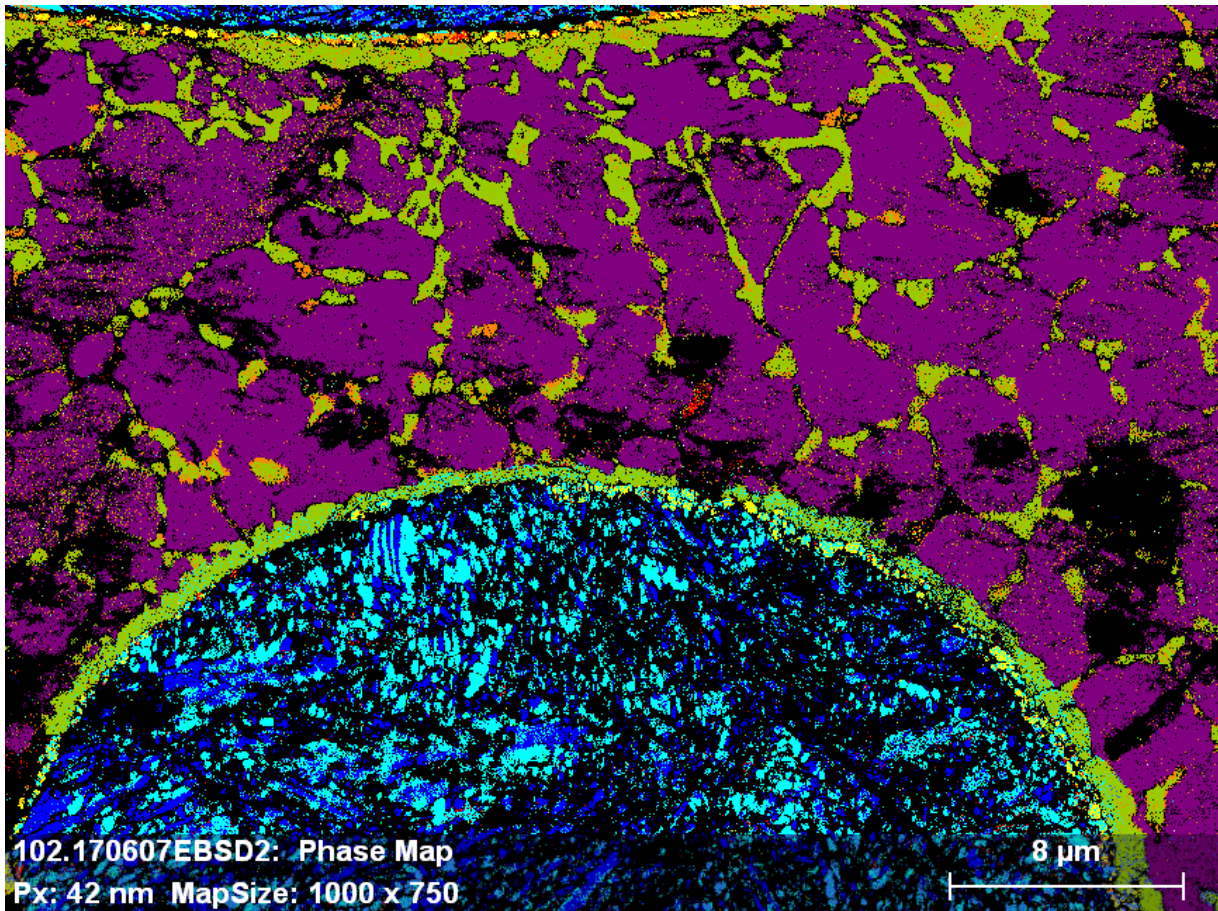
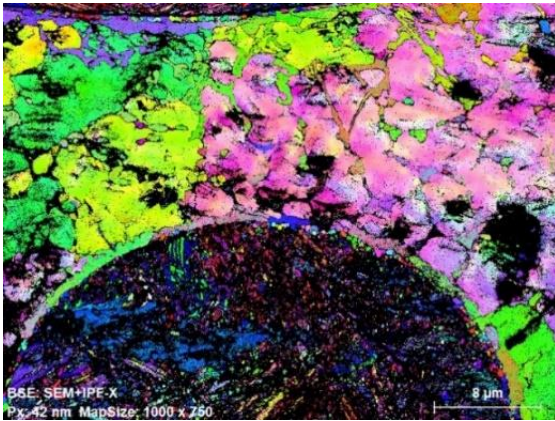


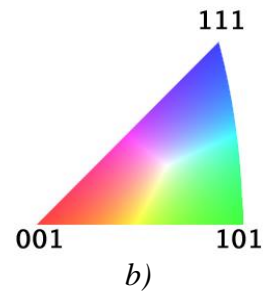
Figure 4-31: First complete EBSD phase map.

Table 4-12: Correlation of colors in Figure 4-31 with their lattice type. C is for cubical, T is for trigonal.

<i>PHASE</i>	<i>COLOR</i>
Austenite	Violet
Qusongite	Dark Blue
M ₄ C_C	Green
W ₂ C_T1	Light Blue
Cr ₂₃ C ₆	Orange
Chromium carbide M ₇ C ₃	Red



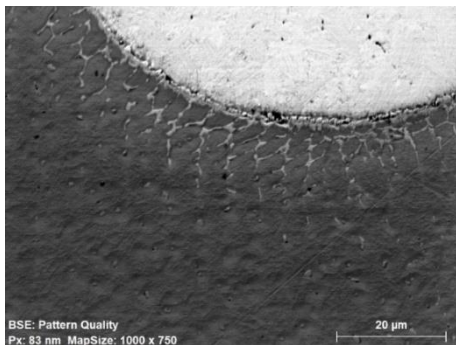
a)



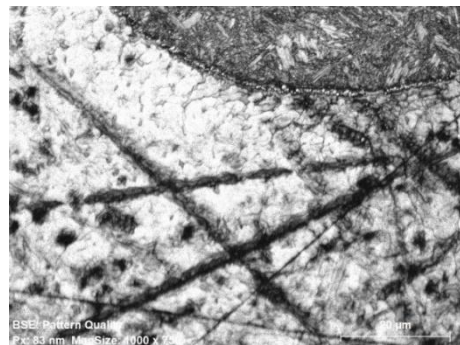
b)

Figure 4-32: a) Inverse Pole Figure (IPF) map in x direction displaying the different orientations of the crystals. b) Inverse Pole Figure color key.

A second EBSD analysis was performed on one side of a WC particle. The pattern quality [Figure 4-33b] shows more zones, that were not indexed in comparison with the previous analysis. In fact, scratches and even deformations of the surface are problems for EBSD. Figure 4-33a shows the position observed and Figure 4-33b shows the pattern quality. The sample has shifted, but not in a way to disturb the analysis.



a)



b)

Figure 4-33: Second EBSD. a) BSE picture of the analyzed zone. b) Pattern quality of the analysis.

Figure 4-34 shows the complete EBSD map. The phases correspond to the same colors as for the previous EBSD analysis [Figure 4-31]. Hence, the reference table [Table 4-12] and the considerations made are the same as for the previous analysis. Moreover, Figure 4-35b shows that there is an evolution of the carbides lattice formed between the matrix and the particle. In fact, the lattice near the particle corresponds to M_4C_C and far from the particle it becomes $M_{23}C_6$.

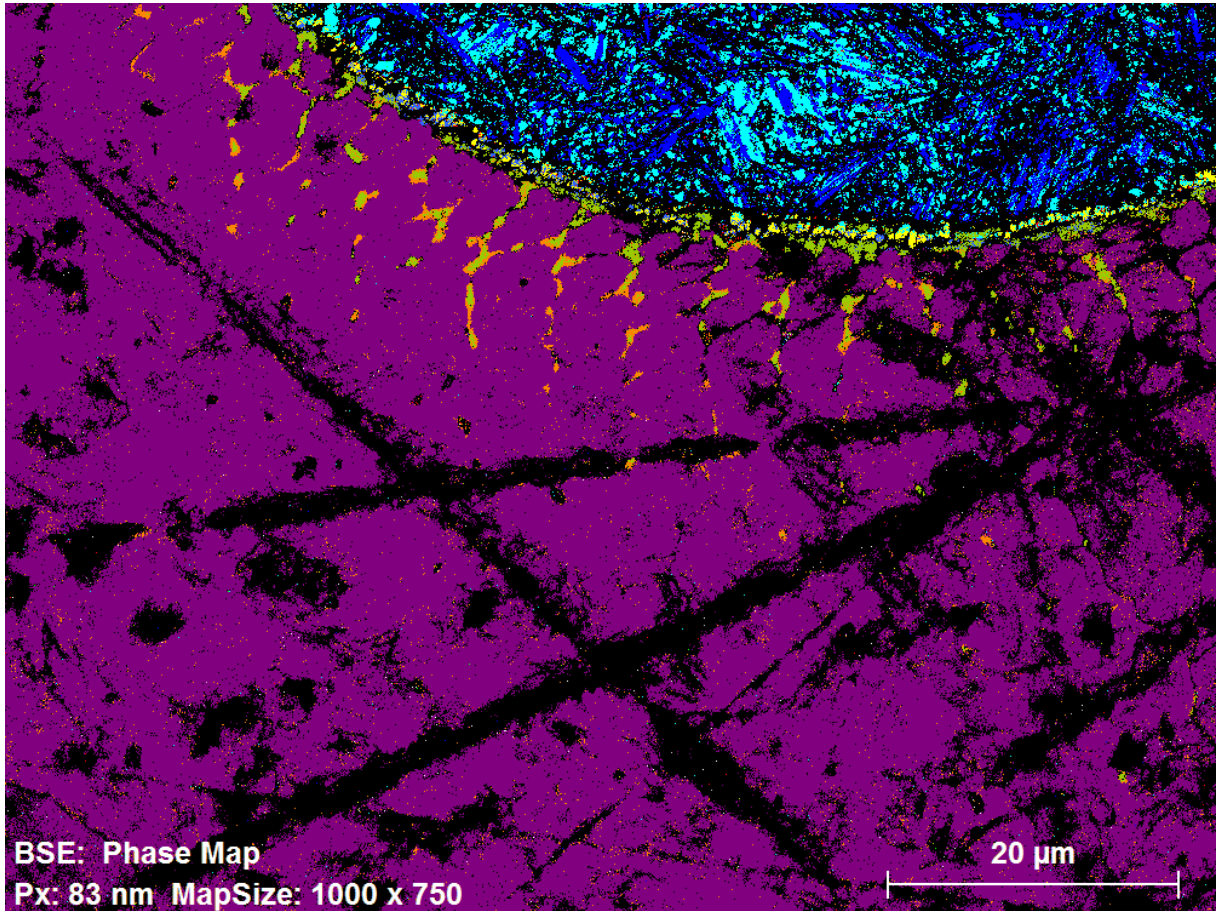
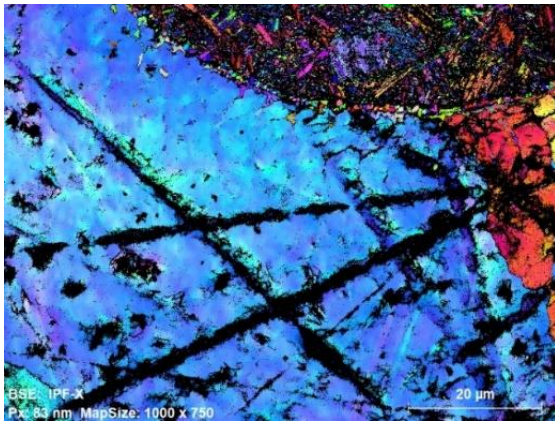


Figure 4-34: Second complete EBSD phase map.



a)

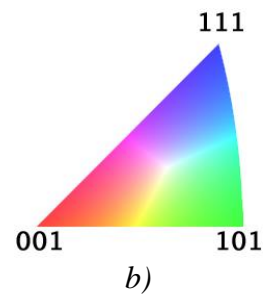


Figure 4-35: a) Inverse Pole Figure (IPF) map in x direction displaying the different orientations of the crystals. b) Inverse Pole Figure color key.

4.3 Thermo-calc simulations

Thermo-calc simulations were performed in order to help understanding the phases formed at pseudo-equilibrium conditions in the SS316L+WC system. Then, to determine the melting point of the system, and to understand the solidification range (from liquidus to solidus). The melting point and the solidification range were useful for the thermal analyses. Next, Thermo-calc has been used to understand the equilibrium phases at different temperatures. The phases and carbides hypothetically formed are shown in the graphs below.

4.3.1 Pseudo-equilibrium conditions simulations

Various simulations were performed using the Scheil program (ScheilGuliver Model), in Thermo-calc. Firstly, the simulation for the SS316L alone was performed. The composition of the steel was introduced in the program and the starting temperature was fixed. Figure 4-36 presents the different phases that form in SS316L. The melting temperature is found between 1420 °C and 1440 °C. The solidification range is between 1450 °C and 1240 °C. The possible phases and carbides are: Ferrite (delta), Austenite, carbide M_6C and carbides enriched with P and S. The dotted line illustrates the equilibrium conditions.

In a second step, other simulations were performed, considering various hypothetical percentages of W and C in the steel, in order to understand the solidification in different zones of the sample. In Figure 4-37 the supposed additional percentages of the elements are: 0.03 wt% C and 0.5 wt% W. The same phases were present as in SS316L with the further presence of $M_{23}C_6$. The addition of only 0,05 wt% of W, leads to the graph of Figure 4-38. The phases are the same as mentioned above. The addition of 5wt% W to the SS316L [Figure 4-39] provokes the formation of a new phase: the laves phase. The melting point and the range of solidification does not change with the variations reported.

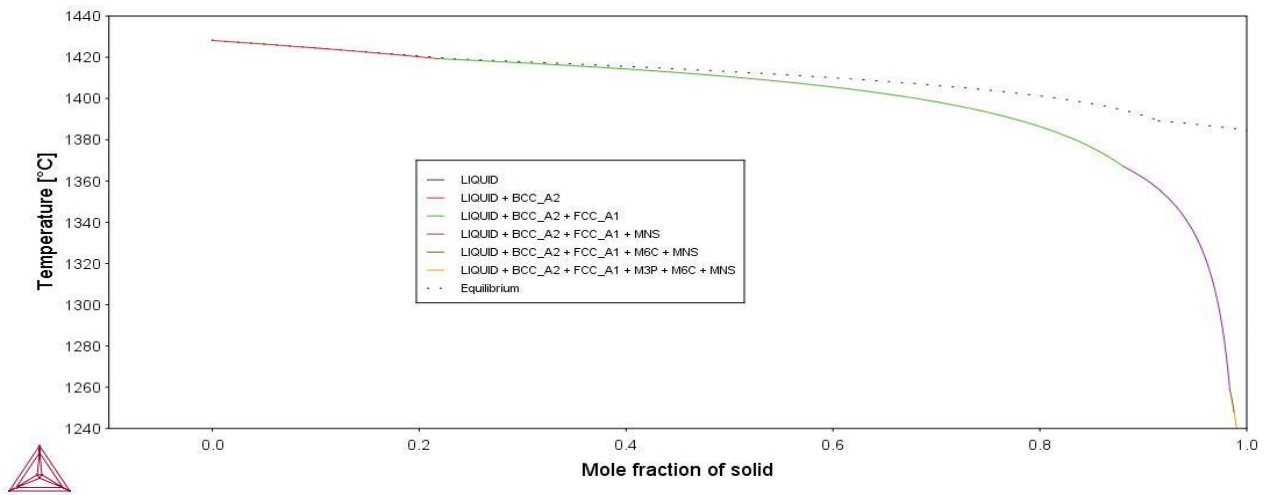


Figure 4-36: Scheil simulation performed with Thermo-calc software. SS316L.

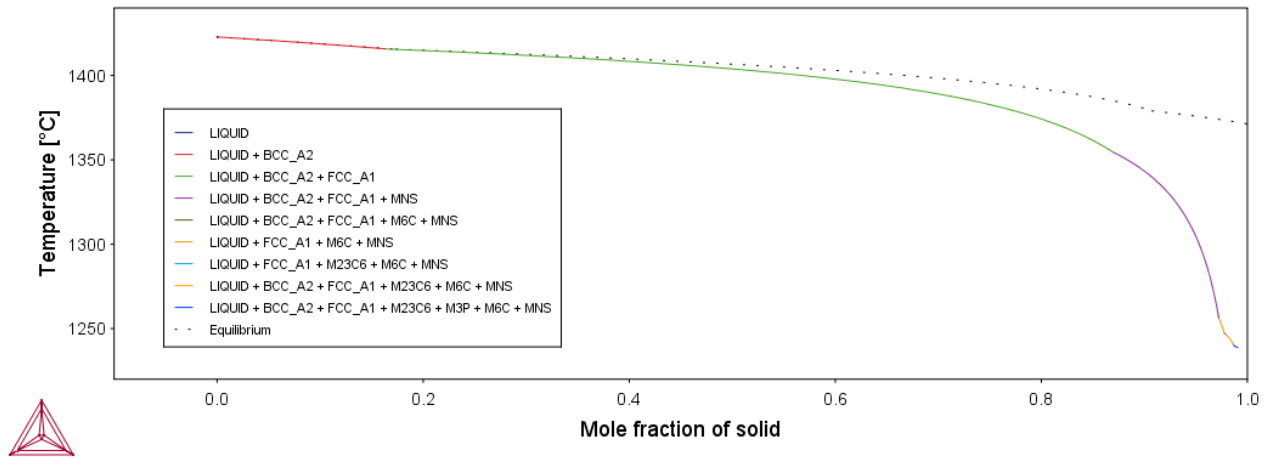


Figure 4-37: Scheil simulation performed with Thermo-calc software. SS316L + 0.03 wt% C and 0.5 wt% W.

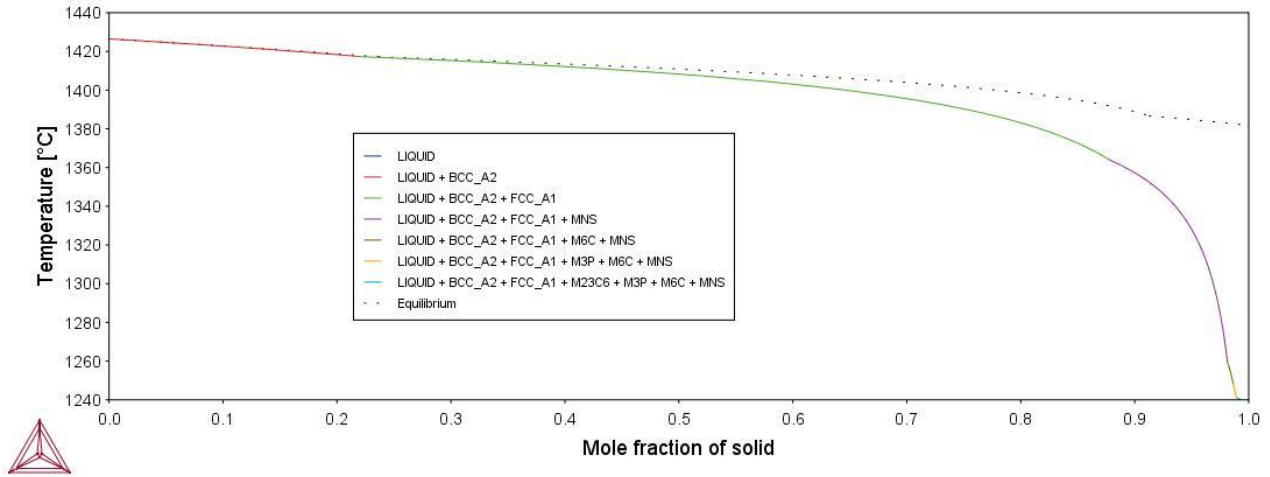


Figure 4-38: Scheil simulation performed with Thermo-calc software. SS316L + 0,05 wt% W.

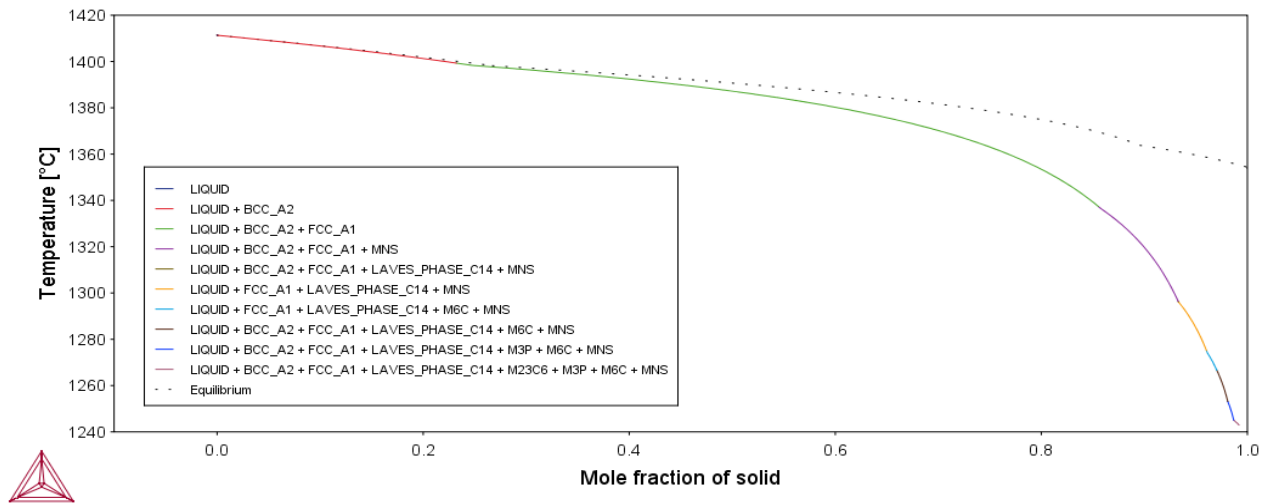


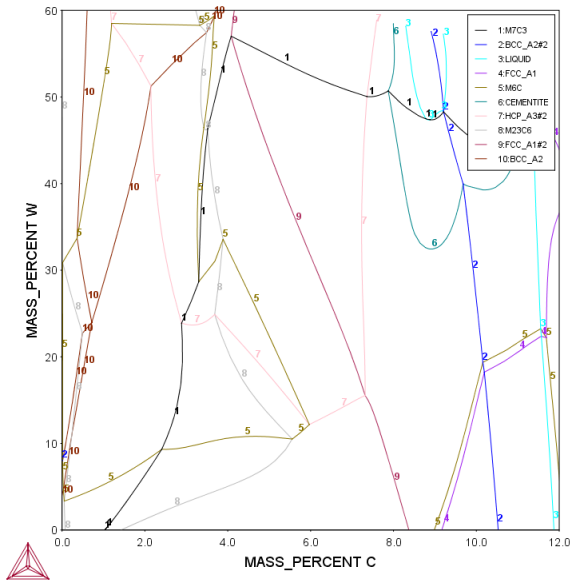
Figure 4-39: Scheil simulation performed with Thermo-calc software. SS316L + 5 wt% W.

4.3.2 Simulations of equilibrium diagram

These equilibrium diagrams [Figure 4-40] present the variation of W and C in the SS316L. The composition of the SS316L is placed in the origin of the axes and the temperature is fixed. Two diagrams have been calculated: Figure 4-40a shows the diagram calculated at 1000 °C, Figure 4-40b shows the diagram obtained at 1250 °C. Thermo-calc names the phases differently. For this purpose, the main ones are explained in Table 4-13.

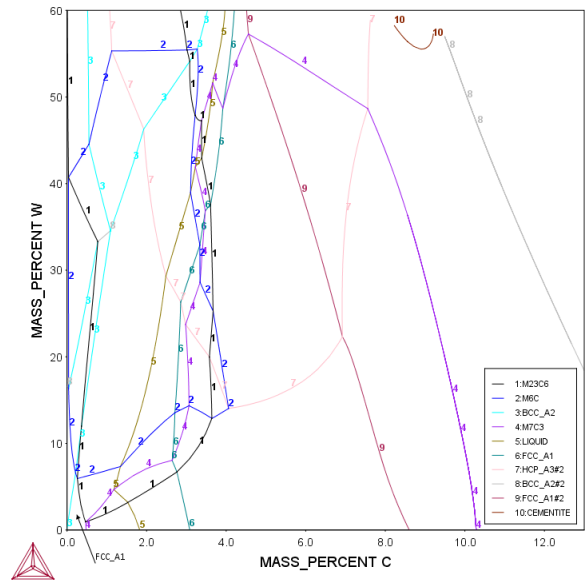
The equilibrium diagrams have been calculated to understand the equilibrium phases present in the system, at a fixed temperature.

2017.06.12.16.10.45
 TCFE6: C, CR, FE, MN, MO, NI, SI, W
 T=1273.15, W(Ni)=0.12, W(Mn)=2E-2, W(Si)=3E-4, W(Cr)=0.17, W(Mo)=2.5E-2, P=1E5, N=1



a)

2017.08.02.17.12.03
 TCFE6: C, CR, FE, MN, MO, NI, SI, W
 T=1523.15, W(Ni)=0.12, W(Mn)=2E-2, W(Si)=3E-4, W(Cr)=0.17, W(Mo)=2.5E-2, P=1E5, N=1



b)

Figure 4-40: Equilibrium diagrams obtained with Thermo-calc. a) Diagram obtained with fixed a temperature of 1000 °C. b) Diagram obtained with a fixed temperature of 1250 °C.

Table 4-13: Name given to the phases in the Thermo-calc software and actual names.

Thermo-calc name	BCC_A2	BCC_A2#2	BCC_A2#3	FCC_A1	FCC_A1#2	FCC_A1#3	HCP_A3#2
Name	Ferrite	Ferrite	Ferrite	Austenite	MC	MC	M ₂ C

4.4 Thermal analyses results

Three DTA tests and one DSC tests [Table 3-8] were taken to study phase transformations in sample W27. The name DT1 is referred to the DTA test up to 1500 °C at 5 °C/min. With DT3 is indicated a DTA analysis up to 1500 °C at 1 °C/min. DT4 refers to a DTA test up to 1200 °C at 5 °C/min and DS4 refers to a DSC test up to 1200 °C at 5 °C/min. The SS316L after SLM process was tested up to 1500 °C at 5 °C/min in the DTA to help understand the peaks observed with the DTA tests on the W27 sample. SLM process is different from Laser Cladding, but the thermal cycle during printing is similar. For this reason, it has been reasonably possible to consider it as a reference.

The maximum temperatures of the tests were chosen following the Thermo-calc analyses. The simulations showed that the melting point was between 1420 °C and 1440 °C, thus it was taken 1500 °C, to ensure the complete melting. The beginning of the formation of the liquid, for all the hypothetical systems, was around 1240 °C Therefore, the temperature chosen to avoid the formation of liquid was 1200 °C.

In the heating curves, all major peaks are endothermic and they represent destabilization, decomposition and fusion. Meanwhile, in the cooling curves all the peaks can be associated with precipitation, eutectic reaction, etc (see section 2.5).

4.4.1 DTA

4.4.1.1 SS316L SLM up to 1500 °C at 5 °C/min

4.4.1.1.1 Heating

The DTA thermogram for the heating of SLM SS316L, is given in Figure 4-41. In order to obtain greater accuracy on the start and end points of the transformation, the curve which gives the first derivative of the thermogram is also displayed. After the DTA tests, samples were observed to the optical and SEM (see section 4.4.2). Table 4-14 summarizes the reactions and their relative temperatures.

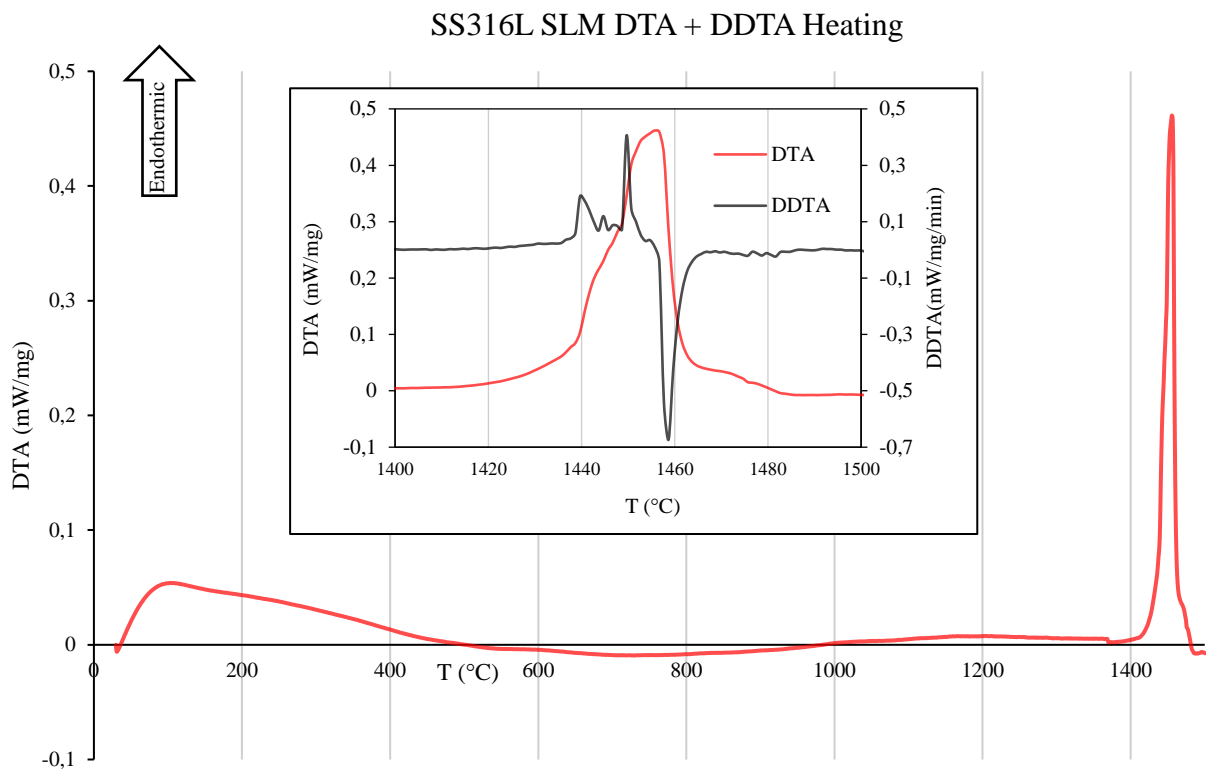


Figure 4-41: Heating thermogram for SS316L produced by SLM process.

Table 4-14: Attribution of the different transformations to each peak. SLM SS316L heating.

Peak	Start Temperature (°C)	Max/Min Temperature (°C)	End Temperature (°C)	Reaction or phase transformation
H1	550	600	670	Dissolution of the secondary carbides (first type)
H2	1060	1100	1200	Dissolution of the secondary carbides (third type)
H3	1440	?	1458	$\gamma \rightarrow L+\delta$ Inverse peritectic transformation
H4	1449	1455	1460	$L+\delta \rightarrow L$ Fusion of δ -ferrite

4.4.1.1.2 Cooling

Figure 4-42 displays the cooling part of the previous DTA curve. The two main reactions are reported in Table 4-15.

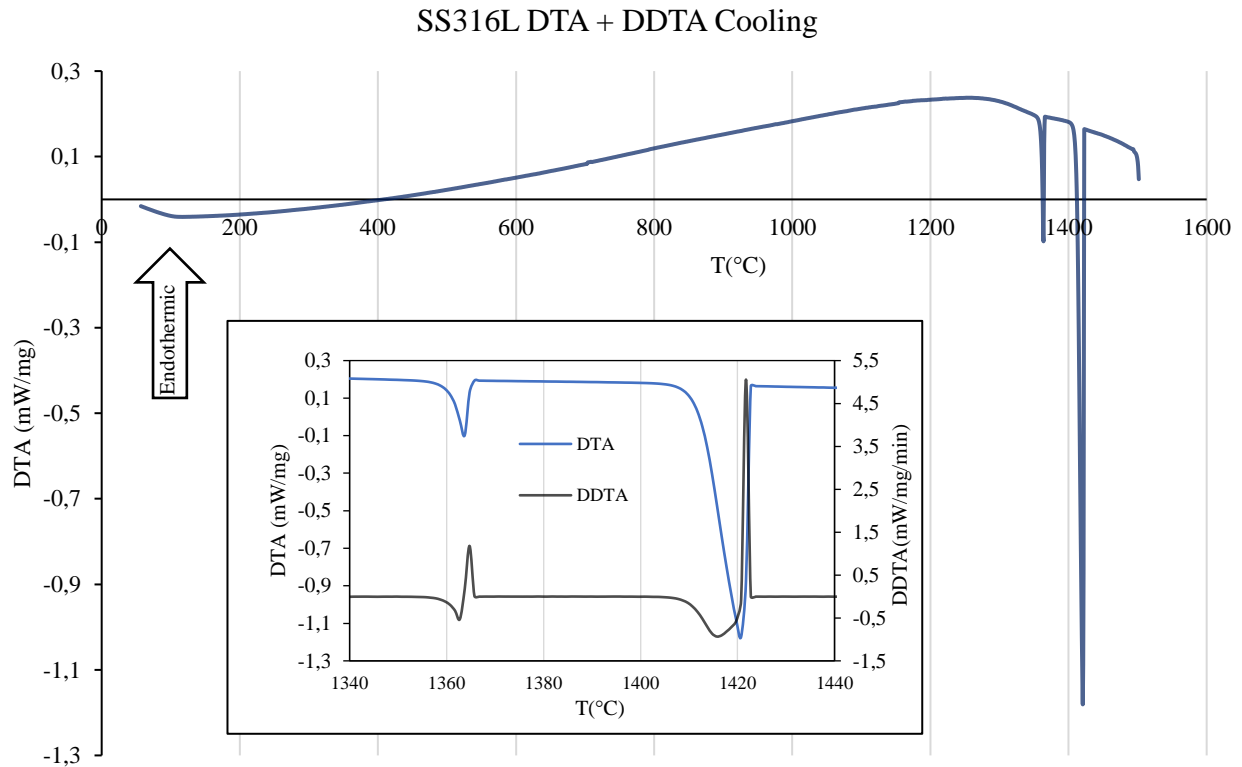


Figure 4-42: Cooling thermogram for SS316L produced by SLM process.

Table 4-15: Attribution of the different transformations to each peak. SLM SS316L cooling.

Peak	Start Temperature (°C)	Max/Min Temperature (°C)	End Temperature (°C)	Reaction or phase transformation
C1	1410	1418	1420	L- \rightarrow L+ δ Formation of δ -ferrite
C2	1361	1363	1365	L+ δ - \rightarrow γ Peritectic transformation

4.4.1.2 DTI

In this subchapter are reported the DTA curves up to 1500 °C at 5 °C/min of sample W27.

4.4.1.2.1 Heating

Figure 4-43 shows the DTA curve upon heating. Table 4-16 reports the interpretation of the peaks. The presence of the particles provokes the formation of new compounds; hence the curve is very different from the heating curve obtained for SLM SS316L.

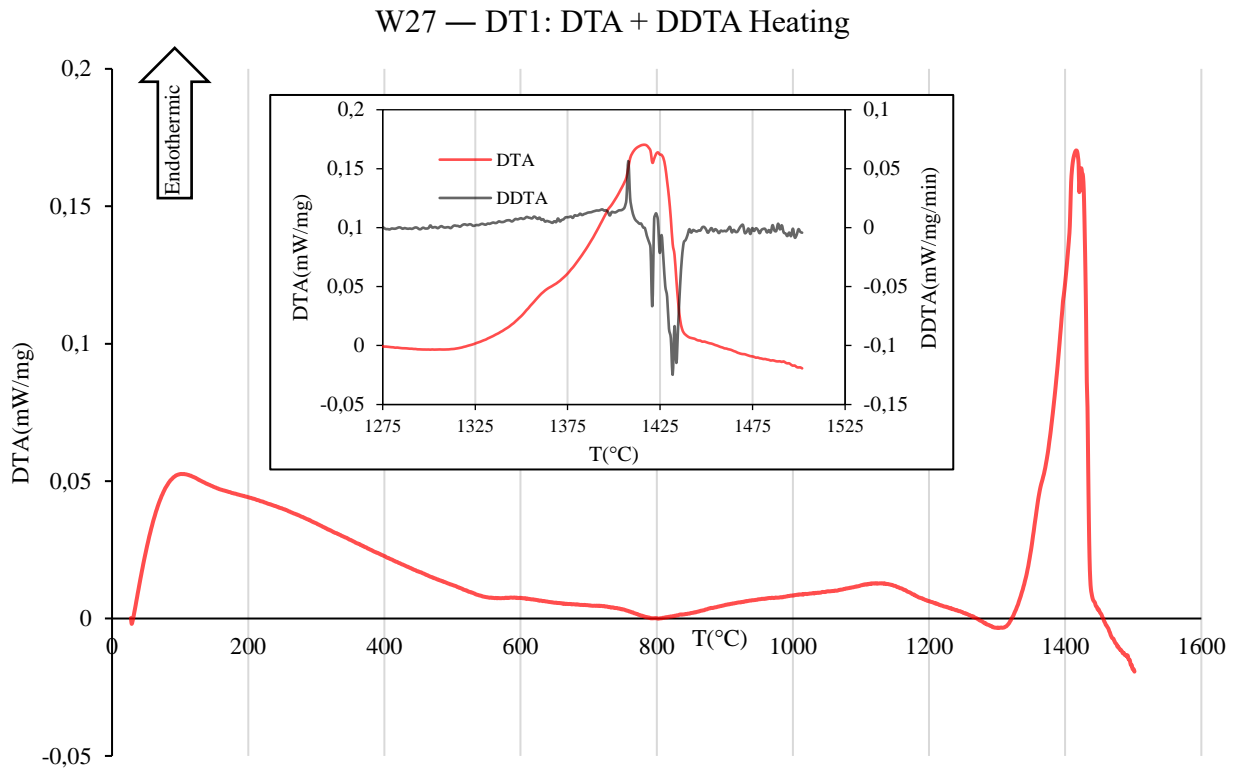


Figure 4-43: Heating thermogram for W27 (test DT1) produced by laser cladding process.

Table 4-16: Attribution of the different transformations to each peak. DT1 test on laser clad W27, heating.

Peak	Start Temperature (°C)	Max/Min Temperature (°C)	End Temperature (°C)	Reaction or phase transformation
H1	555	600	?	Dissolution of secondary carbides (first type)
H2	?	725	800	Dissolution of secondary carbides (second type)
H3	?	1130	1190	Dissolution of the secondary carbides (third type)
H4	1310	1360	?	Direct fusion of eutectic carbides in the interdendritic spaces
H5	1310	1394	?	Direct fusion of eutectic carbides of Cr (M_7C_3 carbide)
H6	1310	1420	?	Direct fusion of eutectic carbides of W (M_6C carbide)
H7	1310	1416	?	$L+\gamma \rightarrow L$ Fusion of austenite phase
H8	?	1426	1432	Direct fusion of W-rich M_2C (enlarged circular crown: see section 4.4.2.1)

4.4.1.2.2 Cooling

Figure 4-44 shows the cooling curve complementary to the previous heating one [Figure 4-43]. The differences with the cooling curve of the DTA test on the SS316L are the peaks formed between 700 °C and 1000 °C. In Table 4-17 are reported the possible meanings of the peaks.

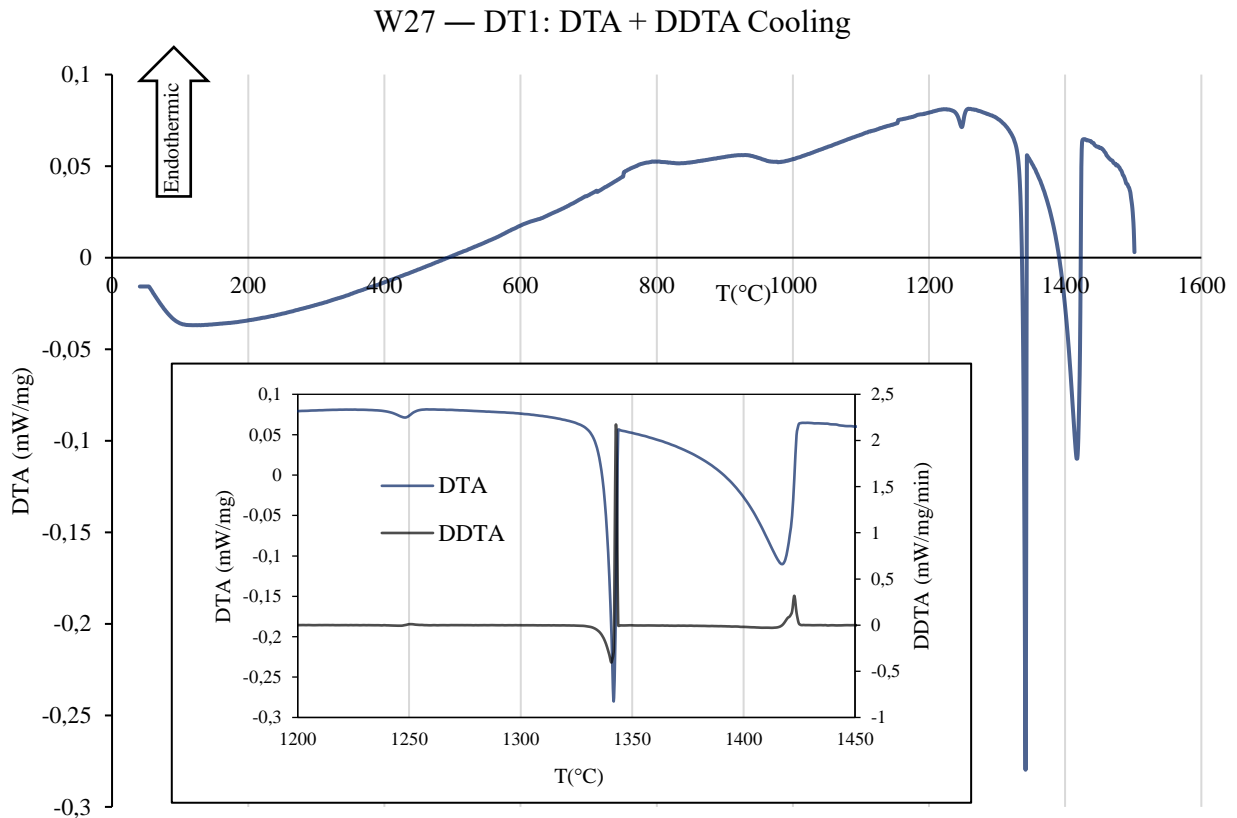


Figure 4-44: Cooling thermogram for W27 (test DT1) produced by laser cladding process.

Table 4-17: Attribution of the different transformations to each peak. DT1 test on laser cladded W27, cooling.

Peak	Start Temperature (°C)	Max/Min Temperature (°C)	End Temperature (°C)	Reaction or phase transformation
C1	1433	1415	?	L- \rightarrow γ Formation of austenite phase
C2	1344	1341	?	Formation of open M ₂ C eutectic carbide
C3	1255	1249	1230	Formation of complex-regular M ₂ C eutectic carbide
C4	?	746-980	?	Continuous changing of the composition with precipitation of secondary carbides inside the grains

4.4.1.3 DT3

In this subchapter are reported the DTA curves up to 1500 °C at 1 °C/min performed on W27 sample.

4.4.1.3.1 Heating

In respect to the DTA performed at higher rate, this test [Figure 4-45] shows a different behavior. The peaks can be distinguished more easily. Table 4-18 collects the meanings and the temperature ranges of each peak.

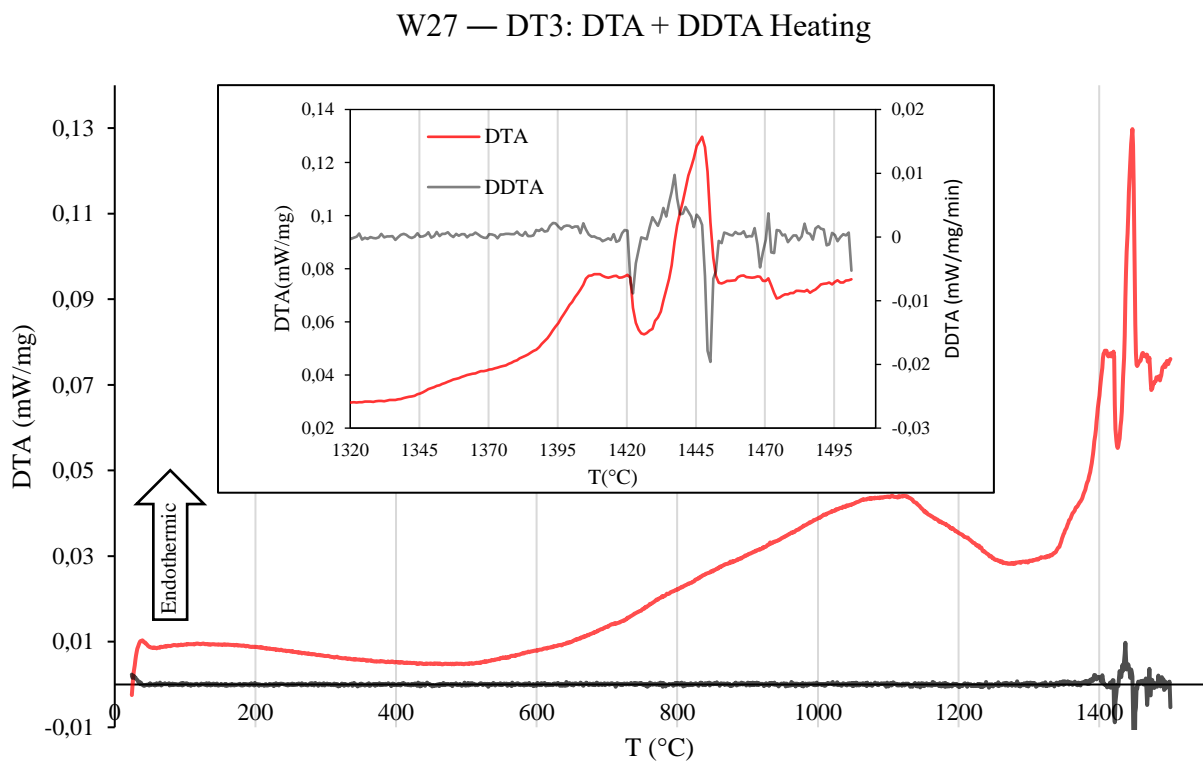


Figure 4-45: Heating thermogram for W27 (test DT3) produced by laser cladding process.

Table 4-18: Attribution of the different transformations to each peak. DT3 test on laser cladded W27, heating.

Peak	Start Temperature (°C)	Max/Min Temperature (°C)	End Temperature (°C)	Reaction or phase transformation
H1	?	600	?	Dissolution of secondary carbides (first type)
H2	?	703	780	Dissolution of secondary carbides (second type)
H3	?	1104	1200	Dissolution of the secondary carbides (third type)
H4	1330	1364	?	Direct fusion of eutectic carbides in the interdendritic spaces
H5	1330	1406	?	Direct fusion of eutectic carbides of Cr (M_7C_3 carbide)
H6	?	1420	1427	Direct fusion of eutectic carbides of W (M_6C carbide)
H7	1430	1446	?	$L \rightarrow L + \gamma$
H8	?	1472	1475	Direct fusion of W-rich M_2C (enlarged circular crown: see section 4.4.2.1)

4.4.1.3.2 Cooling

The cooling [Figure 4-46] curve present almost the same peaks as the cooling curve at 5 °C/min. Peaks meaning is reported in Table 4-19.

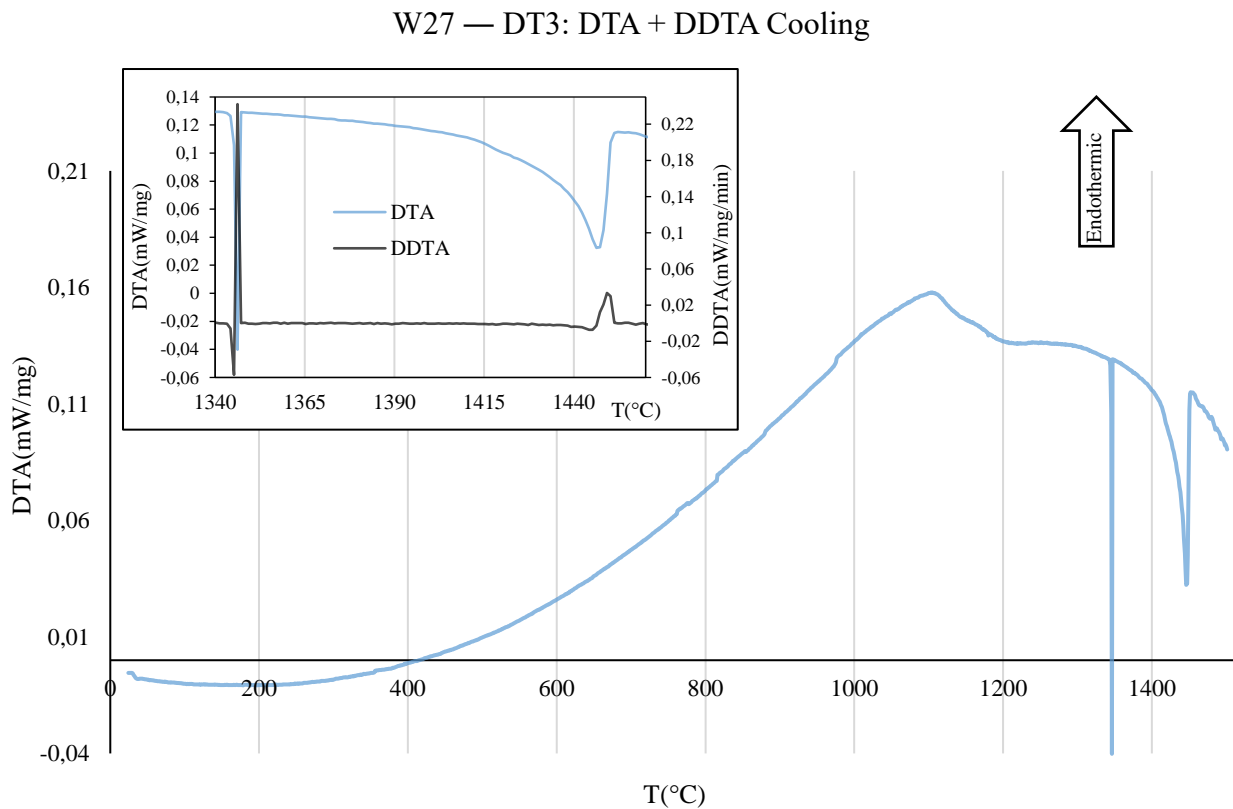


Figure 4-46: Cooling thermogram for W27 (test DT3) produced by laser cladding process.

Table 4-19: Attribution of the different transformations to each peak. DT3 test on laser clad W27, cooling.

Peak	Start Temperature (°C)	Max/Min Temperature (°C)	End Temperature (°C)	Reaction or phase transformation
C1	1451	1446	1355	L->L+γ
C2	1350	1346	1346	Formation of M ₂ C regular
C3	?	1105	?	Continuous changing of the composition with precipitation of secondary carbides inside the grains

4.4.1.4 DS4

In this subchapter are reported the DSC curves up to 1200 °C at 5 °C/min.

4.4.1.4.1 Heating

The two peaks observed are matching with the temperatures of the peaks for secondary carbides observed in the other curves. Below, Figure 4-47 and Table 4-20 present the heating curve and the table of the possibly corresponding peaks.

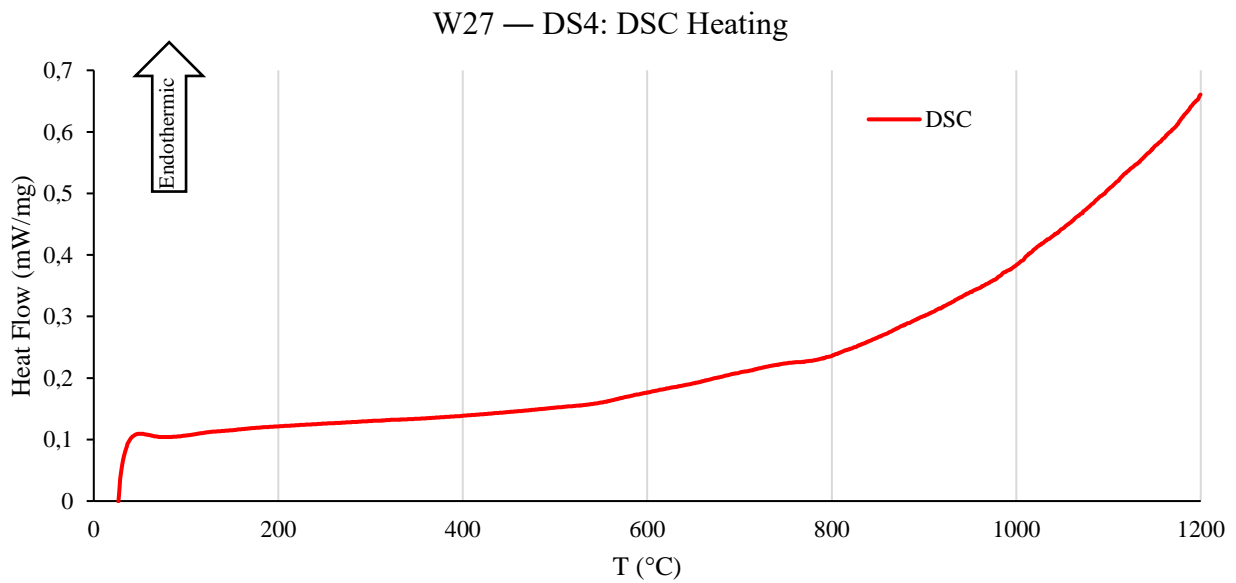


Figure 4-47: Heating thermogram for W27 (test DS4) produced by laser cladding process.

Table 4-20: Attribution of the different transformations to each peak. DS4 test on laser clad W27, heating.

Peak	Start Temperature (°C)	Max/Min Temperature (°C)	End Temperature (°C)	Reaction or phase transformation
H1	585	?	640	Dissolution of secondary carbides (first type)
H2	700	743	780	Dissolution of secondary carbides (second type)

4.4.1.4.2 Cooling

The cooling curve is reported in Figure 4-48.

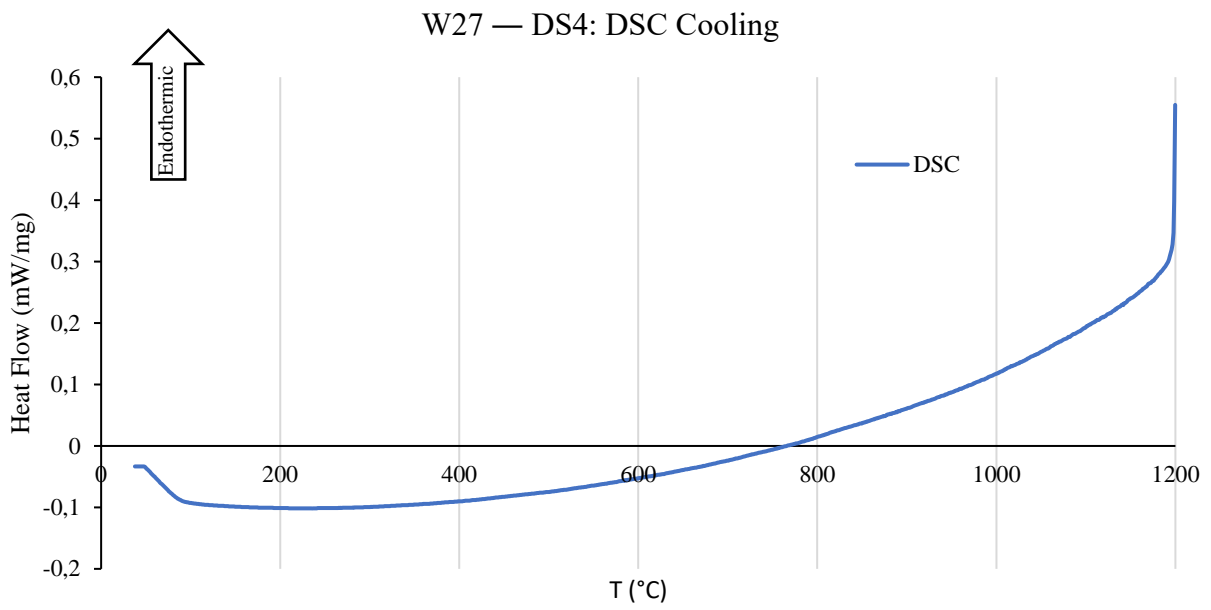


Figure 4-48: Cooling thermogram for W27 (test DS4) produced by laser cladding process.

4.4.2 Microstructural observations of the samples after Thermal Analyses

The microstructure of the samples after thermal analyses has been studied by mean of optical and electronic microscopy (see section 3.5), to study the change in microstructure with different cooling rates. Sample W27 was melted up to 1500 °C at 5 °C/min and at 1 °C/min. After these two tests, the WC particles were melted in the matrix. For this reason, it was also decided to heat the sample up to the lower temperature of 1200 °C at 5 °C/min [Table 3-8].

4.4.2.1 DS4 and DT4

This subchapter describes the microstructure of the sample heated up to 1200 °C at a rate of 5 °C/min. A DTA analysis was performed up to this temperature but did not reveal useful peaks. However, it allows us to verify that there was no formation of a liquid phase. Hence, it was possible to perform a DSC analysis. This allowed us to understand better and verify the respective positions of the peaks. The samples DT4 and DS4 show the same thermal history. Consequently, the microstructure between the two samples does not change.

First, an overview has been gained of the sample DS4. As shown in Figure 4-49, the original WC particles are still present. In fact, the matrix did not reach melting thus solid-state diffusion occurs. Other investigations with polarized light were performed. This sample, in respect to the “as built” condition [Figure 4-23], shows an enlargement of the circular crown around the particles, as reported in the Figure 4-50. Furthermore, there is the formation of another thinner circular crown inside the circumference of the particles [Figure 4-50d]. The black spots around the particles are porosities as shown by SEM observations [Figure 4-51].

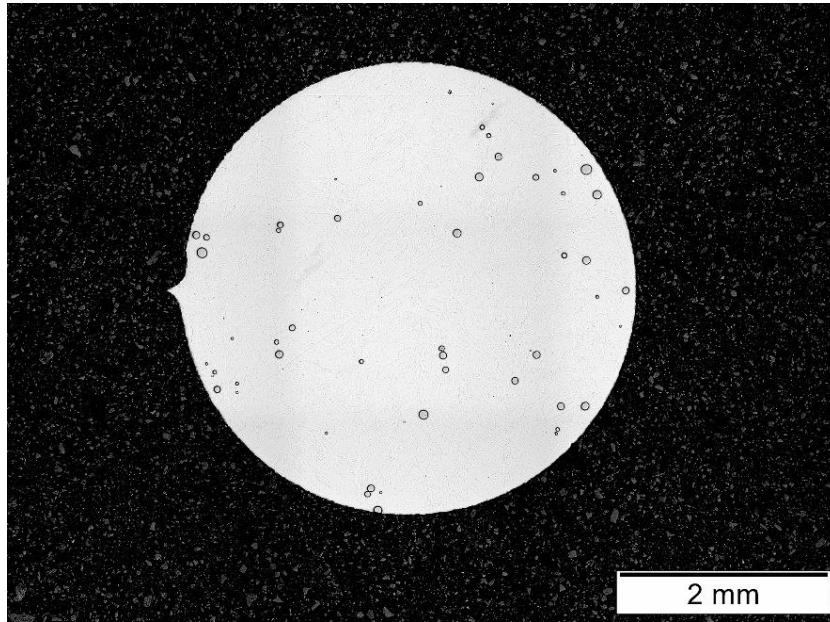
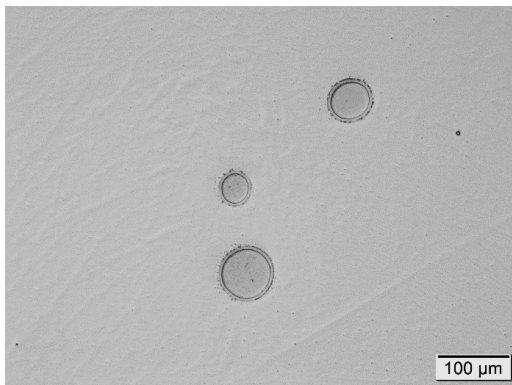
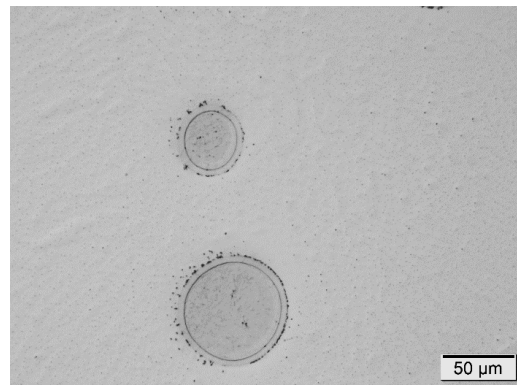


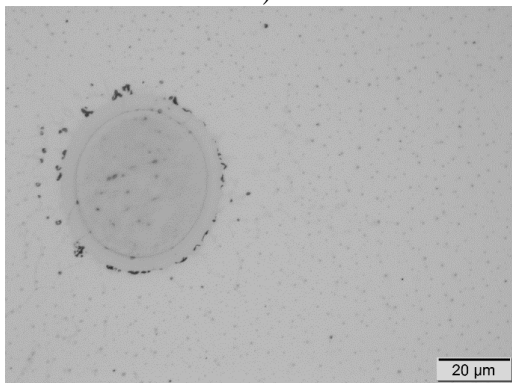
Figure 4-49: Overview of sample DS4.



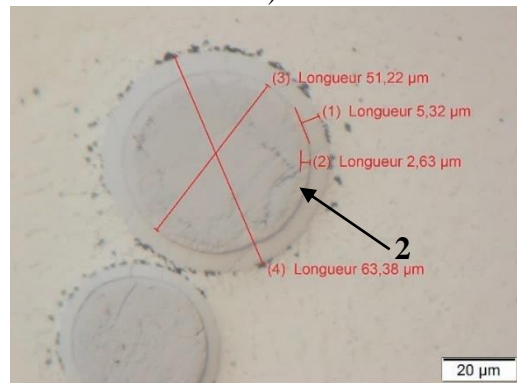
a)



b)



c)



d)

Figure 4-50: Optical micrograph of the zone near the particles, sample DS4. a) Magnification 100x. b) Magnification 200x. c) Magnification 500x. d) different zones observed and their different thickness. Magnification 500x.

SEM-BSE observations and EDS analyses were also carried out. Figure 4-51 presents images of the dissolution of the WC particles at increasingly magnification (from a to d). Figure 4-51a shows that the orientation of the dendrites remains unaltered. Figure 4-51b does not show a totally continuous link between the carbides between the dendrites that can be observed in the additive manufacturing conditions. Carbides around the dendrites are now more rounded and dispersed, owed to Ostwald ripening mechanism. The formation of porosities occurs often around the particles. Then, Figure 4-51c and d show that the large circular crown is cracked. Finally, there is the precipitation of very fine secondary carbides of cubical shape, mainly in the vicinity of the particles [Figure 4-52]. The compositions of the various constituents of the microstructure are collected in Table 4-21 and 4-22. The respective positions of the analysis are indicated in Figure 4-51. The composition of the external zone of the particles [Figure 4-50d] (2) shows more W and less C. This corresponds to an MC with less carbon because of the faster diffusion of the C in comparison with the W. The detected composition of the secondary carbides [Figure 4-52] (7) can be biased because of their small size: a higher amount of Fe is measured including a contribution from the matrix. The morphology suggest that their formation is monocrystalline and they might correspond to a MC-type carbide.

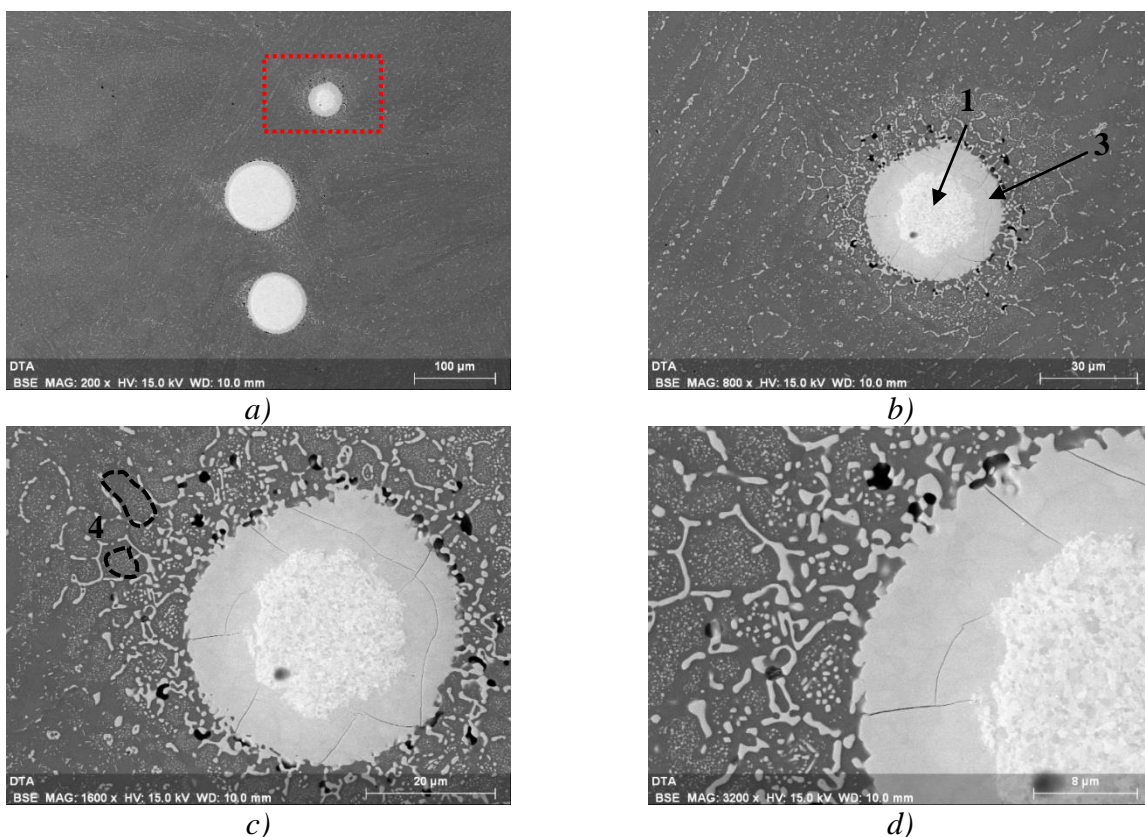


Figure 4-51: SEM-BSE images of the dissolution of the particles, sample DS4. a) 200x. b) 800x. c) 1600x. d) 3200x.

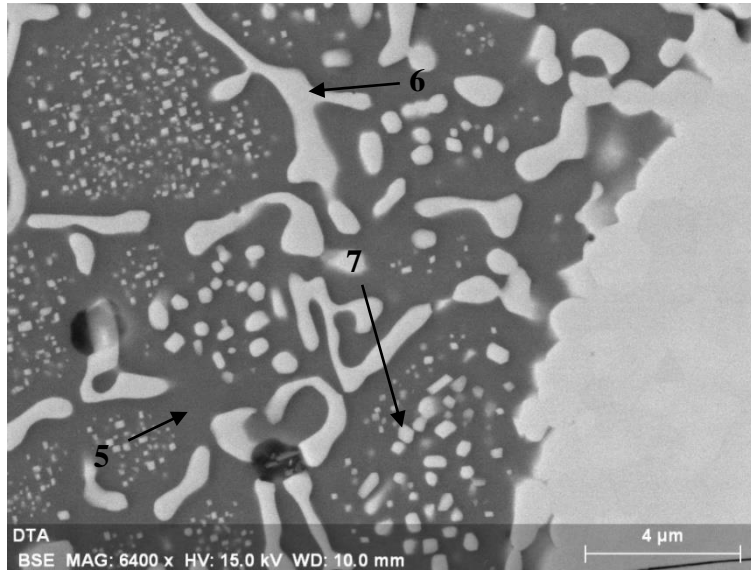


Figure 4-52: Secondary carbides formed by the dissolution of particles.

Table 4-21: Compositions in wt% and relative deviation standard values. Sample DS4.

Position in Figure 4-51, 4-52	wt%	C	Cr	Fe	Ni	W	Mo	Si
1	Inside the particle	6,7 ±0,9	0,4 ±0,3	0,5 ±0,4	0,2 ±0,2	92,3 ±0,9	0	0
2	Zone in the particle described with optical microscope (Figure 4-50d)	2,3 ±0,9	0,7 ±0,2	0,7 ±0,5	0,4 ±0,1	95,9 ±1,5	0	0
3	Enlarged circular crown	4,8 ±0,6	8,4 ±1,3	19,1 ±1,9	1,5 ±0,6	65,5 ±3,0	0,6 ±0,7	0
4	In the grain, average with secondary carbides	2,4 ±0,7	13,4 ±0,8	61,5 ±4,4	8,9 ±0,9	12,6 ±5,0	0,8 ±0,5	0,1 ±0
5	In the grain, without secondary carbides	2,4 ±1,1	13,5 ±0,8	70,6 ±0,3	9,7 ±0,9	2,8 ±0,1	0,3 ±0,2	0,6 ±0,2
6	Carbides around the dendrites	5,3 ±0,4	12,1 ±0,8	27,3 ±4,8	2,3 ±0,5	47,2 ±5,0	5,2 ±1,1	0
7	Secondary carbides	4,1 ±0,5	13,1 ±0,4	34,9 ±1,7	4,4 ±0,7	39,4 ±2,4	4,0 ±0,5	0

Table 4-22: Compositions in at% and relative deviation standard values. Sample DS4.

Position in Figure 4-51, 4-52	at%	C	Cr	Fe	Ni	W	Mo	Si	Type
1	Inside the particle	51,5 ±4,0	0,6 ±0,6	0,8 ±0,7	0,3 ±0,4	46,8 ±3,4	0	0	MC
2	Zone in the particle described with optical microscope (Figure 4-50d)	24,7 ±8,1	1,9 ±0,6	1,6 ±1,2	0,8 ±0,2	70,8 ±9,0	0	0	MC
3	Enlarged circular crown	31,0 ±2,5	12,4 ±1,6	26,4 ±1,9	2,0 ±0,9	27,6 ±2,5	0,5 ±0,6	0	M ₂ C
4	In the grain, average with secondary carbides	11,2 ±3,2	14,2 ±1,0	60,8 ±3,5	8,3 ±0,6	3,9 ±1,6	0,5 ±0,3	0,2 ±0,3	
5	In the grain without secondary carbides	10,3 ±4,3	13,4 ±0,3	65,5 ±2,7	8,6 ±1,0	0,8 ±0,1	0,2 ±0,1	1 ±0,4	
6	Carbides around the dendrites	28,3 ±0,8	15,1 ±1,4	31,4 ±3,8	2,5 ±0,5	16,7 ±2,5	3,5 ±0,8	0	M ₂ C
7	Secondary carbides	22,1 ±2,5	16,2 ±0,5	40,3 ±2,0	4,8 ±0,8	13,8 ±0,8	2,7 ±0,3	0	Secondary precipitations

4.4.2.2 DT1

The “as built” W27 sample was heated up to 1500 °C at 5 °C/min and cooled at the same rate. The sample was heated above the melting point of the matrix (Melting range: 1380-1400 °C [17]). The microstructure after this thermal cycle was studied.

The starting point was the analysis of the overall surface of the sample, with the optical microscope [Figure 4-53]. Porosities and big grains are present, but the WC particles have disappeared. Owing to the prolonged exposure at elevated temperatures, WC particles have been dissolved into the matrix. Polarized light observations were performed to investigate the carbides formed at the grain boundaries which revealed two types of carbides [Figure 4-54c]. They are both eutectic carbides: the first forms small and rounded eutectic isles in the matrix, while the other carbide forms a peripheric layer around the first one. Figure 4-54c and d reveal the presence of cavities due to shrinkage. These are always found in the vicinity of the finer eutectic carbide.

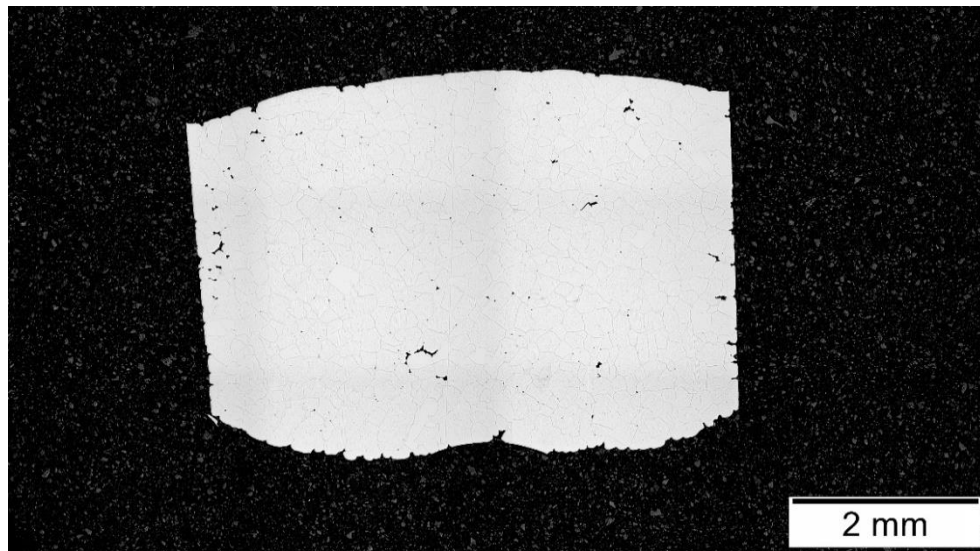


Figure 4-53: Overview of sample DT1.

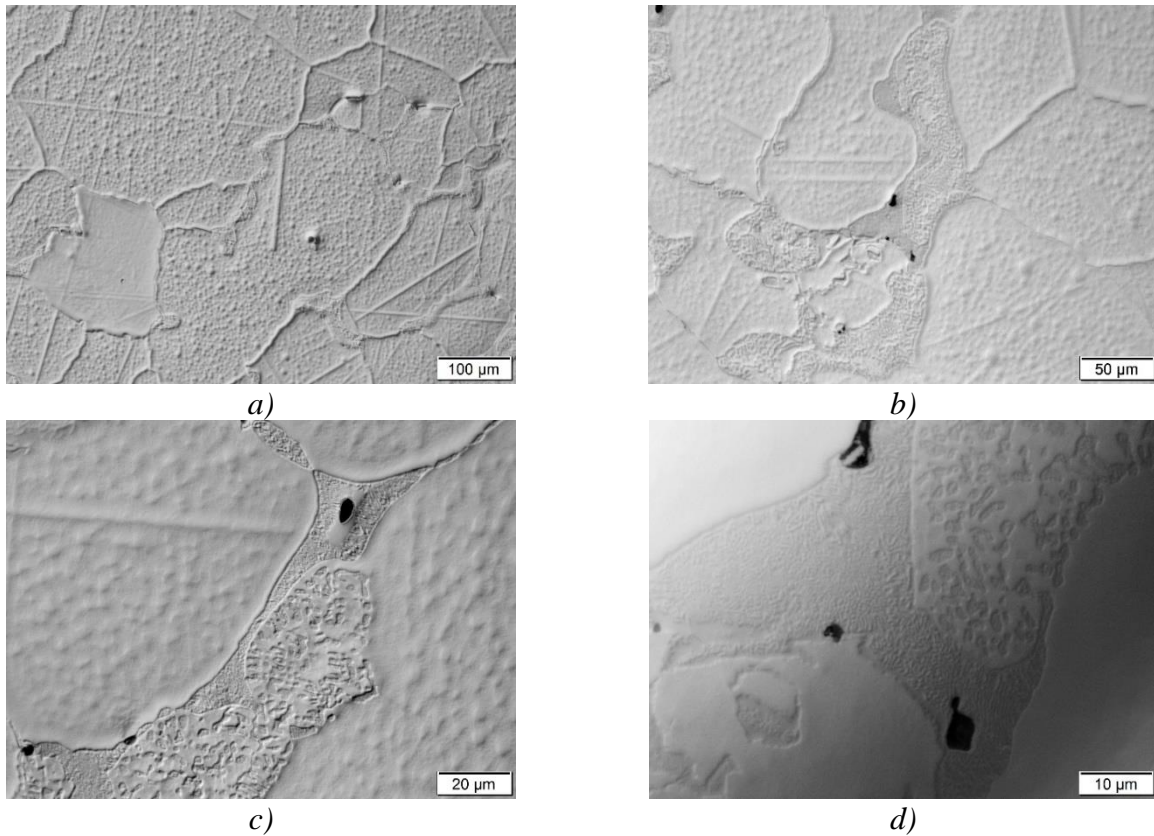


Figure 4-54: Optical images, sample DT1. a) 100x. b) 200x. c) 500x. d) 500x.

The sample was observed with SEM microscope. BSE observation and EDS analyses were performed. Figure 4-55 shows the grains with different shades of grey, revealing that the composition varies from grain to grain. Finer carbides were observed at high magnification revealing very fine lamellae [Figure 4-56].

The compositions of the different constituents are collected in Table 4-23 and 4-15, the various positions are indicated in Figure 4-55.

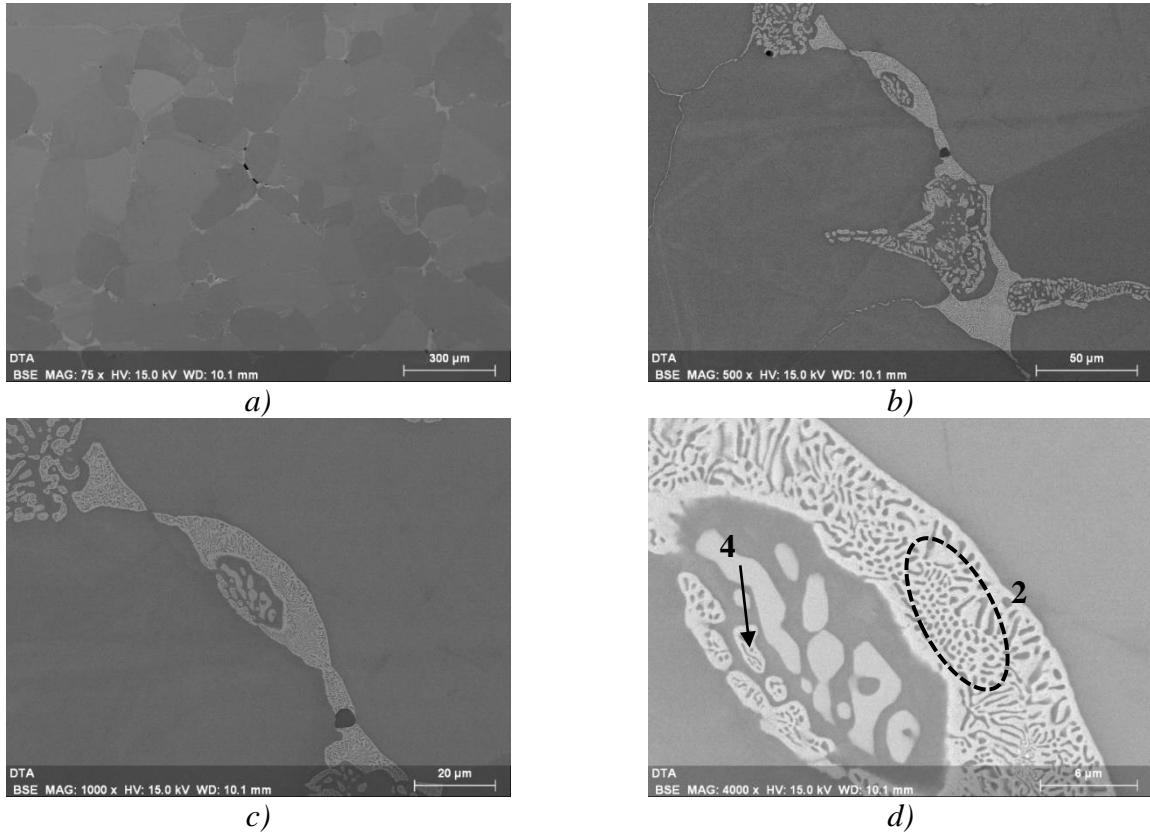


Figure 4-55: SEM-BSE images, sample DT1. a) 200x. b) 800x. c) 1600x. d) 3200x.

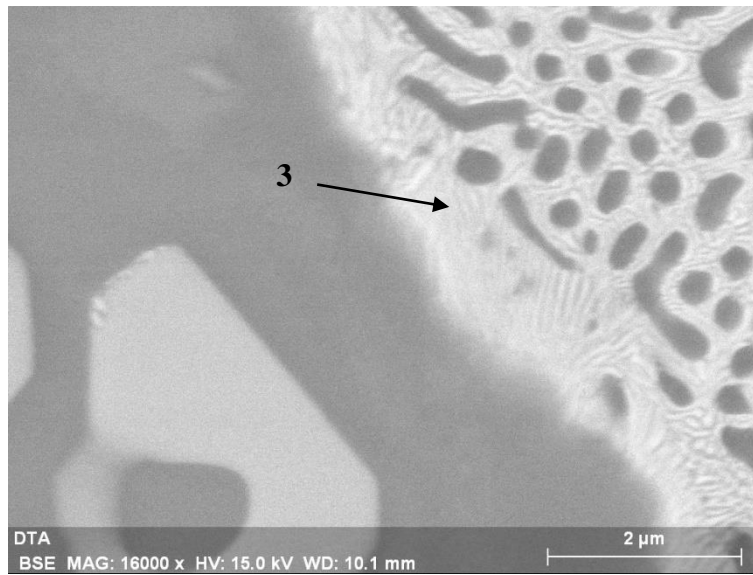


Figure 4-56: Finer lamellae revealed with higher magnifications.

Table 4-23: Compositions in wt% and relative deviation standard values. Sample DT1.

Position in Figure 4-55	wt%	C	Cr	Fe	Ni	W	Mo	Si	Mn
1	Matrix	3 ±0,6	15,6 ±1	62,8 ±2,1	9,3 ±0,8	6,4 ±2,4	1,1 ±0,8	0,2 ±0,2	1,3 ±0,4
2	Average in finer carbide	5,1 ±0,9	21,1 ±2,0	42,9 ±6,6	3,8 ±1,7	21,0 ±6,0	6,0 ±1,4	0 ±0,1	0
3	Finer carbide: lighter part	6,2 ±0,4	21,1 ±1,6	36,3 ±1,3	2,4 ±0,4	28,1 ±0,9	5,8 ±0,6	0 ±0,1	0
4	Eutectic isles in the matrix	5,1 ±0,8	21,6 ±1,7	43,1 ±2,2	2,7 ±1,2	21,8 ±3,2	5,7 ±1,1	0	0

Table 4-24: Compositions in at% and relative deviation standard values. Sample DT1.

Position in Figure 4-55	at%	C	Cr	Fe	Ni	W	Mo	Si	Mn	Type
1	Matrix	13 ±2,5	15,6 ±1,1	58,6 ±1,8	8,3 ±0,8	1,8 ±0,7	0,6 ±0,4	0,4 ±0,4	1,2 ±0,4	
2	Average in finer carbide	23,1 ±4	22,1 ±2,3	41,6 ±5,3	3,5 ±1,6	6,3 ±1,9	3,4 ±0,8	0 ±0,2	0	M₂C complex-regular [34]
3	Finer carbide: lighter part	28,1 ±1,4	22,2 ±1,7	35,6 ±0,7	2,26 ±0,4	8,4 ±0,4	3,3 ±0,4	0,1 ±0,2	0	M₂C
4	Eutectic isles in the matrix	23,0 ±3,0	22,6 ±1,4	42,1 ±2,4	2,5 ±1,1	6,5 ±1,3	3,2 ±0,6	0,01 ±0	0	Open M₂C

4.4.2.3 DT3

This subchapter describes the microstructure of the W27 sample after thermal cycle up to 1500 °C at a rate of 1 °C/min. In this case, the sample remained for longer time at elevated temperatures than sample DT1.

Similarly to the previous cases, the overview of the sample was obtained by optical microscopy [Figure 4-57]. Porosities are larger than in the other samples. Figure 4-58a displays a dendritic solidification, as normally expected at slow cooling rates (see section 2.4). Figure 4-58b shows groups of dendrites two different shades: this effect is owed to the different dendrites orientations. In Figure 4-58c and d shows the morphology of the carbides between the dendrites: a better observation was performed with SEM microscope in BSE mode.

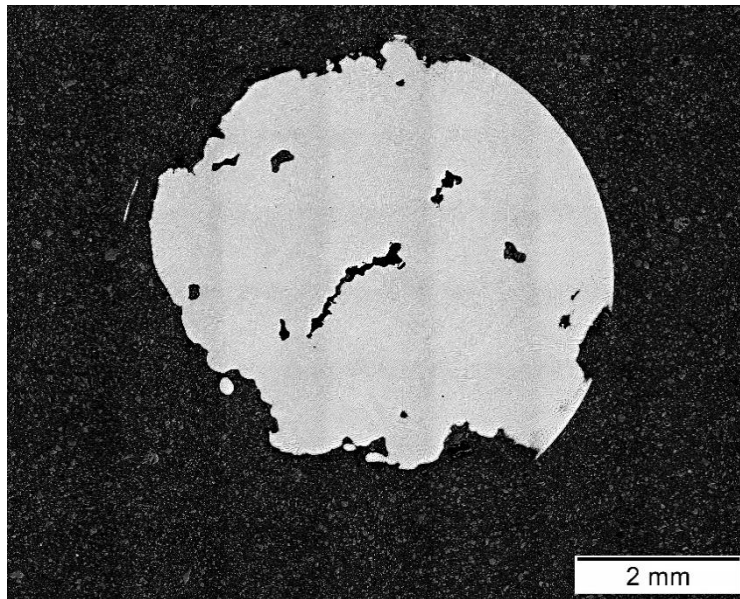
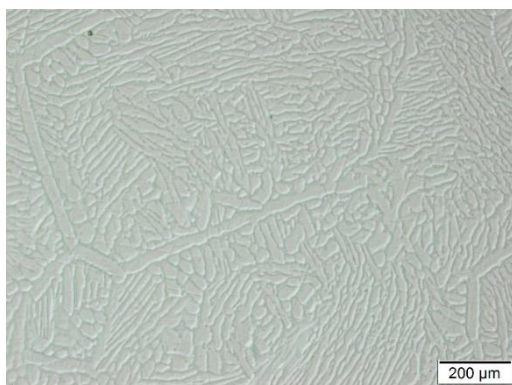
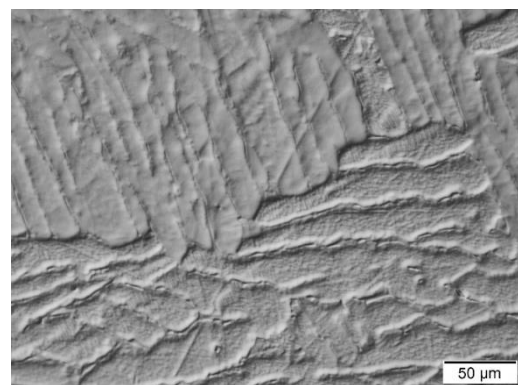


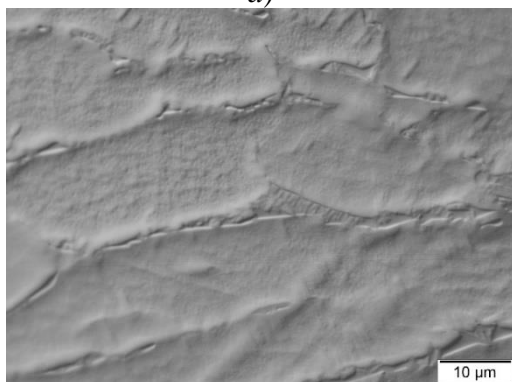
Figure 4-57: Overview of sample DT3.



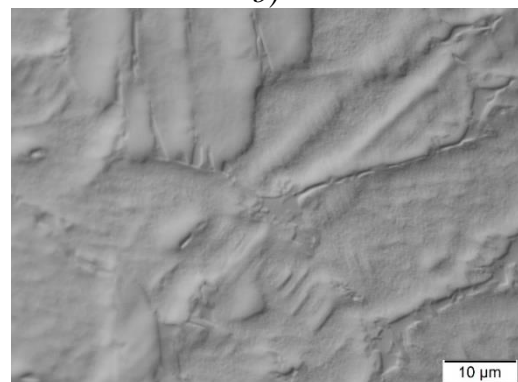
a)



b)



c)



d)

Figure 4-58: Optical images, sample DT3. a) 100x. b) 200x. c) 500x. d) 500x.

SEM analyses revealed that a discontinuous network of carbides around the dendrites forms. The morphology reveals that these are eutectic carbides. Figure 4-59 shows different magnifications of the same area of the sample. In particular, Figure 4-59c and d shows light carbides and dark carbides

that are formed around the lighter ones. The matrix presents some darker areas in the vicinity of the lighter carbides, as shown in Figure 4-60. The results of EDS analysis on these areas are presented in Table 4-25 and Table 4-26 (referring to Figure 4-59).

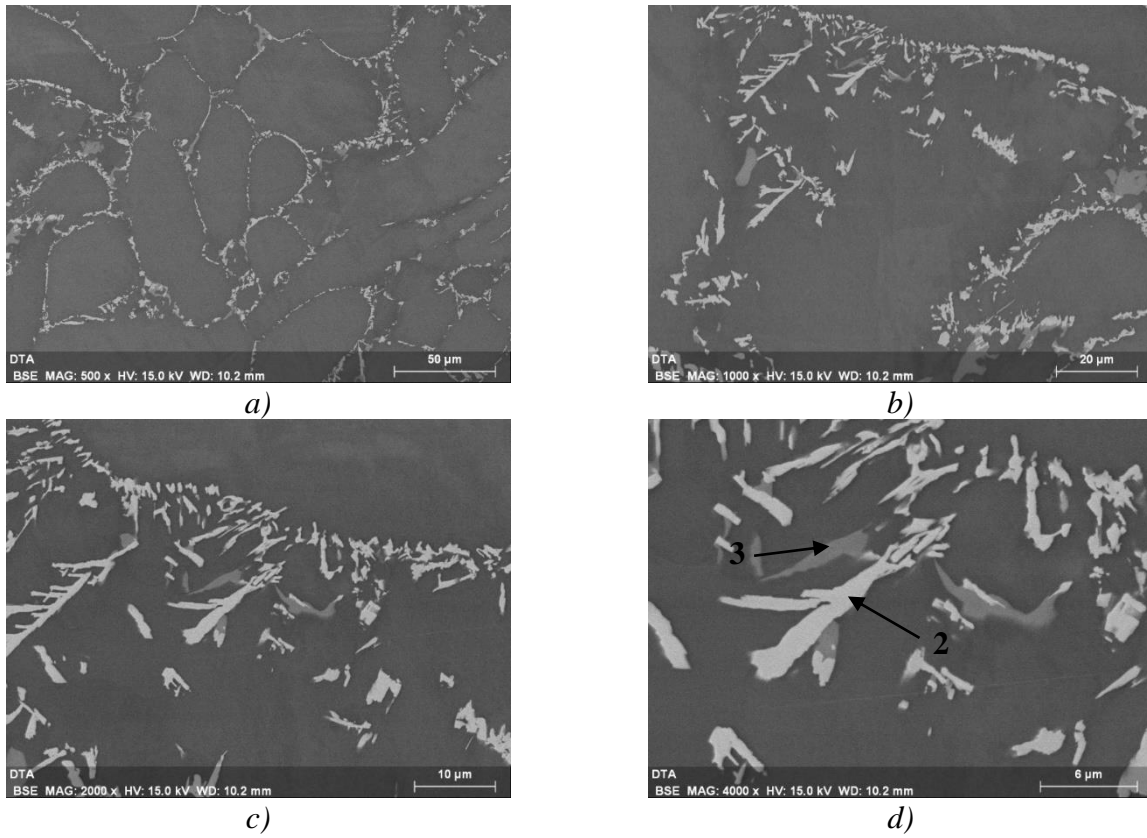


Figure 4-59: SEM-BSE images, sample DT3. a) 200x. b) 800x. c) 1600x. d) 3200x.

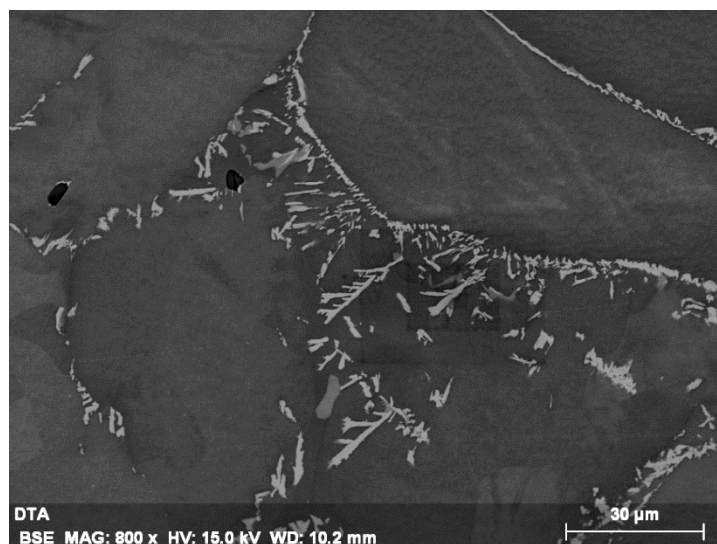


Figure 4-60: Darker areas in the vicinity of lighter carbides. Sample DT3.

Table 4-25: Compositions in wt% and relative deviation standard values. Sample DT3.

Position in Figure 4-59	wt%	C	Cr	Fe	Ni	W	Mo	Si
1	Matrix	2,4±0,9	16,4±1	69,4±1,5	8,4±0,9	2,1±1,6	0,9±0,4	0,3±0,1
2	White carbide	3,6±0,4	11,2±0,6	31,5±1,4	1,4±0,9	45,9±3,9	6,5±1,46	0±0,1
3	Grey carbide	3,5±0,8	21,3±1,6	48,8±2,2	2,1±0,7	17,3±4	6,9±1,1	0,1±0,1

Table 4-26: Compositions in at% and relative deviation standard values. Sample DT3.

Position in Figure 4-59	at%	C	Cr	Fe	Ni	W	Mo	Si	Type
1	Matrix	10,4 ±3,5	16,3 ±1,1	64,2 ±2,4	7,4 ±1	0,6 ±0,4	0,5 ±0,2	0,5 ±0,2	
2	White carbide	21,3 ±1,9	15,0 ±1,7	39,6 ±1,3	1,6 ±1,07	17,6 ±2	4,7 ±1,0	0,1 ±0,3	Eutectic M ₂ C irregular [34]
3	Grey carbide	16,4 ±3,1	23,0 ±1,4	49,2 ±1,8	2,0 ±0,8	5,4 ±1,48	4 ±0,6	0,1 ±0,35	Not identified

4.5 Nano-hardness tests

A grid of fifteen nanoindentation was performed in the zone between the particle and the matrix. Three rows per five columns is the shape of the grid. Of the fifteen nanoindentation, two have not touched the sample. Figure 4-61 shows three images of the surface after indentation. Figure 4-61 shows that the three rows are placed at different distances from the particle. Three of the fifteen indentations were chosen to analyze the hardness evolution, because the other are too close to each other and their values could be perturbed. The three chosen indents are indicated in Figure 4-61a. The closest to the particle (1), corresponds to the first layer of diffusion between matrix and particle [Figure 4-61c]. Then, the one in the middle row (2) correspond to an eutectic carbide [Figure 4-61d]. Finally, the furthest from the particle corresponds to the matrix. Table 4-27 collects the data from the triboindenter for these three indentations.

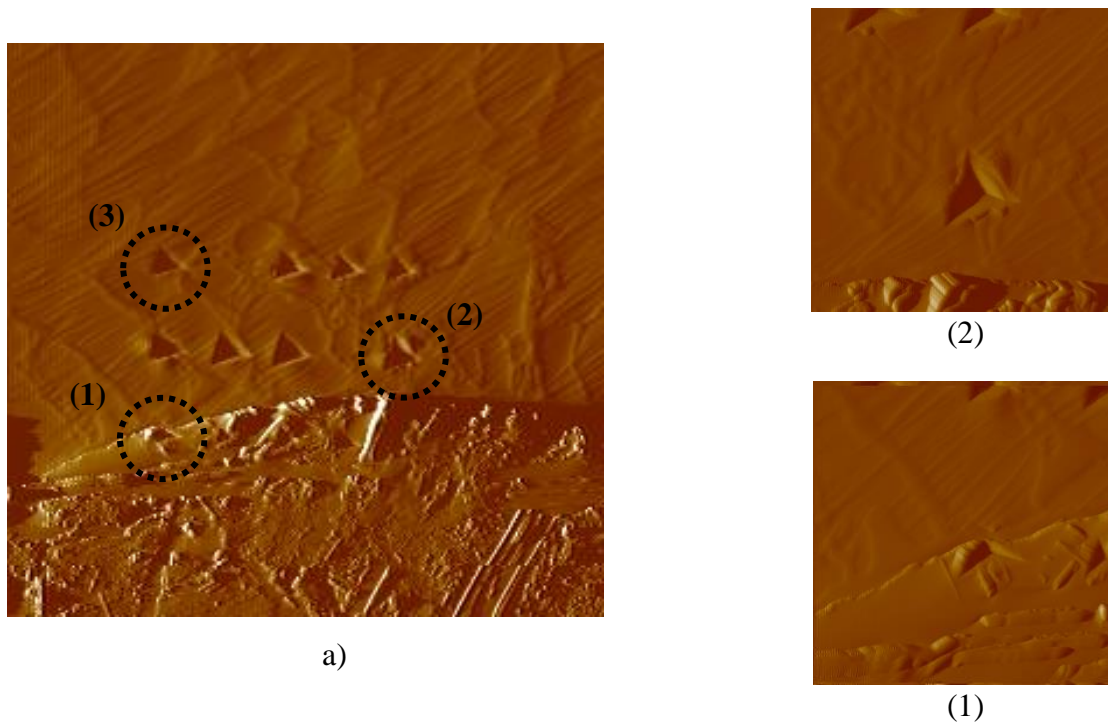


Figure 4-61: Scansions of the surface of the sample after nano-indentation. a) Analyzed indents. (1) Indent in the carbide around the particle (M_2C primary). (2) Indent in an eutectic carbide (M_6C or M_7C_3).

Table 4-27: Values measured by the nano-indenter.

Nano-indent	$P_{max}(\mu N)$	$S(\mu N/nm)$	$A(nm^2)$	$h_{max}(nm)$	$E_r(GPa)$	$H(GPa)$	Drift(nm/s)
(1)	33551,8	395,8	1365259,3	300,6	300,12	24,58	0,17
(2)	20612,3	412,9	1702190,25	301,4	280,44	12,11	-0,22
(3)	14311,9	376,3	1806097,4	301,2	248,09	7,92	-0,17

5 Discussion

This chapter discusses the results obtained and presented in the previous chapter. In particular, the particles distributions in the deposit are evaluated and correlated to the cladding process. The phases identification is discussed with the information from microstructural and thermal tests. The various microstructures obtained with different cooling rates are compared. Finally, nano-hardness results are compared with literature data.

5.1 Particles distribution

This subchapter discusses the positions and the amount of dissolution (based on cross-section measurement) of the particles in the deposit.

5.1.1 Distribution and particles surface quantification along y axis (building direction)

Two scales of observation have been taken into account (see section 4.2.1.1).

- Considering the scale of a single clad layer with a thickness of 700 μm . There is a periodicity in the particles distribution within one single clad layer. The particles have been counted using boxes with thickness 100 μm . In sample W27, a greater number of particles is observed [Figure 4-8] every three to five boxes, therefore every 300 μm to 500 μm a particles accumulation is observed. W27 sample measurement cannot be associated to the clad layer thickness. By contrast, samples W43, W53 and W62 [Figure 4-9 to 4-11] show a greater number of particles every five to eight boxes, therefore every 500 μm to 800 μm a particles accumulation is observed. For samples W43, W53 and W62 the accumulation corresponds to the clad layer thickness: 700 μm . A higher fraction of particles is measured at the base of the layer. Heavy WC particles may have fallen to the bottom of the melt pool while the metallic matrix was in the liquid state due to gravity.
- Considering the scale of the deposits. Within each deposit, a quantification of the particles cross-sectional area, for each box 100 μm thick, was carried out [Figure 4-16 to 4-19]. There is an overall variation in particles surface distribution. Sample W27 [Figure 4-16] shows a low fraction of particle surface in the middle part of the deposit, while in the base and in the top of the sample a high surface fraction of particles is observed. The explanation for this

distribution is owed to the cladding process. At first, when the first few layers are deposited, the deposit is still relatively cold because of the high heat flow rate through the substrate. Hence, the solidification occurs fast and the dissolution rate of the particles remains low. Then, when depositing the following layers, the heat from the laser causes the remelting of the previous layers (commonly the height of the melt pool is 2 to 3 times the layer thickness) [33]. Therefore, the dissolution of the original WC particles may resume while the matrix remelts. Moreover, heat accumulates gradually while additional layers are deposited and the original WC particles dissolution rate increases with the height of the build. At the top, the last few layers are submitted to less remelting cycles. The very last layer undergoes no remelting cycles. The dissolution in the last few layers is less pronounced compared to the layers underneath where dissolution is higher due to the higher thermal energy and the greater number of remelting cycles. Samples W43 and W53 [Figure 4-17 and 4-18] show the same particles surface distribution as W27. Sample W62 [Figure 4-19] does not show the same distribution owing to its different shape if compared to the other samples [Figure 4-7].

5.1.2 Distribution along x axis

All four distributions along x axis [Figure 4-12 to 4-15] present the same pattern (see section 4.2.1.1). As explained in the results part, accumulations of particles on the edges of the samples are observed. This remains to be explained. This is the first time that such an effect is reported to our knowledge, as particles distribution in laser clad metal matrix composites has received very little attention so far.

5.2 Microstructures of clad deposits: phase identification

5.2.1 Possible phases according to SE + EDS + EBSD

The identification of the carbide types present in each zone can be sometimes challenging. Data from EBSD analyses, EDS analyses and morphology of the phases must be compared. Table 5-1 shows the composition from EDS analyses in atomic percent of all the regions of the clad sample. Figure 4-31 and 4-34 show the EBSD analysis performed (see section 4.2.1.3) and Figure 4-26 to 4-29 show the morphologies observed (see section 4.2.1.3).

The phase identification will be explained starting from the original WC particle and moving towards the matrix, as Table 5-1 summarizes.

- Inside the original WC particle (#1 in Table 5-1) EBSD analyses revealed the presence of Qusongite (WC) and W_2C carbide (see section 2.3.2). This is in agreement with the data provided by Höganäs AB company and the EDS measurements (see section 3.1.2).
- In the dissolution zone (#2, 3, 4 and 6 in Table 5-1) M_4C carbide and $M_{23}C_6$ have been detected by the EBSD analyses. Investigations in literature revealed that M_4C is a carbide of common formation in the quaternary system Fe-C-Cr-W. J. Mazumder et Al. [49] explained that M_4C carbide has been observed in the region around the ternary M_6C carbide (Fe_3W_3C). They also observed another type of carbide: $M_{12}C$, but this carbide has not been observed in the present study. F.Z. Abderrahim et Al. [50] showed that M_4C carbide is a metastable sub-carbide related to M_2C carbide. M_4C carbide, in fact, is an M_2C carbide with less carbon, which makes it unstable. These considerations came from calculations of free energy formation of the various compounds. Indeed, EDS analyses revealed that the composition reported in Table 5-1 matches the composition of a typical M_2C carbide. So, it has been considered as complex M_2C carbide type. $M_{23}C_6$ carbide type (b) has been detected by EBSD sharing the same zone with M_4C detected carbide type. These carbides types could be better identified based on additional literature research, to enrich the EBSD database.
- Morphological and EDS observations (#7, 8, 9 and 10 in Table 5-1), show that the tungsten lamellar carbide is an eutectic M_6C carbide [34]. In fact, it presents the typical fishbone morphology. The chromium lamellar carbide is an eutectic M_7C_3 carbide [36] in accordance with its relatively high Cr content. Eutectic M_6C and M_7C_3 carbides have not been detected in the zone chosen for the EBSD analyses.

- Moving away from the particle (#12, 13 and 16 in Table 5-1), EBSD analyses revealed a greater amount of $M_{23}C_6$ carbide. The position in which this carbide is revealed is between the dendrites. Hence, there is a transformation from M_4C carbide to $M_{23}C_6$ carbide when moving away from the particle, visible in Figure 4-34. The formation of complex carbides like $M_{23}C_6$ is common in this type of systems. J. Mazumder et Al. [49] observed $M_{23}C_6$ carbide, more precisely $Fe_{21}W_2C_6$ carbide.

There is an evolution of the carbide type with the distance from the original WC particle. Near the WC particle W, Cr-rich M_2C carbides type are present, with various compositions. Further away, the carbides are eutectic and of a W-rich M_6C or Cr-rich M_7C_3 type. The M_4C carbide type it is observed to be near the M_6C carbide. Further from the particles the M_4C changes composition, evolving to $M_{23}C_6$.

Table 5-1: Composition in at% of each zone in the sample with indications of the correspondent hypotized carbide type.

	<i>at%</i>	<i>C</i>	<i>Cr</i>	<i>Fe</i>	<i>W</i>	<i>Ni</i>	<i>Mo</i>	<i>Si</i>	<i>Mn</i>	<i>Type of carbide</i>
1	inside the original WC particle	51,4±4,3	0,4±0,5	0,9±0,8	46,7±3,8	0,3±0,6	0	0	0,3±0,4	MC of W
2	between original WC Particle and white carbides	32,6±2,8	8,1±0,8	26,3±1,6	30,5±1,8	2,0±0,8	0,0±0,1	0	0,4±0,6	M ₂ C of W and Cr
3	white carbides	36,9±3,4	5,4±1,7	14,5±4,0	42,0±5,1	1±1	0,0±0,1	0	0,2±0,3	M ₂ C of W and Cr
4	compounds between the white carbides and matrix	32,5±3,7	10,2±1,2	27,5±2,1	26,0±2,3	2,7±0,9	0,6±0,5	0	0,5±0,5	M ₂ C of W, Fe and Cr
5	austenite phase	13,6±1,8	14,5±0,6	57,4±1,3	5,4±1,2	7,6±1,4	0,6±0,2	0	0,8±0,4	
6	grain boundary	26,9±1,3	16,3±0,1	37,2±0,4	13,5±0,4	4,2±0,0	1,5±0,5	0	0,5±0,4	M ₂ C
7	tungsten lamellar carbide	20,0±4,0	14,0±1,1	48,6±4,4	9,8±1,8	5,9±1,1	0,9±0,4	0	0,8±0,5	M ₆ C eutectic
8	part of the W-C carbide of support	23,2±3,8	13,8±1,3	43,6±2,9	12,7±1,9	4,8±0,9	1,1±0,3	0	0,7±0,4	
9	X center of the two supports	28,1±1,6	13,7±0,7	38,4±2,8	13,8±1,1	4,2±0,7	1,5±0,1	0	0,4±0,0	
10	chromium carbide	22,5±1,8	29,3±1,5	39,5±1,9	3,4±0,8	2,9±0,5	1,0±0,2	0	1,3±0,6	M ₇ C ₃
11	darker zone near Cr carbide	14,8±5,1	16,8±1,6	59,6±5,2	2,3±0,6	5,6±1,3	0,4±0,1	0	0,5±0,2	
12	carbide between the dendrites (lighter one)	25,8±3,7	17,2±1,2	35,3±2,5	14,5±1,1	3,4±0,9	3,2±1,1	0	0,6±0,6	M ₄ C
13	carbide between the dendrites (darker one)	23,5±2,6	19,4±1,1	43,5±2,0	7,1±1,4	4,2±1,1	1,5±0,2	0	0,7±0,5	M ₄ C
14	austenite phase between the carbides	11,2±3,0	13,4±1,0	62,3±2,3	3,0±1,1	8,5±1,0	0,5±0,2	0,2±0,4	0,9±0,5	
15	austenite phase far from the particle (along the dendrite)	15,0±2,4	13,1±1,0	59,6±2,0	2,4±0,8	8,0±0,9	0,6±0,2	0,2±0,3	1,1±0,4	
16	carbides between dendrites far 50 µm from the particle	18,1±2,1	20,6±0,7	47,2±2,0	6,5±0,7	4,9±0,9	1,8±0,2	0	1,0±0,2	M ₄ C/M ₂₃ C ₆

5.2.2 DTA heating curves

In this subchapter, DTA analyses results (see sections 4.4.1.2.1 and 4.4.1.3.1) will be compared with the discussion in the previous section, regarding electronic microscopy analyses (see section 5.2.1).

The two heating curves displayed in Figure 5-1 correspond to two different heating rates: DT3 test and curve correspond to a rate of 1 °C/min, DT1 test and curve correspond to a rate of 5 °C/min. Since the heating curves start from the same microstructure, they can be considered together. First, the DT1 test was performed, but the peaks could not be linked to all the zones found in the microstructure. In fact, the peaks could not be well distinguished since they were overlapped and they

formed one unique complex peak, which is difficult to consider. Consequently, DT3 was performed in order to achieve a better understanding of the meaning of the peaks.

Figure 5-1 shows the interpretations that have been given to each peak. The solidification/melting range is shown to be between 1240 °C and 1500 °C, in accordance with the Thermo-calc simulations (see section 4.4). Peaks of secondary carbides are displayed at temperatures below the solidification/melting range, meanwhile peaks related to eutectic carbides and primary carbides are displayed at temperatures in the solidification/melting range.

- At lower temperatures (below the solidification/melting range), the precipitation and dissolution of secondary carbides have been considered. The dissolution of the secondary carbides is confirmed by the DSC analysis performed [Figure 4-47]. By contrast, the secondary carbides have not been observed in the microstructural observations of the clad sample. Moreover, Figure 5-1 displays three distinct peaks: one at 600 °C, 800 °C and the other at 1100 °C, thus the dissolution of three different types of secondary carbides occurs. Probably, the secondary carbides are precipitated in zones not considered in this work.
- At the temperature of 1360 °C, the dissolution of the eutectic interdendritic carbides occurs. This carbides type show a large variability of composition (#12, 13 and 16). In fact, the relative peaks are large. The interdendritic carbides form a continuous network around the austenite phase.
- At the temperature of 1394 °C and at 1406 °C in DT3 (in the solidification/melting range) the dissolution of eutectic Cr-rich M_7C_3 carbides type, shown in Figure 4-28, has been considered. The composition of this carbide is reported in Table 5-1 (#10). Its morphology is very fine, barely visible with SEM observations and it occupies the spaces between W-rich M_6C carbides. Thus, it dissolves before the eutectic W-rich M_6C .
- The peaks observed at 1409 °C in DT1 and at 1420 °C in DT3 have been correlated to the dissolution of eutectic W-rich M_6C carbide. The morphology of this carbide is coarser than the Cr-rich M_7C_3 carbide type and its W content is higher, as reported in Figure 4-28 and Figure 5-1. The peak in the DT1 is overlapped with the peak of austenite, in DT3 this peak is distinct, but still complex.
- The peaks showed at 1415 °C and 1447 °C for DT1 and DT3 respectively, are related to the melting of the austenite phase. The peak is wide, so the melting of the austenite phase occurs in a wide range of temperatures. Probably, this is owed to the high composition variability of the matrix, because of the diffusion process that occurs between the original WC particles and

the SS316L matrix. The melting point of austenite is higher for the test at slower rate, but the motivation still is unknown.

- The last peak corresponds to the fusion of the W-rich M_2C formed by the dissolution of the particles. The peak of the melting of the original WC particles is not present because they undergo a total dissolution in the matrix before melting (section 4.4.2.1 shows an enlarged dissolution zone around the original WC particle). Hence, the original WC particles transform to M_2C carbide. If the original WC particles would have been submitted to the same thermal cycle but without being in contact with the steel, they would not have been melted. In this case, they have been completely dissolved in the steel, as reported also by Chun-Ming Lin [51]. The complete dissolution can be seen in Figure 4-53, that correspond to the DT1 test, and Figure 4-57, that correspond to the DT3 test. These two figures do not present particles anymore. Thus, when heating the microstructure presented in Figure 4-23, the particle itself will not produce any DTA signal, because it is completely dissolved in the steel to form the carbide M_2C around it.

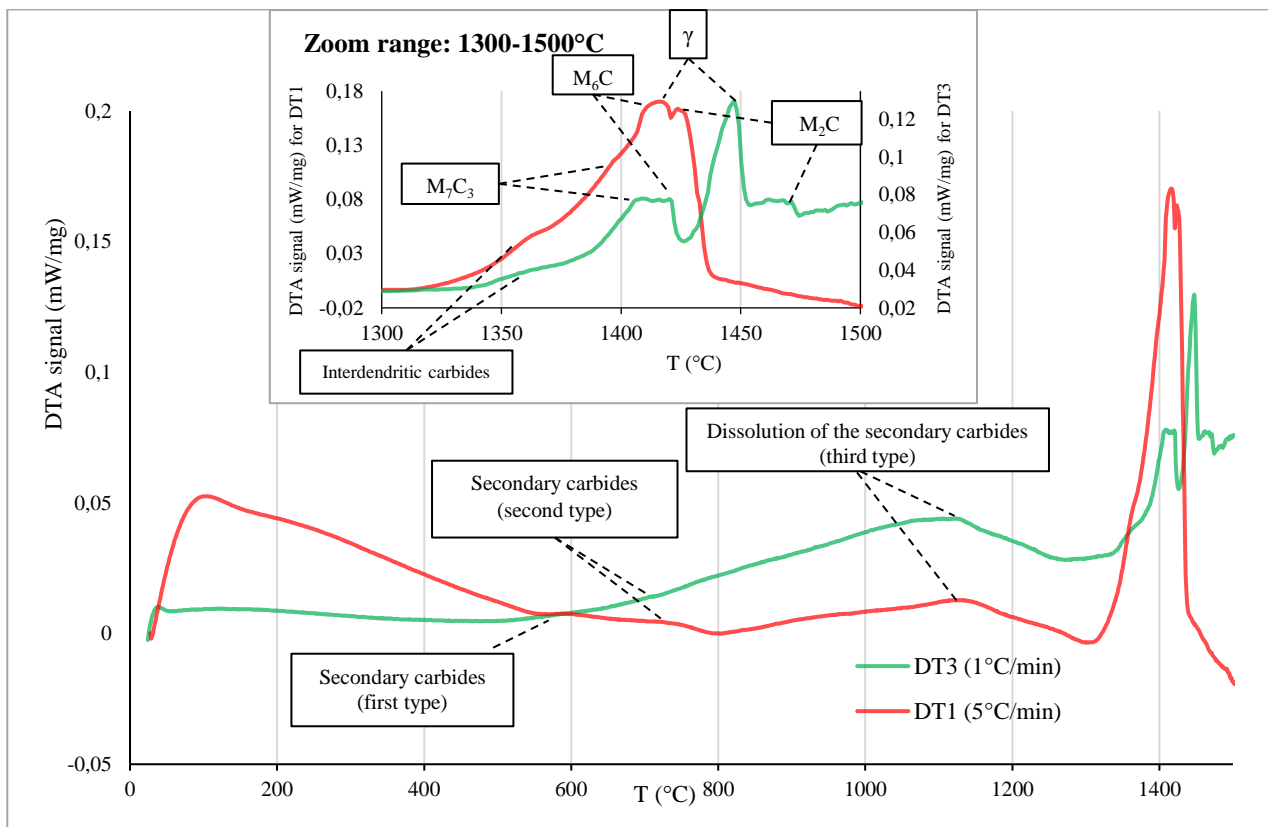


Figure 5-1: Complete DTA heating tests (DT1 and DT3) with the possible peaks explanation.

5.3 Solidification schemes as a function of cooling rate

This subchapter presents the solidification schemes as a function of the cooling rate, from the slow cooling rates (DT3 – 1 °C/min and DT1 – 5 °C/min), to the fast cooling rate (clad sample – hypotized).

5.3.1 Slow cooling rate

Figure 5-2 presents the cooling curve of DT3 test at the rate of 1 °C/min. The microstructure related to this test is presented in Figure 4-59. Each peak can be associated to the presence of a phase in the corresponding microstructure. The peaks will be explained from high to low temperature, as the cooling process occurs.

- At the temperature of 1445 °C, there is the formation of austenite from the liquid. The formation of δ -ferrite has not been related to this peak because of the high carbon content, in respect to the carbon content needed to stabilize the δ -ferrite. Moreover, δ -ferrite has not been observed in the microstructure. The part of the peak at high temperatures is related to the nucleation process of the austenite phase, and it shows that the nucleation occurs in a very small range of temperature. On the other hand, the part of the peak at lower temperature gives information on the growth process of the austenite, and this part of the peak includes a wide range of temperatures. Hence, the composition variability of the austenite phase is high. Indeed, Figure 4-60, obtained by SEM with the BSE detector, presents dark areas in the austenite phase around the carbides.
- The second peak is at the temperature of 1345 °C. This peak is probably provoked by the formation of the eutectic W-rich M_2C irregular carbides. Table 4-26 presents a W-rich composition for this carbide type, thus its formation occurs before the formation of the Cr-rich grey carbide observed in the microstructures [Figure 4-59]. The rate of the reaction for the formation of eutectic M_2C irregular carbides is high. In fact, as it is an eutectic structure, the whole formation occurs in a range of 5 °C and the composition variability is small. Boccalini et al. [34] have observed that this carbide is promoted by low cooling rates, as has been observed in this case study.
- At temperatures below the solidification range (1240 °C-1500 °C), precisely between 980 °C and 1192 °C, the precipitation of secondary carbides takes place. Secondary carbides have not been observed in the microstructure. Further microstructural investigation is needed to reveal the secondary carbides, probably an etching could help.

The grey carbides [Figure 4-59d] present in the microstructure could not be linked to any peak. This carbide type is still unknown, but it contains a high percentage of Cr if compared to the matrix and the M_2C regular carbide type. Thus, this carbide could be related to an M_7C_3 carbide type. Otherwise the morphology is different from what found in literature (see section 2.5).

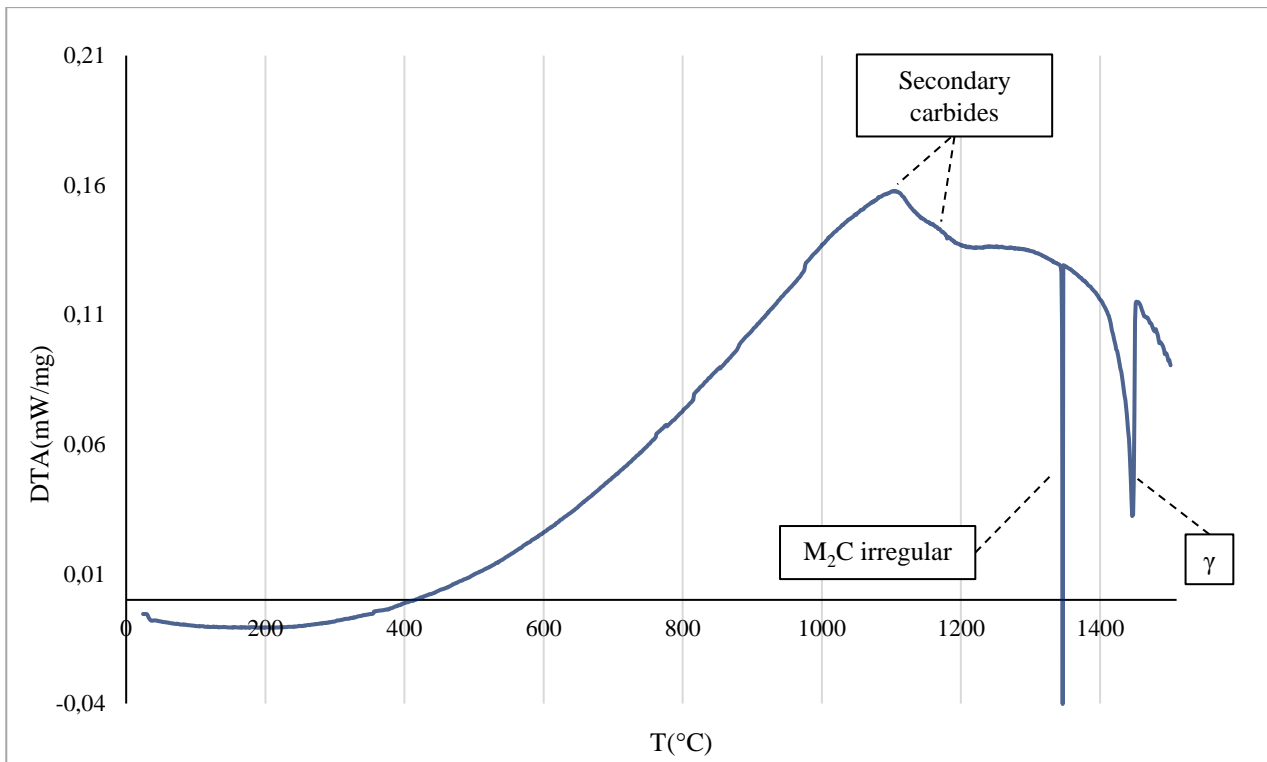


Figure 5-2: DTA cooling test (DT3) with the possible peaks explanation.

The comparison between DT3 test at the rate of 1 °C/min and the DT1 test and 5 °C/min will be discussed below.

Figure 5-3 presents the cooling curve for DT1 test at a rate of 5 °C/min. Figure 4-55 shows the microstructure related to the explanation of this curve.

- At a temperature of 1417 °C, the austenite phase nucleates from the melt. The formation of δ -ferrite has not been considered possible. As discussed for DT3 test, carbon content is too high and in the final microstructure markings of peritectic transformations have not been observed. The shape of this peak is similar to the shape of the peak linked to the formation of the austenite described for DT3 test. A great composition variability of the matrix is also observed in the microstructure obtained after the DT1 test [Figure 4-55a].

- At 1341 °C the formation of the carbide called eutectic open M_2C occurs. This carbide was not observed in the DT3 (1 °C/min) test microstructure. The eutectic open M_2C carbide has been considered to form at higher temperatures than the finer complex-regular M_2C .
- At 1245 °C the formation of the carbide called complex-regular M_2C carbide occurs. In fact, this carbide develops forming a peripheric layer around the open M_2C carbide [Figure 5-4a]. Probably, the formation of the eutectic open M_2C carbide occurs first, changing the composition of the surrounding liquid phase. After reaching a certain composition, the formation of the complex-regular M_2C carbide can take place. The retarded formation of the complex-regular M_2C carbide is confirmed by the presence of shrinkage cavities in this carbide type [Figure 5-4b]. Boccalini et al. [34] studied the complex-regular M_2C carbide and stated that its formation is promoted by high cooling rates or low vanadium contents. The material analyzed in this study contains no vanadium and the cooling rate is higher than in DT3 test.
- At temperatures below 1240 °C, precisely between 742 °C and 977 °C the precipitation of secondary carbides occurs. These carbides have been observed only in optical micrographs after prolonged OPS polishing (10 min). The composition of these carbides has not been measured.

From the DT3 to the DT1 microstructures the difference is high, despite the small difference in cooling rate. The carbides observed in each microstructure are M_2C types, but the morphology is completely different. In fact, the cooling rate strongly affects the morphology of the carbides [34].

The comparison of the formation/precipitation temperatures of the common phase in each test can be useful. Austenite phase in DT3 test (1 °C/min) forms at 1445 °C, meanwhile in DT1 test (5 °C/min), it forms at 1417 °C. Secondary carbides in DT3 test (1 °C/min) form between 980 °C and 1192 °C, while in DT1 test (5 °C/min), they form between 742 °C and 977 °C. The formation temperature of both the austenite phase and the secondary carbides is lower when the cooling rate is high. In fact, the faster cooling rates present a lower constitutional undercooling than slower cooling rates [15]. Constitutional undercooling basically is the difference between the real temperature of the melt and the temperature shown in equilibrium condition for a certain composition. Moreover, when constitutional undercooling is higher, dendrites are more easily formed (see section 2.4).

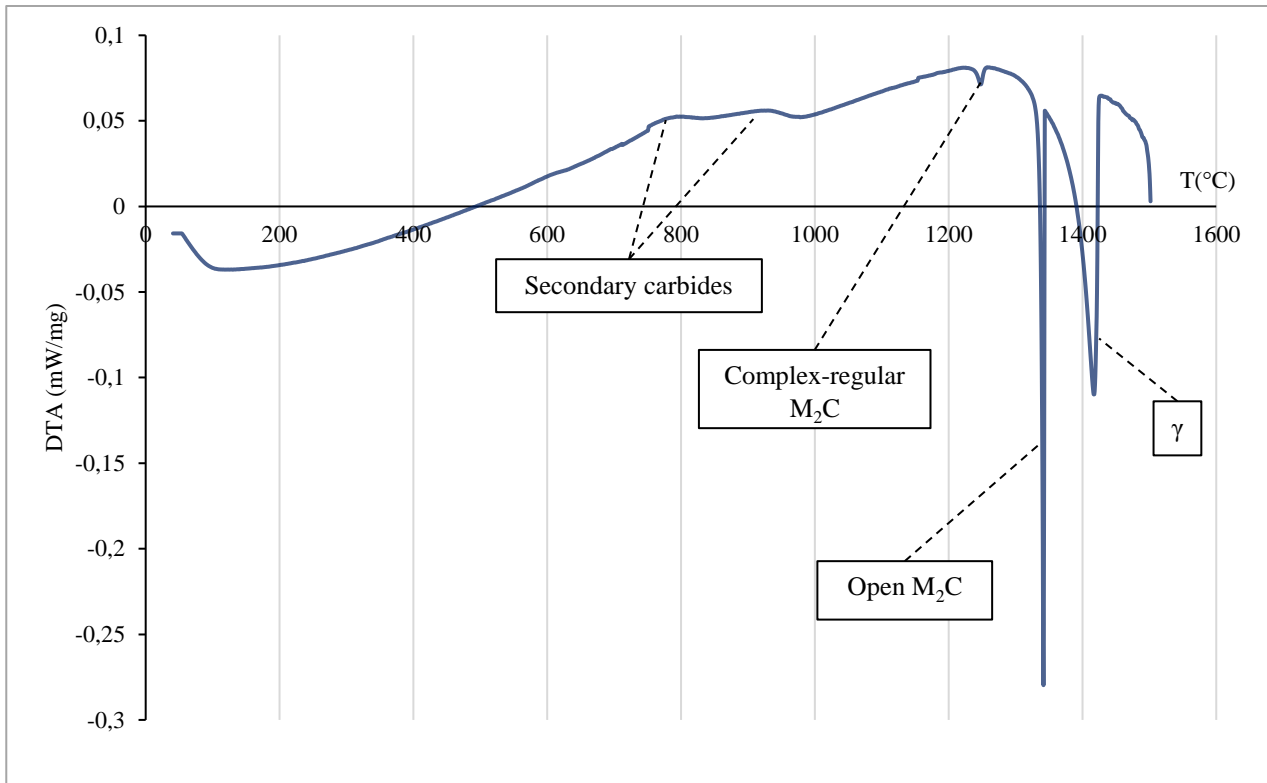


Figure 5-3: DTA cooling test (DTI) with the possible peaks explanation.

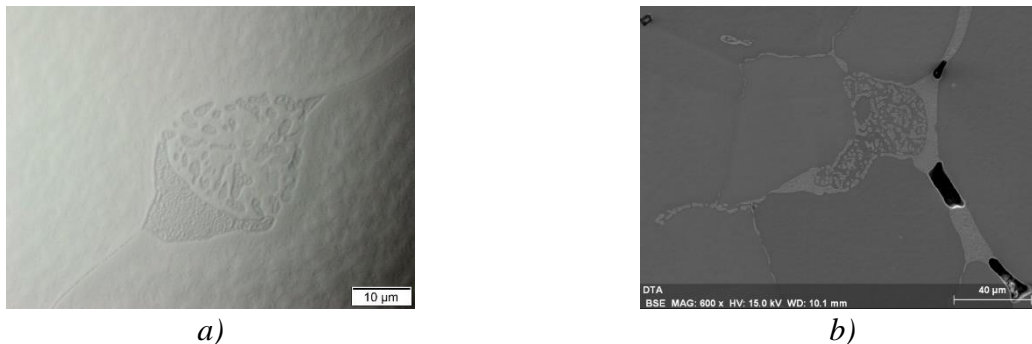


Figure 5-4: a) Optical image representing the open M₂C carbide surrounded by the finer carbide. 1000x. b) SEM image showing the presence of cavities. 600x.

5.3.2 Hypothetical solidification of the laser clad deposit (high cooling rates)

Combining SEM observations, DTA analyses results and literature (see section 2.4) a possible solidification scheme may be proposed for the clad deposit. Figure 5-6 presents a schematization of the deposition process, with indications of the heat extraction from the melt pool. The numbers in the following paragraph are linked to Figure 5-7 that shows a schematization of the clad microstructure.

The solidification proceeds from two different zones in the clad deposit: (1) around the particle and (2) around the melt pool. Together these zones are related to contact surface between solid and melt. The first zone (1) represents the contact between the solid WC particle and the molten SS316L. WC particles act as inoculants for the solidification process. The second zone (2) represents the contact between the melt pool of SS316L generated by the heat of the laser and the solid substrate or previous layers. These two zones are considered as solidification fronts.

- Firstly, zone A [Figure 4-26], where the formation of the reaction crown by the dissolution of the original WC particles in the molten steel occurs. M_2C primary carbides [Table 5-1] are formed in this zone. The first zone near the particle presents less W in comparison to the white carbides described in subchapter 4.2.1.3, Zone A. The zone between the white carbides and the matrix has a similar composition to the closest zone to the WC particle. The solidification could have happened in two different ways: (a) the solidification starts directly from the particle surface, forming the first zone near the particle. W accumulates in the liquid around this zone and then forms the white carbides richer in W [Figure 5-5a]. Another way (b) to explain the different composition of these zones considers that the white carbides are actually part of the particle. The liquid could penetrate along cracks or grain boundaries [Figure 4-2], leaving the external part of the particle but solubilizing the inner part [Figure 5-5b].

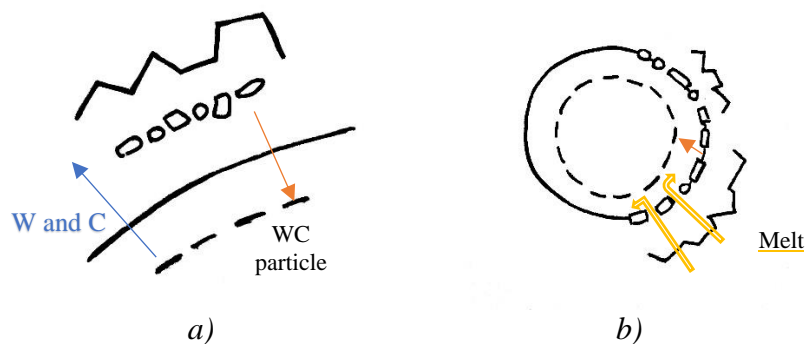


Figure 5-5: Possible WC particles dissolution processes. a) First way of dissolution. Blue arrow indicates the diffusion direction of W and C, orange arrow indicates the reduction in size of the WC particle. b) Second way of dissolution. Yellow arrows indicate the liquid penetration, orange arrow indicates the reduction in size of the WC particle.

- Secondly, while the solidification around the particles is taking place, the other front of solidification is moving forward. The second solidification front starts from the contact with the substrate or previous layers. Dendrites grow through the matrix towards the WC particle (see section 2.4). The compositions of the austenite phase along the dendrites and of the

carbides formed between them are reported in Table 5-1. These carbides can be richer in W or in Cr. Logically, the closer to the particle they are, the more W they get.

- Thirdly, looking back to the first solidification front, there is the formation of equiaxed grains. Between the grains M_2C rich in W is formed, while the matrix is austenite.
- Finally, the liquid reaches two different eutectic compositions. There is the formation of the lamellar carbide rich in W, with the classical morphology of the M_6C carbide [34] and the formation of a lamellar carbide rich in Cr. This last one is probably M_7C_3 eutectic carbide, from consideration on composition [Table 5-1] and on morphology [36]. The chromium carbides M_7C_3 eutectic are finer than the tungsten lamellar M_6C carbides. Moreover, the chromium carbides grow in the spaces between the tungsten carbides. Thus, the tungsten carbides form before the chromium carbides.

The clad microstructure shows many types of carbides in comparison with the microstructures obtained by slower cooling rates. In fact, primary carbides were not observed at the slow cooling rates [Figure 4-55 to 4-59]. In the clad microstructure, a particular carbide, formed by the dissolution of the original WC particles, was observed. It is not clear if it can be considered as primary carbide. This carbide was observed as enlarged in the microstructure after DS4 test [Figure 4-51].

The dissolution of the original WC particles in the matrix varies for different particles, as a function of their size. In fact, smaller particles are more inclined to dissolve in the matrix because the ratio between the surface and the volume of the particle is high and there is more contact between particle and matrix. The free energy of the process of dissolution of these smaller particles is more lower and the dissolution takes place easily. Nevertheless, in the microstructural observations it is not possible to state which particle is greater. Their shape is spherical and they are all cut in one of their cross-sections. So, two particles of the same size could be reported in the microstructure with different cross-sections. However, comparing two equal size cross-sections it is possible to state which cross-section belongs to a greater or to a smaller particle, observing the quantity of the dissolution.

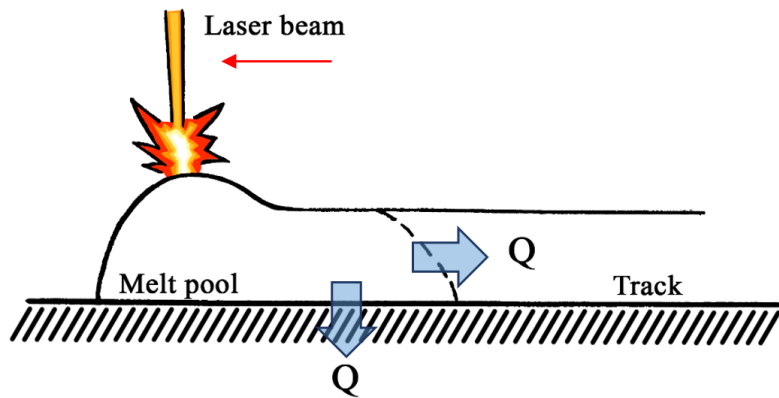


Figure 5-6: Schematization of the laser clad process with indication of the different parts.

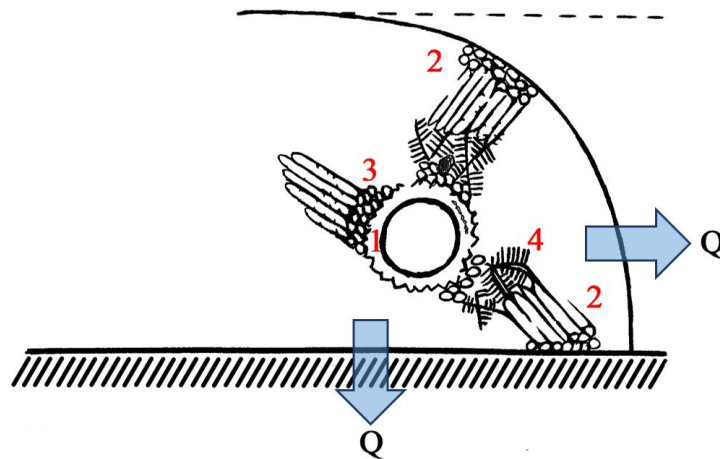


Figure 5-7: Zoom of Figure 5-6 near the solidification front with a schematization of the microstructure observed in Figure 4-23.

For any given particle, the solidification morphology varies as a function of position along the surface (i.e. at the lower or upper surface). Some zones do not present the last step of solidification described above: there is no formation of eutectic carbides. This is probably due to the displacement of the particle in the matrix through the action of gravity. In fact, while the particle falls into the molten steel, a sort of “dead zone” could be created on the top of the particle. Therefore, on the top of the particle the same molten steel stays for more time in contact with the particle. By contrast, in the lowest part of the particle always new steel is brought to the surface until it solidifies. Thus, if the contact time is greater, then the particle dissolves more [Figure 5-8].

Dissolution of the original WC particles is less pronounced with laser cladding process, due to the fast cooling rate. Hogan AB reports that the lower the dissolution of the particles, the better are the abrasive wear resistance and impact wear of the final coating (Annex C).

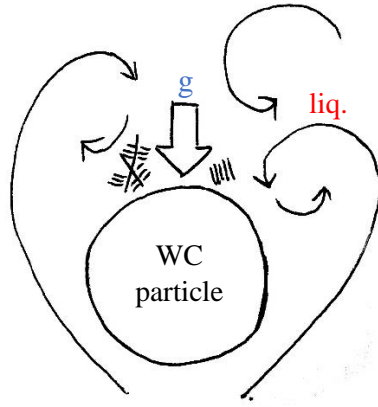


Figure 5-8: Displacement of one particle in the melt pool.

Nano-hardness considerations

Three points of analysis were taken in three different zones of the sample. Hardness measurement is reported in GPa, so there is the need to a conversion in Vickers (HV): most common measure unit for hardness. Then, hardness in GPa must be divided by a conversion factor of 0,009807 to obtain HV [52].

The hardness values in HV are reported in Table 5-2. The first (1) indentation was carried out closer to the particle than the other two indents (see section 4.2.1.3, Zone A). In fact, the first indentation presents a higher hardness. Hardness value provided by CES Edupack [17] for WC is between 3100 and 3600 HV. Hardness value in HV of indent (1) is 2508HV. Hardness value in zone (1) does not differ so much from the hardness value of WC by CES Edupack. Moreover, hardness value for the first indentation is way greater than the other two presented in the table below. In fact, the composition of zone (1) is very rich in W [Table 4-4, 4-5]. The second indentation (2) was measured in correspondence with an eutectic carbide (see section 4.2.1.3, Zone C). The measured hardness is 1235HV, while the hardness value reported by Boccalini et al. [34] for an M_6C carbide is 1500HV. The measured hardness is a bit lower than the reported one and this is possibly owed to the presence of the M_7C_3 carbide near the M_6C . The test, in fact could have indented also a part of the M_7C_3 carbide, whose hardness value is not reported. The second (2) indent shows a higher hardness than the third (3) indentation; measured in the matrix.

Together the three indentations shows higher hardness values than that of the steel from CES Edupack [17]. This can be explained taking in account the different cooling rates to which the steels were submitted. In fact, the condition of the SS316L considered in CES Edupack is “fully annealed”, thus presents a lower value of hardness.

Other values from the nano-hardness test were reported in Table 5-2. The maximum stress (μN) needed to obtain the maximum displacement (h_{max}) decreases from indentation (1) to indentation (3), meanwhile the surface of the nano-indentation increases.

Table 5-2: Output values of the nano-indenter, with the addition of the hardness values converted in HV.

<i>Nanoindentation</i>	<i>Pmax(μN)</i>	<i>S($\mu\text{N}/\text{nm}$)</i>	<i>A(nm^2)</i>	<i>hmax(nm)</i>	<i>Er(GPa)</i>	<i>H(GPa)</i>	<i>H(HV)</i>	<i>Drift(nm/s)</i>
(1)	33551,8	395,8	1365259,3	300,6	300,12	24,58	2508	0,17
(2)	20612,3	412,9	1702190,25	301,4	280,44	12,11	1235,7	-0,22
(3)	14311,9	376,3	1806097,4	301,2	248,09	7,92	808,1	-0,17

6 Conclusions and future prospects

The results obtained during the project and their interpretation will be summarized in this section. Moreover, some suggestions will be provided to overcome the problems encountered.

The main objective of this project was the study of the microstructure of a coating built by laser cladding. The material analyzed is an austenitic stainless-steel 316L-particulate tungsten carbide, metal-matrix composite.

The first part of this project was the examination of powders with SEM (SE and EDS) analysis. A granulometry test on the WC powder was also performed. Composition, particles surface and particles size are in agreement with the datasheets (Annex A, B) [42, 43].

The microstructural characterization was performed on the laser clad SS316L+WC MMC coating, with optical and SEM (SE, BSE, EDS, EBSD) analysis.

Optical observations on particles distribution and surface distribution were performed for samples W27, W43, W53 and W62, along the building direction. In each single deposit has been observed an accumulation of particles on the edge of each clad layer, due to a particles displacement driven by gravity. Moreover, a low fraction of particle surface was observed in the middle part of the deposit. This is linked to the different particle dissolution with different distances from the substrate, due to a different heat accumulation during cladding (see section 5.1.1).

SEM observations were carried out on sample W43. The matrix presents a very fine dendritic microstructure, with different orientation growth (SE and EBSD-IPF x). Between the matrix and the original WC particles a reaction occurs during laser cladding process. This reaction produces the partial dissolution of the WC particle in the matrix with the formation of reaction carbides. W-rich M_2C carbide, W-rich eutectic M_6C carbides, Cr-rich eutectic M_7C_3 carbide, M_4C carbide [50] and $M_{23}C_6$ carbide [Table 5-1] were recognized through a confrontation between EDS (composition), SE (morphological) and EBSD (lattice) data. In addition, it would be useful to correlate with higher precision the lattice type with the composition of each sample. For this reason, further EBSD analyses are suggested in zones of the sample where eutectic carbides are present. Moreover, further research to index the compounds and constituent should be carried out. The carbides observed are very small, hence it is suggested to perform TEM analysis.

The thermal analyses performed are summarized in Table 3-8. The tests revealed that the original WC particles dissolved completely in the steel when reaching high test temperatures. Dissolution starts from a temperature below 1200 °C, as proven by the DS4 test (see section 4.4.2.1), with a visible enlargement of the circular crown of reaction carbides around the original WC particles. The tests DT3 (1 °C/min) and DT1 (5 °C/min) had been compared each other and with their microstructures. The carbides morphology was completely different.

A solidification sequence was theorized in order to better understand the additive manufacturing of composite samples. The solidification fronts are two: (a) particles-melt pool interface, (b) melt pool-substrate interface. First, formation of the M_2C carbide for solubilization of the original WC particle in the molten steel. Meanwhile, in the (b) solidification front, start the formation of equiaxed grains and then dendrites, growing in the direction of the particles. In the (a) solidification front the formation of equiaxed zone and eutectic reaction carbides (M_6C and M_7C_3) occurs. The eutectic reaction carbides were not observed around every particle.

The dissolution of the original WC particles in the matrix was correlated to their size. Further thermal analyses up to different temperatures are suggested in order to better understand how much the temperature affects the particles dissolution.

Nano-hardness tests [Table 5-2] revealed that the SS316L+WC MMC produced by laser cladding show a hardness evolution between the steel and the WC. Hardness values were measured in the dissolution zone of the original WC particle (see section 4.2.1.3, Zone A), in an eutectic carbide (see section 4.2.1.3, Zone C) and in the matrix. The dissolution zone presents a lower hardness value than the WC particle [Table 2-6]. The eutectic carbide presents a lower hardness than the M_6C carbide (see section 2.5), due to the different eutectic carbides present in the sample. Finally, the matrix presents a higher hardness value than the one presented in section 2.3.2, due to the fast cooling rate of the laser cladding process. Moreover, it would be of great practical utility to verify the wear resistance of this deposit, e. g. with a pin-on-disk test. The formation of carbides enhances the hardness and probably the wear resistance, but can cause segregations in the material. Therefore, corrosion resistance tests are also suggested.

7 References

- [1] T. L’Hoest, “Réalisation de dépôts composites métal/ céramique par laser cladding”, Master Thesis, University of Liege, 2015.
- [2] A. Mertens, T. L’Hoest, J. Magnien, R. Carrus, and J. Lecomte-Beckers, “On the Elaboration of Metal-Ceramic Composite Coatings by Laser Cladding”, *Material Science Forum*, vol. 879, pp. 1288–1293, 2017.
- [3] ISO/ASTM 52900:2015(E), “Standard Terminology for Additive Manufacturing – General Principles –Terminology”, 2015.
- [4] D. Herzog, V. Seyda, E. Wycisk, and C. Emmelmann, “Additive manufacturing of metals” *Acta Mater.*, vol. 117, pp. 371–392, 2016.
- [5] W. E. Frazier, “Metal additive manufacturing: A review,” *J. Mater. Eng. Perform.*, vol. 23, no. 6, pp. 1917–1928, 2014.
- [6] Lawrence Livermore National Laboratory Website: <https://acamm.llnl.gov/am-technology/powder-bed-am> (On line 23/08/2017).
- [7] Thermal Spray depot Website: <http://www.thermalspraydepot.com/laser-cladding-services/> (On line 23/08/2017).
- [8] Sciaky Inc. Website: <http://www.sciaky.com/additive-manufacturing/wire-am-vs-powder-am> (On line 23/08/2017).
- [9] L. Santo, “Laser cladding of metals : a review”, *Int. J. Surface Science and Engineering*, vol. 2, no. 5, pp. 327–336, 2008.
- [10] E. Toyserkani, A. Khajepour, *Laser Cladding*, Book, 2005.
- [11] U. de Oliveira, V. Ocelik, and J. Th. M. De Hosson, “Analysis of coaxial laser cladding processing conditions” vol. 197, pp. 127–136, 2005.
- [12] H. Gedda, “Laser Cladding : An Experimental and Theoretical Investigation” Luleå University, 2004.
- [13] G. J. Bruck, “Fundamentals and industrial applications of high power laser beam cladding” vol. Vol. 957, 1988.
- [14] R. Vilar, “Laser cladding”, *Journal of Laser Application*, vol. 11, no. 2, 1999.
- [15] M. Dabalà. Personal lesson notes of Science and Thecnology of Metallic Materials. University of Padova, Italy, 2015-2016.
- [16] Lesson by T. Sourmail and H. K. D. H. Bhadeshia. University of Cambridge Website: https://www.phase-trans.msm.cam.ac.uk/2005/Stainless_steels/stainless.html (On line 9/08/2017).

- [17] M. Ashby, “CES EduPack.” 2016.
- [18] Q. Fang, W. Bai, J. Yang, X. Xu, G. Li, N. Shi, M. Xiong, and H. Rong, “Qusongite (wc): A new mineral” *Am. Mineral.*, vol. 94, no. 2–3, pp. 387–390, 2009.
- [19] A. I. Kurlov, Alexey S. Gusev, *Tungsten carbides. Structures, properties and application in hard metals*. Book, Springer, 2013.
- [20] M. L. Griffith, M. E. Schlienger, L. D. Harwell, M. S. Oliver, M. D. Baldwin, M. T. Ensz, M. Essien, J. Brooks, C. V. Robino, J. E. Smugeresky, W. H. Hofmeister, M. J. Wert, and D. V. Nelson, “Understanding thermal behavior in the LENS process” *Mater. Des.*, vol. 20, no. 2, pp. 107–113, 1999.
- [21] V. Manvatkar, A. De, and T. DebRoy, “Spatial variation of melt pool geometry, peak temperature and solidification parameters during laser assisted additive manufacturing process,” *Mater. Sci. Technol.*, vol. 31, no. 8, pp. 924–930, 2015.
- [22] T. Durejko, M. Pola, I. Kunce, P. Tomasz, K. J. Kurzyd, and Z. Bojar, “The microstructure , mechanical properties and corrosion resistance of 316 L stainless steel fabricated using laser engineered net shaping”, *Materials Science & Engineering A*, vol. 677, pp. 1–10, 2016.
- [23] B. Song, X. Zhao, S. Li, C. Han, Q. Wei, S. Wen, J. Liu, and Y. Shi, “Differences in microstructure and properties between selective laser melting and traditional manufacturing for fabrication of metal parts: A review” *Front. Mech. Eng.*, vol. 10, no. 2, pp. 111–125, 2015.
- [24] AZO Materials website: <https://www.azom.com/article.aspx?ArticleID=12155> (On line 23/08/2017).
- [25] T. Niendorf, S. Leuders, A. Riemer, H. A. Richard, T. Tröster, and D. Schwarze, “Highly anisotropic steel processed by selective laser melting” *Metall. Mater. Trans. B Process Metall. Mater. Process. Sci.*, vol. 44, no. 4, pp. 794–796, 2013.
- [26] Y. Zhong, L. Liu, S. Wikman, D. Cui, and Z. Shen, “Intragranular cellular segregation network structure strengthening 316L stainless steel prepared by selective laser melting” *J. Nucl. Mater.*, vol. 470, pp. 170–178, 2016.
- [27] A. Mertens, S. Reginster, Q. Contrepolis, T. Dormal, O. Lemaire and J. Lecomte-Beckers, “Microstructures and Mechanical Properties of Stainless Steel AISI 316L Processed by Selective Laser Melting”, *Materials Science Forum*, vols. 783-786, pp. 898–903, 2014.
- [28] University of Cambridge Website: Lesson by H. K. D. H. Bhadeshia. <https://www.phase-trans.msm.cam.ac.uk/dendrites.html> (On line 24/08/2017).
- [29] H. J. Shin, J. K. An, S. H. Park, and D. N. Lee, “The effect of texture on ridging of ferritic stainless steel” *Acta Mater.*, vol. 51, pp. 4693–4706, 2003.
- [30] University of Cambridge Website:

- https://www.doitpoms.ac.uk/miclib/micrograph_record.php?id=617 (On line 24/08/2017).
- [31] A. F. Padilha, C. F. Tavares, and M. A. Martorano, “Delta Ferrite Formation in Austenitic Stainless Steel Castings” *Mater. Sci. Forum*, vols. 730–732, pp. 733–738, 2013.
- [32] N. Hashemi: ‘Study of High Speed Steel deposits produced by Laser cladding’, PhD Thesis, University of Liege, 2017.
- [33] M. Boccalini and H. Goldenstein, “Solidification of high speed steels” *Int. Mater. Rev.*, vol. 46, no. 2, 2001.
- [34] M. Durand-Charre, *Microstructure of Steels and Cast Irons*. Book, 2003.
- [35] J. Nurminen, J. Näkki, and P. Vuoristo, “Microstructure and properties of hard and wear resistant MMC coatings deposited by laser cladding” *Int. J. Refract. Met. Hard Mater.*, vol. 27, no. 2, pp. 472–478, 2009.
- [36] K. Wiecezrak, P. Bala, R. Dziurka, T. Tokarski, G. Cios, T. Koziel, and L. Gondek, “The effect of temperature on the evolution of eutectic carbides and $M_7C_3 \rightarrow M_{23}C_6$ carbides reaction in the rapidly solidified Fe-Cr-C alloy”, *J. Alloys Compd.*, vol. 698, pp. 673–684, 2017.
- [37] PubMed.gov Website: <https://www.ncbi.nlm.nih.gov/pmc/articles/PMC5011776/figure/f1/> (On line 24/08/2017)
- [38] F. Stein, M. Palm, and G. Sauthoff, “Structure and stability of Laves phases. Part I. Critical assessment of factors controlling Laves phase stability”, *Intermetallics*, vol. 12, no. 7–9, pp. 713–720, 2004.
- [39] A. Scheid and A. D’Oliveira, “Effect of processing on microstructure and properties of CoCrMoSi Alloy” *Mater. Res.*, vol. 16, no. 6, pp. 1325–1330, 2013.
- [40] M. Breda, “Phase Stability in Duplex Stainless Steel” PhD Thesis, Università di Padova, 2014.
- [41] A. Armadilhas and D. A. Inoxidáveis, “Some Pitfalls in Welding of Duplex Stainless Steels,” *Soldag. insp. São Paulo*, vol. 15, no. 4, pp. 336–343, 2010.
- [42] Carpenter Powder Product Website: <https://www.carttech.com/en/> (On line 28/08/2017).
- [43] Höganäs Website: <https://www.hoganas.com/> (on line 28/08/2017).
- [44] Malvern Website: <https://www.malvern.com/en/support/product-support/mastersizer-range/mastersizer-2000> (On line 24/08/2017).
- [45] Sirris Website: <http://www.sirris.be/> (On line 24/08/2017).
- [46] Be Additive Manufacturing (BeAM) Website: <http://beam-machines.fr/en/about> (On line 24/08/2017).
- [47] IREPA laser Website: <http://www.irepa-laser.com/en/additive-manufacturing> (On line 24/08/2017).
- [48] EDEN instruments Website: www.eden-instruments.com/en/nanoindentation-platforms/

(On line 24/08/2017).

- [49] J. Mazumder, O. Conde, R. Villar, and W. Steen, *Laser Processing : Surface Treatment and Film Deposition*. Book, 1996.
- [50] F. Z. Abderrahim, H. I. Faraoun, and T. Ouahrani, “Structure , bonding and stability of semi-carbides M_2C and sub-carbides M_4C (M=V, Cr, Nb, Mo, Ta, W): A first principles investigation,” *Phys. B Phys. Condens. Matter*, vol. 407, no. 18, pp. 3833–3838, 2012.
- [51] C. M. Lin, “Functional composite metal for WC-dispersed 304L stainless steel matrix composite with alloying by direct laser: Microstructure, hardness and fracture toughness,” *Vacuum*, vol. 121, pp. 96–104, 2015.
- [52] Website: <http://www.gordonengland.co.uk/hardness/hvconv.htm> (On line 24/08/2017).

8 Annexes

8.1 Annex A: Datasheet SS316L powder



Carpenter Stainless Type 316/316L

Identification

UNS Number

- S31600/S31603

Type Analysis

Single figures are nominal except where noted.

Carbon (Maximum)	0.03 %	Manganese (Maximum)	2.00 %
Phosphorus (Maximum)	0.045 %	Sulfur (Maximum)	0.030 %
Silicon (Maximum)	1.00 %	Chromium	16.00 to 18.00 %
Nickel	10.00 to 14.00 %	Molybdenum	2.00 to 3.00 %
Iron	Balance		

General Information

Description

Carpenter Stainless Type 316/316L is a low carbon version of conventional Type 316.

In this low-carbon austenitic alloy, control of carbon to a maximum of 0.03% has been shown to minimize carbide precipitation during welding. Customers have reported the use of this steel in the as-welded condition in a variety of corrosive applications.

Carpenter Stainless Type 316/316L is suggested for applications requiring a moderate level of improvement in machinability for shorter runs of less complex parts, particularly at larger bar diameters.

Manufacturers interested in realizing the potential economic benefits and lower costs associated with higher machining speeds and lower cycle times should consider Carpenter's Project 70+® Type 316/316L stainless.

Customers have reported that Project 70+® Type 316/316L stainless offers significantly improved machinability characteristics over generic Carpenter Stainless Type 316/316L. This includes up to 50% and higher machining speeds, with improved finishes and longer tool life.

Applications

Carpenter Stainless Type 316/316L should be considered for use in paper pulp handling equipment, process equipment for producing photographic chemicals, inks, rayon, rubber, textile bleaches and dyestuffs, as well as various high temperature equipment applications.

Scaling

The safe scaling temperature for continuous service is 1600°F (871°C).

Corrosion Resistance

Carpenter Stainless Type 316/316L has been used in sulfite pulp mills to resist corrosion by sulfurous acid compounds. Due to its superior corrosion resistance, its use has been extended to handling many of the chemicals used by chemical process industries.

The alloy is more resistant to pitting than conventional 18-8 alloys.

For optimum corrosion resistance, surfaces must be free of scale, lubricants, foreign particles, and coatings applied for drawing and heading. After fabrication of parts, cleaning and/or passivation should be considered.

Important Note: The following 4-level rating scale is intended for comparative purposes only. Corrosion testing is recommended; factors which affect corrosion resistance include temperature, concentration, pH, impurities, aeration, velocity, crevices, deposits, metallurgical condition, stress, surface finish and dissimilar metal contact.

Nitric Acid	Good	Sulfuric Acid	Moderate
Phosphoric Acid	Moderate	Acetic Acid	Good

Carpenter Stainless Type 316/316L

Sodium Hydroxide	Moderate	Salt Spray (NaCl)	Good
Sea Water	Moderate	Sour Oil/Gas	Moderate
Humidity	Excellent		

Properties

Physical Properties

Specific Gravity	7.95
Density	7944 kg/m ³
Mean Specific Heat (0 to 100°C)	0.5021 kJ/kg/K
Mean CTE (0 to 649°C)	18.5 x 10 ⁻⁶ cm/cm/°C
Electrical Resistivity (23°C)	739.6 micro-ohm-mm

Heat Treatment

Annealing

Heat to 1850/2050°F (1010/1121°C) and water quench. Brinell hardness approximately 150.

Hardening

Cannot be hardened by heat treatment. Hardens only by cold working.

Workability

Forging

Carpenter Stainless Type 316/316L can be readily forged, upset and hot headed.

To forge, heat uniformly to 2100/2300°F (1149/1260°C). Do not forge below 1700°F (927°C). Forgings can be air cooled.

Best corrosion resistance is obtained if the forgings are given a final anneal.

Cold Working

Carpenter Stainless Type 316/316L can be deep drawn, stamped, headed and upset without difficulty. Since this alloy work hardens, severe cold forming operations should be followed by an anneal.

Machinability

Carpenter Stainless Type 316/316L machines with chip characteristics that are tough and stringy. The use of chip curlers and breakers is advised. Since the austenitic stainless steels work harden rapidly, heavy positive feeds should be considered.

Following are typical feeds and speeds for Carpenter Stainless Type 316/316L.

Carpenter Stainless Type 316/316L

Typical Machining Speeds and Feeds—Carpenter Stainless Type 316/316L

The speeds and feeds in the following charts are conservative recommendations for initial setup. Higher speeds and feeds may be attainable depending on machining environment.

Turning—Single-Point and Box Tools

Depth of Cut (inches)	Micro-Melt® Powder HS Tools			Carbide Tools (Inserts)			
	Tool Material	Speed (fpm)	Feed (ipr)	Tool Material	Speed (fpm)		Feed (ipr)
					Uncoated	Coated	
.150	M48,T15	102	.015	C2	350	450	.015
.025	M48,T15	120	.007	C3	400	525	.007

Turning—Cut-Off and Form Tools

Tool Material		Speed (fpm)	Feed (ipr)						
Micro-Melt® Powder HS	Carbide Tools		Cut-Off Tool Width (inches)				Form Tool Width (inches)		
			1/16	1/8	1/4	1/2	1	1½	2
M48,T15	C2	90	.001	.0015	.002	.0015	.001	.001	.001
		330	.004	.0055	.007	.005	.004	.0035	.0035

Rough Reaming

Micro-Melt® Powder HS		Carbide Tools		Feed (ipr) Reamer Diameter (inches)					
Tool Material	Speed (fpm)	Tool Material	Speed (fpm)	1/8	1/4	1/2	1	1½	2
M48,T15	84	C2	90	.003	.005	.008	.012	.015	.018

Drilling

Tool Material	Speed (ipm)	Tools							
		Feed (inches per revolution) Nominal Hole Diameter (inches)							
		1/16	1/8	1/4	1/2	3/4	1	1½	2
M42	50-60	.001	.002	.004	.007	.010	.012	.015	.018
C2-Uncoated	110	--	.002	.004	.006	.0085	.0096	.0113	.0113
C2-Coated	140	.0005	.002	.004	.006	.0085	.0096	.0113	.0113

Die Threading

FPM for High Speed Tools				
Tool Material	7 or less, tpi	8 to 15, tpi	16 to 24, tpi	25 and up, tpi
M7, M10	8-15	10-20	15-25	25-30

Milling, End—Peripheral

Depth of Cut (inches)	Micro-Melt® Powder HS Tools						Carbide Tools					
	Tool Material	Speed (fpm)	Feed (ipt) Cutter Diameter (inches)				Tool Material	Speed (fpm)	Feed (ipt) Cutter Diameter (inches)			
			1/4	1/2	3/4	1-2			1/4	1/2	3/4	1-2
.050	M48, T15	90	.001	.002	.003	.004	C2	270	.001	.002	.003	.005

Tapping

High Speed Tools	
Tool Material	Speed (fpm)
M7, M10	12-25

Broaching

High Speed Tools		
Tool Material	Speed (fpm)	Chip Load (ipt)
M48, T15	18	.0040

Additional Machinability Notes

When using carbide tools, surface speed feet/minute (SFPM) can be increased between 2 and 3 times over the high-speed suggestions. Feeds can be increased between 50 and 100%.

8.2 Annex B: Datasheet WC powder

Höganäs

CERTIFICAT D'ANALYSE

Page:
1(1)

Nom article
4590
Code article
101222

Numéro lot
2017724
Date édition
2015-04-15
No cde
0010264144
Livraison
1688580
Expédition
3261406

Client
SIRRIS
Celestijnenlaan 300C
B-3001 HEVERLEE

62271

Quantité
20 Kg
Votre référence
265188

	Résultat test	Spécification		ISSUE 1
		Compt	MIN	
CHEMICAL PROPERTIES				
Carbon	4.0 %		3.5	4.2 %
Tungsten is BALANCE				
Iron	0.1 %			0.5 %
Others (Total)	0.1 %			0.2 %
SIEVE ANALYSIS				
+212 Microns	0 %			0 %
+180 Microns	0.0 %			0.5 %
+150 Microns	0.5 %			5.0 %
+90 Microns	58.5 %			
+53 Microns	40.5 %			
-53 Microns	0.5 %			5.0 %

Validé par



Carl Mary
Quality Control Manager

09:06:06

2015-04-15

BE1

COAMMS480AH-A4

Höganäs Belgium S.A.
Ruelle Gros Pierre 10
B-7800 ATH

Téléphone 32 68 268989
Fax 32 68 285775

BANK: Nordea Bank AB, Frankfurt Branch
SWIFT/BIC: NDEADEF3
IBAN (EUR): DE39 5143 0300 8602 6600 01
IBAN (USD): DE12 5143 0300 8602 6600 02
IBAN (GBP): DE82 5143 0300 8602 6600 03

RPM Tournai
BE 0422.056.601

8.3 Annex C

Extract from “Höganäs: Designing for abrasive environments – Ni SF alloy mixes with tungsten carbides”.

Dissolution of carbides

Tungsten carbides can dissolve in the liquid nickel-based matrix. This is another factor that influences the final coating properties. The larger the degree of dissolution, the lower the abrasive wear resistance and impact wear of the final coating.

Low heat input and fast solidification rate suppress the dissolution of the tungsten carbide particles. As illustrated in figure 3, a) and c), lower heat input from laser cladding results in lower dissolution of carbides. Chemical composition of the matrix, the microstructure and the amount, size and shape of the carbide particles can also affect the dissolution. For example macrocrystalline carbides are thermally more stable than other types of carbides, illustrated in figure 3, a) and b).

The selection of correct process parameters is fundamental in affecting coating properties. In order to achieve sound clads with limited dissolution and good distribution of the tungsten carbides, the process parameters must be optimised for each mix.

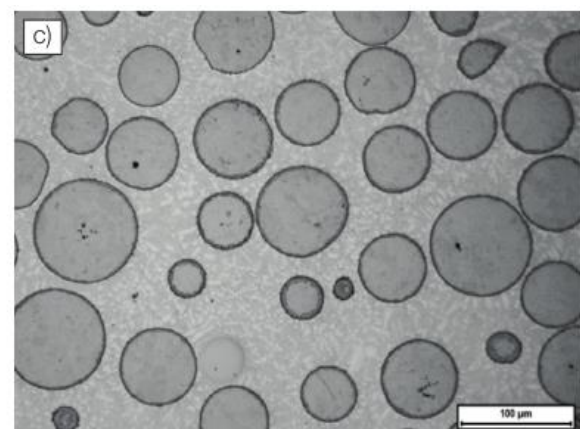
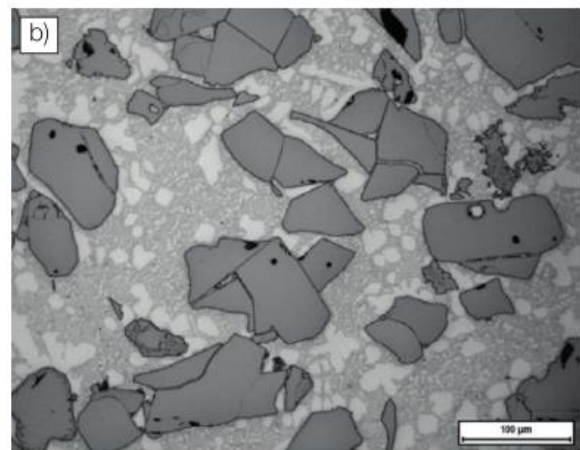
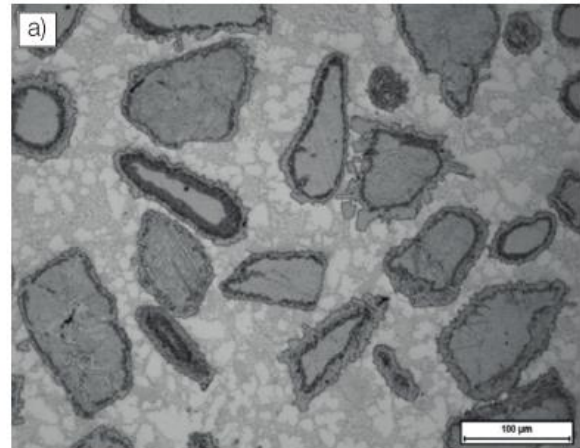


Figure 3. The micrographs show the microstructure of clads based on 1559-40 with 50wt%

a) 4570, PTA welded

b) 4580 PTA welded

c) 4590, laser cladded.

The samples were oxide polished.

